Highly Efficient Diode-Pumped Lasers based on In-Band Pumping of Nd:YVO_4 crystal

by

Tanant Waritanant

A thesis submitted to the Faculty of Graduate Studies of The University of Manitoba

In partial fulfilment of the requirements of the degree of

DOCTOR OF PHILOSOPHY

Department of Electrical and Computer Engineering

University of Manitoba

Winnipeg

Abstract

Among the neodymium-doped laser gain media, the crystal of yttrium orthovanadate ($Nd:YVO_4$) has been studied as an alternative to Nd:YAG for medium range power applications due to its several advantages in crystal properties such as very high emission cross-section and inherent birefringence. At very high output power, however, the $Nd:YVO_4$ laser crystal is still limited by the inferior thermal properties which lead to a stronger thermal gradient. This affects laser operation in various ways and ultimately results in unstable cavity (optical resonator). $Nd:YVO_4$ has regained a lot of attention recently due to the possibility to absorb pump at longer wavelengths thus reducing the thermal load. This was only recently allowed by the fact that the laser diode technology has developed more efficient sources at other wavelengths that are ideal for diode-pumped solid-state lasers.

This thesis presents a study and quantification of thermal lensing effects of $Nd:YVO_4$ laser under 914 nm pumping in order to develop wavelength tunable $Nd:YVO_4$ laser based on the ${}^4F_{3/2} \rightarrow {}^4F_{11/2}$ transitions with high efficiency and output power. To achieve higher efficiency and allow for higher power scaling, the reduction in thermal lensing due to the lower quantum defect (defined as the difference between the pump photon energy and laser photon energy) is the main driving mechanism. The thermal lensing effects were found to be lowered by a factor of two under the new pumping wavelength at 914 nm which is attractive for power scaling purposes and particularly attractive for laser gain media with inferior thermal properties.

Once thermal effects have been quantified, discrete wavelength tuning of $Nd:YVO_4$ laser between adjacent competing emission lines with birefringent plates as intracavity selectors was demonstrated with the highest slope and optical-to-optical efficiencies.

Due to the increasing interest in dual-wavelength operation for the use as an optical source for terahertz (THz) radiation via difference frequency generation, this thesis also gave a demonstration of two selectable pairs of power-ratio-tunable dual-wavelength operation with multiple intracavity birefringent plates along with explanation of gain balancing. The results obtained by this method provided the best output power in dual-wavelength operation for the wavelength pairs of interest, on-demand switching, tunable power-ratio, and robustness of the setup compared to other static methods of gain balancing.

The latter half of the thesis was concentrated on developing highly efficient picosecond pulsed operation (mode-locked, ML) of Nd:YVO_4 laser based on the low quantum defect pumping which also elevates the theoretical limit of the efficiency of laser systems. The experimental results obtained in this section show the highest to date slope efficiency that has been obtained with any neodymium-doped laser gain media.

The combined knowledge from discrete tuning section and mode locking section paved the way for the discretely tunable multi-wavelength mode-locked Nd:YVO_4 laser which we have demonstrated for the first time.

Finally, this thesis ends with preliminary test on other possible neodymium-doped laser gain media that can benefit the most from the technique of in-band pumping and can be used to develop medium range output power from Nd-doped gain medium with sub-picosecond pulse generation capability.

Acknowledgment

First, I would like to thank my grandfather for his lessons on integrity and the meaning of hard work and my grandmothers for their unrelenting encouragement. It is also my greatest pride and pleasure to give my deepest gratitude to my mom and dad for their kind and enduring teaching, their understanding, and their unconditional love. I certainly believe that none of this would have been possible without them.

I would like to give my greatest thank-you to my advisor, Prof. Arkady Major, whose office door was always open whenever I had any question about my research or writing. I would also like to express my gratitude to my committee members, Prof. Peter Zetner and Prof. Puyan Mojabi, for their helpful discussions, thought-provoking questions, and advices on the whole project and the formation of this thesis.

Other sincere thanks go to Prof. Waleed S. Mohammed whose encouragement had provoked my inspiration during my undergraduate study and Prof. Te-Yuan Chung for his technical trainings and his countless examples of logical thinking.

A big thank you to my good friend Reza Akbari for his very helpful discussions and sense of humor and Sujith Manjooran and his family for their hospitality. I really enjoyed my time spent on working with all my colleagues in Prof. Major's biomedical photonics group.

I would also like to thank the University of Manitoba for awarding me the graduate fellowship, the international graduate student scholarship, and the financial support for attending academic conferences.

Finally, I would like to thank the country of Thailand for being such a lovely home and Canada for its warmth even in the middle of the coldest winter.

Contents

List of Figures

List of Tables

List of symbols and abbreviations

Symbols (in order of appearance)

h	Planck constant
v	Frequency
c	The speed of light
η_h	Fractional thermal load
λ	Wavelength
T	Temperature
Q	Thermal load
K_c	Thermal conductivity
r	Radius
n	Refractive index
D_{th}	Dioptric power
f_{th}	Focal length of the thermal lens
P_{abs}	Absorbed pump power
w_p	Pump radius
α_T	Thermal expansion coefficient
$C_{r,\theta}$	Elasto-optical coefficient
I	Light intensity
σ_{abs}	Absorption cross-section
N	Dopants concentration
U	Electric field
k	Wavenumber
Z_R	Rayleigh range
M^2	Beam quality parameter (M-squared)
r_p	Normalized pump intensity distribution
s	Normalized cavity mode intensity distribution
η_m	Mode-matching quality
η_s	Slope efficiency

$\eta_{o\text{-}o}$	Optical-to-optical efficiency
α_{abs}	Absorption coefficient
M_{th}	Thermal lens sensitivity factor
P_{th}	Threshold power
L_{λ}	Round trip intracavity loss at wavelength λ
T_{OC}	Transmission of the output coupler
l	Length of the crystal
η_{λ}	Quantum defect efficiency (Stoke's factor)
σ	Emission cross-section
τ	Upper state lifetime
L_{in}	Round trip intracavity loss without BRF filter
L_{BRF}	Loss introduced by the BRF.
E_p	Pulse energy
$E_{sat,SESAM}$	Saturation energy of the SESAM
$E_{sat,Laser}$	Saturation energy of the gain medium
$F_{sat,L}$	Fluence at the gain medium
$\Delta\delta$	Phase retardation
L	Cavity length
ω_m	Modulation frequency
Λ	Period of the Bragg reflector
ΔR	Modulation depth

Abbreviations

AR	Anti-reflection
BRF	Birefringent filter
CARS	Coherent anti-Stokes Raman scattering
CW	Continuous wave
CW-ML	Continuous wave mode locking
DFG	Difference frequency generation
DM	Dichroic mirror
DPSS	Diode-pumped solid-state laser

FEA	Finite element analysis
FWHM	Full width at half maximum
HR	High-reflectivity
ML	Mode locking
NIR	Near infrared
OC	Output coupler
QD	Quantum defect
QS	Q-switching
QS-ML	Q-switched mode locking
RF	Radio frequency
SESAM	Semiconductor saturable absorber mirror

Chapter 1

Introduction

Lasers, which originally came from the acronym for Light Amplification by Stimulated Emission of Radiation, are optical devices which make use of the process called stimulated emission to generated near-monochromatic and highly coherent light (light waves that have a fixed phase relationship in space and time). Lasers can be divided into different categories based on the type of laser gain medium (the material which has the suitable energy level for the stimulated emission to occur) used in the system, such as solid-state, gas, liquid, and semiconductor lasers.

Among different types of lasers, solid-state lasers have major advantages over other means of efficient generation of coherent radiation. For example, when compared to laser diodes (semiconductor lasers), solid-state lasers are able to provide much better beam quality (an example of beam quality factor is given in section 2.4.1) of the output at the same power level. The comparison between solid-state and gas lasers can also be made which favors solid-state laser due to higher wall-plug efficiency. Regarding the applications, efficient solid-state lasers both in continuous wave and pulsed regimes are desirable for micro-machining, material processing, laser deposition, biomedical imaging, biomedical research, and microsurgery.

Historically, solid-state laser was the first demonstrated in the form of a ruby laser. However, it was not until 1964 when the very first diode-pumped solid-state laser (DPSS) was demonstrated by R.J. Keyes and T.M. Quist [1]. The main reason behind the use of a laser diode to pump a solid-state laser is due to the narrow band output spectrum of the laser diode when compared to other radiation sources such as flash lamps. This narrow band output of the laser diode, when designed to fall into the high absorption band of the solid state-laser gain medium, could greatly enhance the power efficiency of the solid-state laser systems.

Within the past few decades, because of its several advantages in diode-pumped laser systems such as very high emission and absorption cross-sections, the crystals of neodymium yttrium orthovanadate ($Nd:YVO_4$) have become more widely used in many compact laser devices with low to mid-range output power up to tens of Watts or Class 4 according to the International Electrotechnical Commission (IEC) classification. For consistency, this thesis considers the output power below 100 mW as low power level, 100 mW to 50 W as medium power level, and above 50 W as high power level.

This thesis proposed to study Nd-doped laser crystals as an efficient source of picosecond (10^{-12} s) pulses with medium output power level. This chapter discussed the background information of the different aspects of a mode-locked diode-pumped Nd:YVO_4 laser.

1.1 Picosecond ultrafast lasers

Picosecond lasers refer to lasers which can generate trains of short optical pulses with duration of 1 to tens of picoseconds (hence the 'ultrafast' terminology) which are the limits set by their gain bandwidth [2]. The benefits of having lasers with short optical pulses are because they can provide extremely high peak power compared to continuous wave lasers. This means that this type of laser can provide a large amount of photons in a very short period of time which is required to observe some of the non-linear optical processes.

Although femtosecond (10^{-15} s) lasers such as Ti:sapphire lasers can provide much shorter pulses and higher peak power which are even more suitable for applications which heavily rely on non-linear phenomena such as multi-photon absorption, they are much less economical, power inefficient (due to their intrinsic loss through large quantum defect), and unnecessary for some applications in which pulse energy and average power are more important, e.g. micromachining and microsurgery.

As an example of biomedical applications of picosecond lasers, two-photon bio-imaging has been demonstrated with picosecond lasers with pulse duration of 5 ps and only 1.1 kW of peak power level [3]. Another important biomedical use for picosecond lasers is for coherent anti-Stokes Raman scattering (CARS) microscopy which prefers picosecond to femtosecond lasers in the near infrared (NIR) range due to their much smaller bandwidth (i.e. higher spectral resolution) while still providing high peak power levels [4-6]. Intraocular microsurgery was demonstrated in [7] using picosecond Nd:YAG laser. Osteotomy using a picosecond Nd:YVO_4 laser was also tested [8]. Recently, an efficient tissue and bone non-thermal ablation was tested with frequency doubled picosecond Nd:YVO_4 laser [9].

There are different types of laser sources which can generate picosecond pulses such as fiber lasers, solid-state lasers, and semiconductor lasers, each with their own advantages and disadvantages. Among them, the most common sources are the mode-locked solid-state lasers which have an advantage of providing higher pulse energy, high peak power, excellent pulse quality, and near diffraction limited beam quality which are all important for the resolution of the scanning systems.

1.2 Motivation and objectives

From the uses of picosecond lasers in the applications mentioned above and the attractiveness of the low cost, high quality output, and high wall-plug efficiency of the solid-state laser systems, this research aims to develop an efficient picosecond laser that meets the requirements for biomedical imaging, notably, picosecond pulse duration of approximately <20 ps and medium average output power (>1 W) with Nd:YVO_4 laser laser crystal. Further power scaling options for applications that demand higher average power are also mentioned in the conclusion of the chapter 2.

Our approach to solve this task is as follows. First, to study the thermal effect of the new in-band pumping scheme (pumping directly to the upper energy level of the laser transition) at 914 nm instead of the classical 808 nm pump wavelength in Nd:YVO_4 laser crystal which would allow the system to operate under higher pump power with lower effect on the laser system stability. Secondly, to use this pumping technique to explore the high efficiency in pulsed (mode-locked) regime. Thirdly, to develop a method for wavelength tunability under continuous wave and mode-locked regimes. Finally, to investigate the possibility of using other laser crystals with similar thermal properties but larger gain bandwidth such as Nd:$ScYSiO_5$ (SYSO) and Nd:$CaYAlO_4$ (Nd:CYA) under 914 nm pumping. The rest of this chapter will provide some background information and basic properties of the Nd-doped laser crystal chosen for this research, Nd:YVO_4.

1.3 Nd:vanadate (Nd:YVO_4) laser crystal

Solid-state laser gain media are comprised of crystal host materials and rare earth metal dopants. Dopants replace other ions of relatively the same size in the host material and roughly determine the absorption and emission wavelengths of the laser. The crystallographic structure of the host material holds these dopants in place and affects the energy level arrangements of the dopant ions. In Nd-doped gain media, these dopants are neodymium ions (Nd^{3+}). The following table provides relevant properties of the three most common Nd-doped laser crystals.

Table 1-1. Laser crystal properties compared with 1% doping concentration [2,10,11]

Crystal	$Nd:YVO_4$	Nd:YAG	Nd:YLF
Laser wavelength (nm)	1064	1064	1047 (π), 1053 (σ)
Stimulated emission cross-section (10^{-19} cm^2)	**25 (π)**, 7 (σ)	2.8	1.8 (π), 1.2 (σ)
Fluorescence lifetime (μs)	90	230	485
Emission linewidth (nm)	0.96	0.51	1.47
Thermal conductivity ($Wm^{-1}K^{-1}$)	**5**	14	6.3
Thermo-optical coefficient (dn/dT) (10^{-6} K^{-1})	**15.5 (σ)** **8.41 (π)**	7.3	-4.3 (π), -2.0 (σ)

In Nd-doped yttrium orthovanadate ($Nd:YVO_4$) crystal, Nd^{3+} ions replace Y^{3+} ions in the host crystal. The host material is tetragonal with lattice parameters a, b = 7.12 Å, and c = 6.29 Å. Crystals with tetragonal structure are naturally uniaxial birefringent, meaning that the a- and b-axes are equivalent, and differ from the c-direction. $Nd:YVO_4$ crystal can be oriented along the a- or c- axis. In most cases, the $Nd:YVO_4$ crystal is oriented along the a-axis with surface coatings done on both front and back surface due to the higher pump absorption for light polarization with the electric field vector directed along the c-axis. Fig. 1-1 illustrates crystallographic axes and dimensions of one of the $Nd:YVO_4$ crystal used in the experiments.

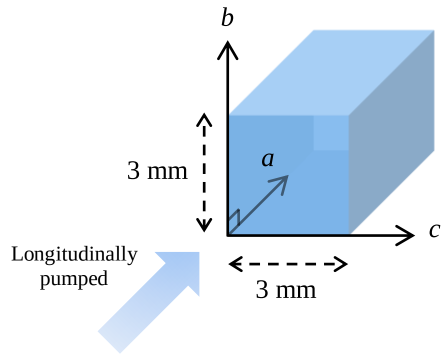

Fig. 1-1 Crystallographic axes of 12-mm-long Nd:YVO_4 crystal used in the experiment.

Nd:YVO_4 laser is a 4-level laser system in which laser operation involves 4 energy levels and has been extensively studied as an alternative to Nd:YAG for medium range power applications due to several advantages such as its very high emission cross section, broader absorption profile, and birefringence [2,12]. The absorption spectrum of the Nd:YVO_4 crystal is shown in Fig. 1-2 [13]. The π- and σ-polarizations in the figure are used in uniaxial crystals to denote the polarizations parallel and perpendicular to the optical axis of the crystal (c-axis), respectively. The emission spectrum of the Nd:YVO_4 crystal is shown in Fig. 1-3 [14].

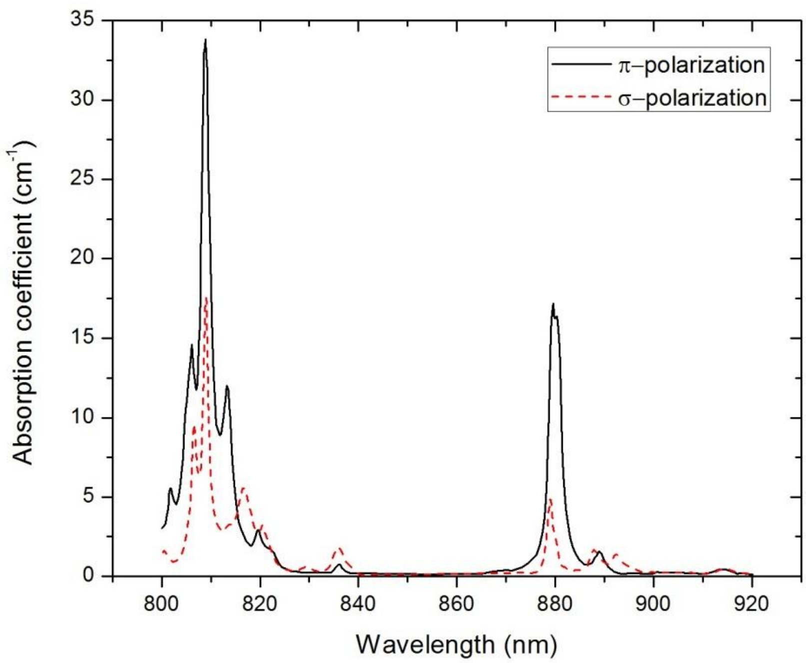

Fig. 1-2 Absorption spectrum of Nd:YVO_4 [13].

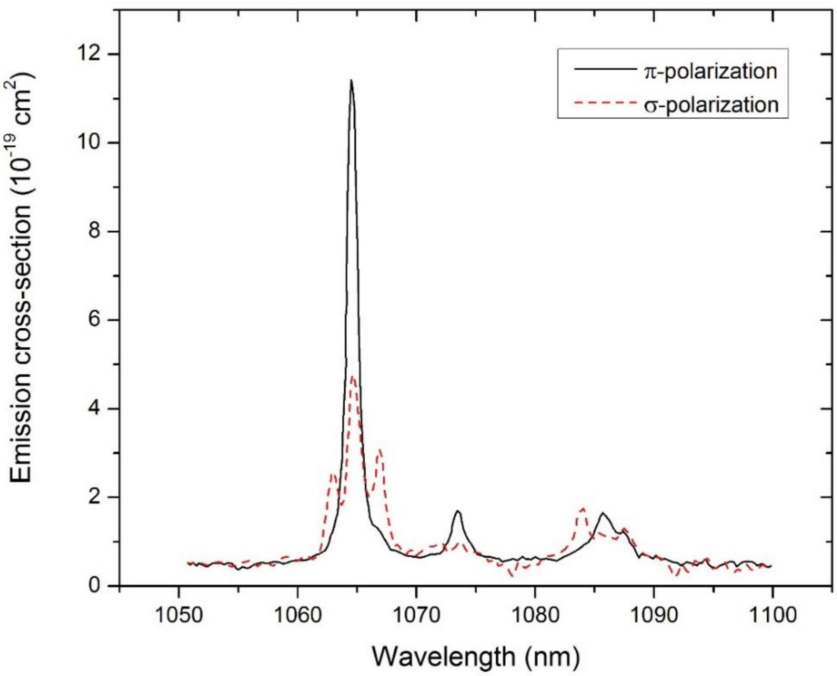

Fig. 1-3 Emission spectrum of $Nd:YVO_4$.

Stimulated emission cross-section of light polarization with the electric field vector parallel to the c-axis (π-polarization) of the $Nd:YVO_4$ crystal is 3-4 times higher than that parallel to the a-axis (σ-polarization) resulting in polarized laser emission parallel to the c-axis due to much higher gain.

However, at high output power, performance of the $Nd:YVO_4$ laser crystals is limited by their thermal properties which lead to a strong thermal gradient [5,10-14]. The induced thermal gradient degrades the optical properties of the gain medium, the stability of the laser cavity, the output beam quality, and the optical efficiency. Ultimately, a large thermal gradient could results in failure of the material. To overcome this limitation, recent studies have focused on diode pumping of $Nd:YVO_4$ crystals at other absorption lines with longer wavelengths. The longer pump wavelengths result in the reduction of quantum defect (*QD*) defined in equation (1-1) as

$$QD = h\nu_{pump} - h\nu_{laser} , \tag{1-1}$$

where h is the Planck's constant and ν is the frequency of the electromagnetic wave.

Multiple pump wavelengths such as 880 nm, 888 nm and 914 nm to produce 1064 nm laser output [15-20] have been proposed and studied. The energy level of Nd:YVO_4 showing corresponding optical transitions are shown in Fig. 1-4.

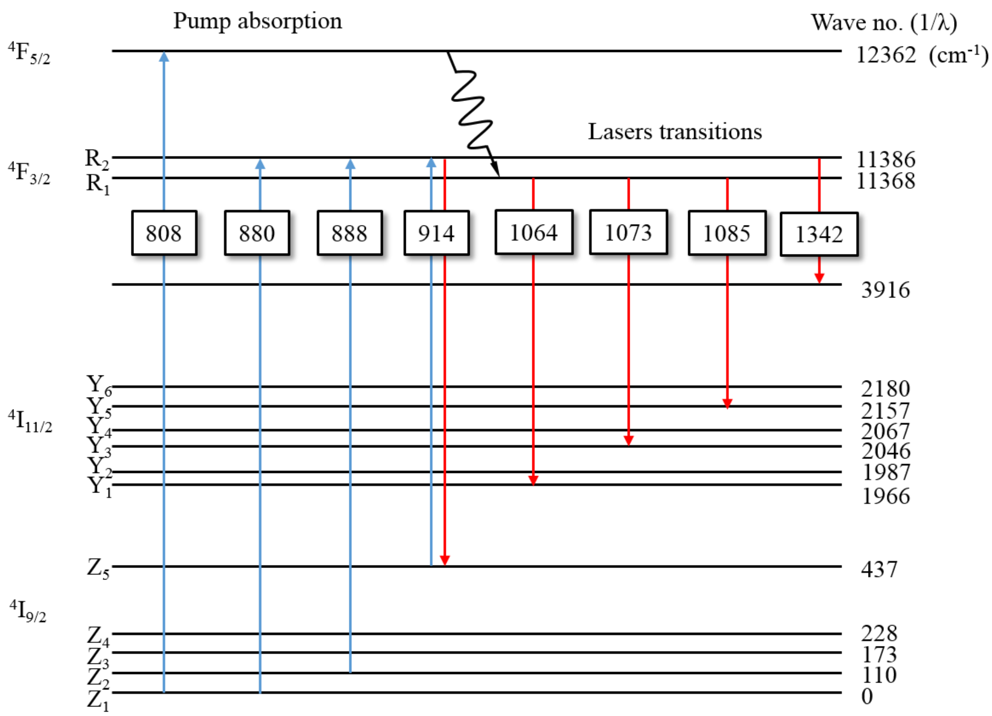

Fig. 1-4 Energy level diagram of Nd:YVO_4 absorption and laser transitions.

The smaller quantum defect from the longer pump wavelengths translates directly to a smaller amount of heat generated within the crystal due to the relaxation process with minimal effect from energy transfer upconversion (ETU) and quenching in continuous wave regime [21]. In this work, 914 nm was used as the pump wavelength instead of the conventional 808 nm, which reduced the quantum defect by ~40%. There was, however, no report focusing on thermal lensing effect in such cases.

1.4 Laser diodes at 914 nm

Laser diodes are generally used to pump solid-state lasers. However, there are some exceptions like Ti:sapphire crystal which has the peak absorption around 480 nm at which it has limited pumping options and therefore is generally pumped by another frequency-doubled solid-state laser such as Nd:YVO_4. This results in an extremely low wall-plug efficiency since the system involves two solid-state lasers instead of one as well as one frequency conversion process.

Among the wavelengths that are absorbed by the Nd:YVO_4 as mentioned in the last section, 914 nm is the longest wavelength. Conveniently, the high-power fiber-coupled InGaAs laser diodes around 914 nm are widely used for pumping of the Yb-doped fiber lasers and are readily available for power scaling experiments. Moreover, they provide better lifetime, efficiency, and higher power than their AlGaAs counterparts that generate 808, 880, and 888 nm output [18]. The beam quality of the output at 914 nm is also usually more than 4 times better than AlGaAs laser diodes and therefore allows for efficient mode-matching (i.e. overlapping of the pump and laser mode volumes) in longer laser crystals which will be discussed in more detail in the next chapter.

1.5 Previous results with 914 nm pumping

First direct in-band diode-pumping of Nd:YVO_4 at 914 nm was demonstrated by D. Sangla et al. in 2009 with a 1.5 at. %-doped 10 mm long a-cut Nd:YVO_4 crystal [18]. The absorption band at 914 nm was measured to be approximately 4 nm which is larger than the available laser diode bandwidth of 2.5 nm. The absorption coefficient was also measured to be 0.65 cm^{-1} for polarization along the c-axis and 0.46 cm^{-1} along the a-axis which is much lower than the strong difference at classical 808 nm pump wavelength (~2 times). Therefore, it was confirmed that this absorption band is suitable for diode pumping which usually utilized unpolarized light. At the highest pump power of 35 W limited by the laser diode, 14.6 W was absorbed and maximum laser output power was 11.5 W. The slope efficiency was found to be 80.7% which is very close to the theoretical limitation of quantum defect efficiency at 86%. The optical efficiency was 78.7% which is the highest ever reported for a diode-pumped Nd:YVO_4 laser at this power level. The definition of the slope efficiency and the optical efficiency will be given in section 2.4.4 in chapter 2.

Performance difference of Nd:YVO_4 laser at 1064 nm under 808 nm and 914 nm pumping were investigated by X. Delen et al. [21]. In order to control the geometry of the pumping, the two fiber-coupled laser diodes operating at 808 and 914 nm were chosen to have the same output characteristics. The laser crystals, however, were chosen with different doping concentrations, 0.1 at. % for 808 nm pumping and 1.5 at. % doping for 914 nm pumping, due to the large difference in their absorption coefficients. Even with the lower doping concentration in case of the 808 nm pumping, the absorbed pump power was still higher than that of the 914 nm pumping case. The authors then chose to compare the results of both pumping schemes under the same absorbed pump power. In continuous wave (CW) regime, slope efficiency of 81% and 58% were obtained for 914 nm pumping and 808 nm pumping, respectively. The difference in slope efficiency was due to the larger quantum defect in 808 nm pumping scheme proving one of the advantages of pumping at 914 nm. The fractional thermal loading was investigated in CW regime and found to be close to quantum defect value while fractional thermal loading in 914 pumping case was found to be higher than that of the 808 nm case in q-switching regime. Upconversion processes and nonradiative decays were identified as the factors responsible for such cases.

The first 1342 nm $Nd:YVO_4$ laser with 914 nm in-band pumping was demonstrated by X. Ding et al. [20] in 2011. In the experiment, another $Nd:YVO_4$ laser operating at 914 nm was used instead of a laser diode to pump the 1342 nm laser to ensure good overlapping of the pump beam and the oscillating laser mode. A 1.0 at. % doped and a 3.0 at. % doped *a*-cut $Nd:YVO_4$ crystals were used in the experiment to investigate the influence of doping concentration on laser performance. The highest output power of 0.86 W output was obtained under 1.82 W of absorbed pump power. The slope efficiency of 65.4% was reported which is the highest slope efficiency obtained in 1342 nm $Nd:YVO_4$ laser to date. The use of higher doping concentration was stated to have a negative impact on laser performance due to the lower stimulated emission cross section of the of $^4F_{3/2} \rightarrow {}^4I_{13/2}$ transition induced by heating. A longer $Nd:YVO_4$ crystal with lower doping was suggested instead of high concentration doping in order to maintain enough absorption and high efficiency in 914 nm in-band pumped $Nd:YVO_4$ laser.

So far, there has been no report on the performance of in-band pumped $Nd:YVO_4$ laser under mode locking regime. The only one result from hybrid material ($Nd:Gd_{0.6}Y_{0.4}VO_4$) demonstrated relatively low optical-to-optical efficiency of 27% and slope efficiency of only 44% which was caused by the non-optimal mode-matching condition for the TEM_{00} mode [22]. Moreover, to the best of my knowledge, although the gain from $Nd:YVO_4$ crystal supports laser oscillations at around 1073 and 1085 nm as seen in the emission spectrum Fig. 1-3, mode-locked operation at

1073 has never been reported before and only one report at 1085 nm line using Nd:$LuVO_4$ crystal was made [23]. The pulse duration of 144 ps was measured which is much longer than the minimum pulse duration allowed by the available gain bandwidth.

1.6 Contributions

The following contributions have been made in this study.

- Quantification of reduction in thermal lensing effect in Nd:YVO_4 under 914 nm and other pump wavelengths in comparison. The thermal lensing effect has been found to be 2.1 times weaker than with the traditional pump at 808 nm under the same condition. The results were published in [24].
- A successful demonstration of multi-wavelength Nd:YVO_4 laser selectable between 1064, 1073, 1085 nm with high efficiency. The results were published in [25].
- A new proposed combination of birefringent filters (with theoretical analysis) in order to manipulate gain-loss between different emission lines for dual-wavelength generation.
- A successful generation of dual-wavelength operation of Nd:YVO_4 at 1064 & 1073 nm and 1064 & 1085 nm with the highest efficiency demonstrated to date (submitted).
- A successful demonstration of the highest efficiency in picosecond pulse generation regime compared to all other Nd-doped gain media. The results were published in [26].
- First mode-locked operations at 1073 and 1085 nm lines from Nd:YVO_4 (submitted).
- First successful demonstrations of two disordered gain media (Nd:SYSO and Nd:CYA) under new in-band pump wavelength of 914 nm (to be submitted).

1.7 Overview of Thesis

This thesis investigates the potential for high efficiency diode-pumped continuous wave and mode-locked Nd:YVO_4 lasers operating at three different output wavelengths at 1064, 1073, and 1085 nm.

Chapter 2 presents the study of thermal lensing under 914 nm pumping in comparison with other pump wavelengths available for diode-pumped Nd:YVO_4 laser. The fundamentals of thermal lensing effect are reviewed in order to explain the sources of the resulting thermal lensing. Finite element analysis (FEA) simulations have been done under the same condition as the experiment to verify the accuracy of the experimentally measured value of thermal lens. Trade-off between multiple design parameters affecting thermal lens are discussed.

Chapter 3 investigates tunability between adjacent emission lines within the same terminal manifold in Nd:YVO_4 laser. The on-demand wavelength selectivity (which has not been demonstrated before) at the three wavelengths mentioned earlier was also demonstrated here due to the flexibility of the method used to introduce discrete tuning.

Chapter 4 presents the results for dual-wavelength operations using the modified tuning filter technique introduced in Chapter 3. A specific setup in order to achieve dual-wavelength operation with high efficiency was described.

Chapter 5 covers the fundamentals of passive mode locking with semiconductor saturable absorber mirror (SESAM) and reports the performance of an efficient, self-starting, diode-pumped passively mode-locked Nd:YVO_4 laser with in-band pumping with the highest slope efficiency to date. The significance of high slope efficiency was also discussed.

Chapter 6 reports on extending stable mode locking operation to 1073 nm and 1085 nm with wavelength selectivity with one experimental setup.

Chapter 7 details the future prospects for shorter pulse generation from other promising Nd:doped gain media under 914 nm pumping.

Chapter 8 presents the conclusion and discussion for the work given in this thesis.

References

[1] R. J. Keyes and T. M. Quist, "Injection Luminescent Pumping of CaF_2:U^{3+} with GaAs Diode Lasers," Appl. Phys. Lett. 4(3), 50 (1964).

[2] W. Koechner, *Solid-state Laser Engineering,* 6th ed. (Springer, 2006).

[3] H. Yokoyama, H. Guo, T. Yoda, K. Takashima, K. Sato, H. Taniguchi, H. Ito, "Two-photon bioimaging with picosecond optical pulses from a semiconductor laser," Opt. Express. 14(8), 3467-3471 (2006).

[4] C. Evans and X. Xie, "Coherent anti-Stokes Raman scattering microscopy: chemical imaging for biology and medicine," Annu. Rev. Anal. Chem. 1, 883 -909 (2008).

[5] C. Chung, Y. Lin, K. Wu, W. Tai, S. Chu, Y. Lee, Y. Hwu, Y. Lee, "Coherent anti-Stokes Raman scattering microscopy using a single-pass picosecond supercontinuum-seeded optical parametric amplifier," Opt. Express. 18(6), 6116-22 (2010).

[6] C. W. Freudiger, W. Min, B. G. Saar, S. Lu, G. R. Holtom, C. He, J. C. Tsai, J. X. Kang, X. S. Xie, "Label-Free Biomedical Imaging with High Sensitivity by Stimulated Raman Scattering Microscopy," Science 322(5909), 1857-1861 (2008).

[7] C. P. Lin, Y. K. Weaver, R. Birngruber, J. G. Fujimoto, C. A. Puliafito, "Intraocular microsurgery with a picosecond Nd:YAG laser," Lasers Surg. Med. 15(1), 44-53 (1994).

[8] Y. M. Lee, R. Y. Tu, A. C. Chiang, Y. C. Huang, "Average-power mediated ultrafast laser osteotomy using a mode-locked Nd:YVO_4 laser oscillator," J. Biomed. Opt. 12(6), 060505 (2007).

[9] C. Tulea, J. Caron, H. Wahab, N. Gehlich, M. Hoefer, D. Esser, B. Jungbluth, A. Lenenbach, and R. Noll, "Highly efficient nonthermal ablation of bone under bulk water with a frequency-doubled Nd:YVO_4 picosecond laser," Proc. SPIE 8565, 85656E (2013).

[10] O. Svelto, *Principles of Lasers* (Kluwar Academic Publishers, 1998).

[11] Y. Sato and T. Taira, "Highly accurate interferometric evaluation of thermal expansion and dn/dT of optical materials," Opt. Mater. Express 4(5), 876-888 (2014).

[12] G. Turri, H. P. Jenssen, F. Cornacchia, M. Tonelli, and M. Bass, "Temperature-dependent stimulated emission cross section in Nd:YVO_4 crystals," J. Opt. Soc. Am. B 26, 2084 (2009).

[13] L. McDonagh, R. Wallenstein, R. Knappe, and A. Nebel, "High-efficiency 60 W TEM_{00} Nd:YVO_4 oscillator pumped at 888 nm," Opt. Lett. 31(22), 3297-3299 (2006).

[14] R. D. Peterson, H. P. Jenssen, and A. Cassanho, "Investigation of the spectroscopic properties of Nd:YVO_4," J. Opt. Soc. Am. 68, 294 (2002).

[15] L. McDonagh, R. Wallenstein, and A. Nebel, "111 W, 110 MHz repetition-rate, passively mode-locked TEM_{00} Nd:YVO_4 master oscillator power amplifier pumped at 888 nm," Opt. Lett. 32(10), 1259-1261 (2007).

[16] N. Pavel, C. Krankel, R. Peters, K. Petermann, and G. Huber, "In-band pumping of Nd-vanadate thin-disk lasers," Appl. Phys. B 91, 415 (2008).

[17] Y. J. Wang, W. H. Yang, H. J. Zhou, M. R. Huo, Y. H. Zheng, "Temperature dependence of the fractional thermal load of Nd:YVO_4 at 1064 nm lasing and its influence on laser performance," Opt. Express 21(15), 18068-78 (2013).

[18] D. Sangla, M. Castaing, F. Balembois, and P. Georges, "Highly efficient Nd:YVO_4 laser by direct in-band diode pumping at 914 nm," Opt. Lett. 34(14), 2159-2161 (2009).

[19] X. Yu, F. Chen, R. Yan, X. Li, J. Yu, and Z. Zhang, "High power diode-pumped 914-nm Nd:YVO_4 laser," Chin. Opt. Lett. 8(5), 499-501 (2010).

[20] X. Ding, S. J. Yin, C. P. Shi, X. Li, B. Li, Q. Sheng, X. Y. Yu, W. Q. Wen, and J. Q. Yao, "High efficiency 1342 nm Nd:YVO_4 laser in-band pumped at 914 nm," Opt. Express 19(15), 14315-14320 (2011).

[21] X. Delen, F. Balembois, O. Musset, and P. Georges, "Characteristics of laser operation at 1064 nm in Nd:YVO_4 under diode pumping at 808 and 914 nm," J. Opt. Soc. Am. B 28, 52 (2011)

[22] H. C. Liang, Y. J. Huang, P. Y. Chiang, and Y. F. Chen, "Highly efficient Nd:$Gd_{0.6}Y_{0.4}VO_4$ laser by direct in-band pumping at 914 nm and observation of self-mode-locked operation," Appl. Phys. B 103(3), 637–641 (2011).

[23] J. H. Lin, P. K. Yang, "Passive mode locking of c-cut Nd : $LuVO_4$ laser by the SESAM at 1086 nm" in IQEC and CLEO Pacific Rim, Sydney, NSW, 1885-1886 (2011).

[24] T. Waritanant and A. Major, "Thermal lensing in Nd:YVO_4 laser with in-band pumping at 914 nm," Appl. Phys. B 122, 135 (2016).

[25] T. Waritanant and A. Major, "Selectable Multi-Wavelength Operation of a Diode-Pumped Nd:YVO_4 Laser," Opt. Lett. 42(6), 1149-1152 (2017).

[26] T. Waritanant and A. Major, "High efficiency passively mode-locked Nd:YVO_4 laser with direct in-band pumping at 914 nm," Opt. Express 24(12), 12851-12855 (2016).

Chapter 2

Thermal lensing under 914 nm pumping

In order to achieve the goal of an efficient picosecond pulse generation with medium-range power output with Nd-doped laser material, the most efficient laser crystal for diode pumping, $Nd:YVO_4$, was chosen. This is due to the fact that $Nd:YVO_4$ crystals have much higher stimulated emission cross-section as can be seen from table 1-1. However, it is counterbalanced by the inferior thermal conductivity when compared to the other Nd-doped crystals such as Nd:YAG which limits laser operation within the medium power range [1-6].

The main limitation in output power of diode-pumped solid-state laser systems is due to the thermal lensing effect which decreases the stability of the laser system and laser beam quality. In some cases, mechanical failure of the material can also happen from high enough thermal stress.

This study would confirm the usefulness of in-band pumping at 914 nm and its role to reduce the thermal problems in the $Nd:YVO_4$ crystal. Furthermore, the measurement of thermal lensing reduction will prove very useful and ideal for gain media with severe thermal problems such as laser crystals with disordered structures which will be discussed in Chapter 7.

2.1 Thermal lensing theory

In a laser system, laser crystals or gain media are optically pumped with radiation with higher photon energy than that of the laser output photons. The pump energy is then absorbed thus putting electrons from the ground state into the upper energy level and, under lasing condition, they undergo one or more non-radiative transitions resulting in increased lattice vibration of the crystal or heat. The difference in energy between a laser photon and a pump photon is defined as quantum defect (QD) as seen in equation (1-1).

This difference in energy dictates the amount of residual heat produced inside the crystal by the absorbed pump power. The fractional thermal load (η_h) is defined as

$$\eta_h = 1 - h\nu_{laser} / h\nu_{pump}, \tag{2-1}$$

or in terms of the pump and laser wavelengths [7],

$$\eta_h = 1 - \frac{\lambda_{pump}}{\lambda_{laser}}. \tag{2-2}$$

This residual heat from non-radiative electronic transition affects the crystal optical and mechanical properties. For a running CW laser, the steady-state heat equation becomes,

$$\nabla^2 T(x,y,z) = \frac{-Q(x,y,z)}{K_c}, \tag{2-3}$$

where ∇^2 is the Laplacian operator, T is the temperature (K), Q is the thermal load per unit volume (W m^{-3}), and K_c is the thermal conductivity (W m^{-1} K^{-1}). This is under the assumption that thermal conductivity is constant and is not dependent on the temperature.

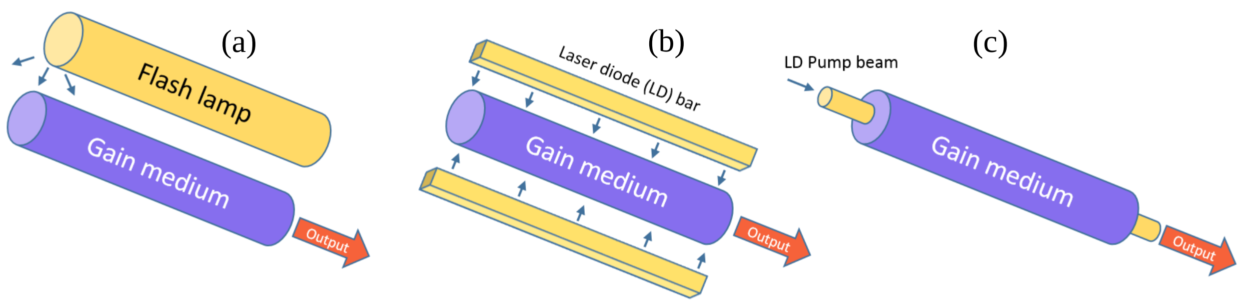

Fig. 2-1 Optical pumping geometries of solid-state lasers. (a) Flash lamp-pumped, (b) side-pumped, and (c) end-pumped.

In solid-state laser, there are multiple optical pumping geometries such as flash lamp pumping, which uses gas discharge lamp to pump the laser gain medium, side-pumping with laser diode, and end-pumping with laser diode with pump beam traveling along the same path as the laser output. The three pumping geometries are shown in Fig. 2-1.

Fig. 2-1(c) shows the basic configuration of an end-pumped solid-state laser where pump light is provided by a fiber-coupled laser diode module. The similarity of the geometry of the optical pump and the fundamental traverse mode of the laser cavity in the end-pumping scheme allows for a much more efficient laser system. Therefore in this thesis we focused on the end-pumping geometry since we are interested in medium to high power range laser with high efficiency.

Fig. 2-2. Provides a closer cross-sectional look at the end-pumping geometry starting from the fiber-coupled laser diode. The pump light is then focused into the optical resonator (laser cavity) with achromatic doublet through a dichroic mirror which acts as a total reflector at the laser wavelength.

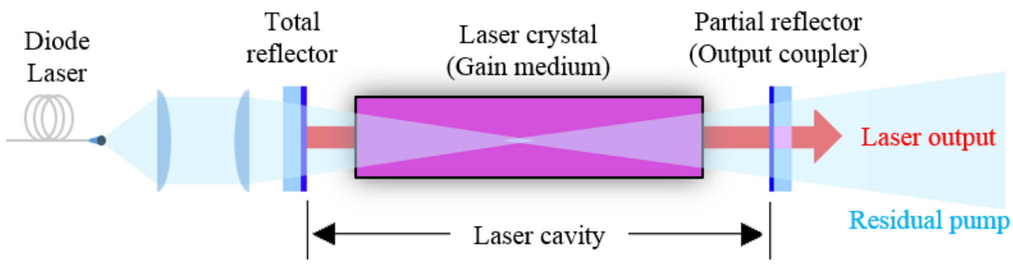

Fig. 2-2 Basic configuration of end-pumped solid-state laser.

With the end-pumping geometry in mind, equation (2-3) can be re-written with radial symmetry as

$$\frac{1}{r}\frac{\partial}{\partial r}\left(r\frac{\partial T}{\partial r}\right)+\frac{\partial^2 T}{\partial z^2}=\frac{-Q(r,z)}{K} \qquad (2\text{-}4)$$

where r is the radius from the optical axis of the crystal. The resulting change in temperature throughout the material of the gain media effects the crystal properties in multiple ways as shown in the diagram in Fig. 2-3.

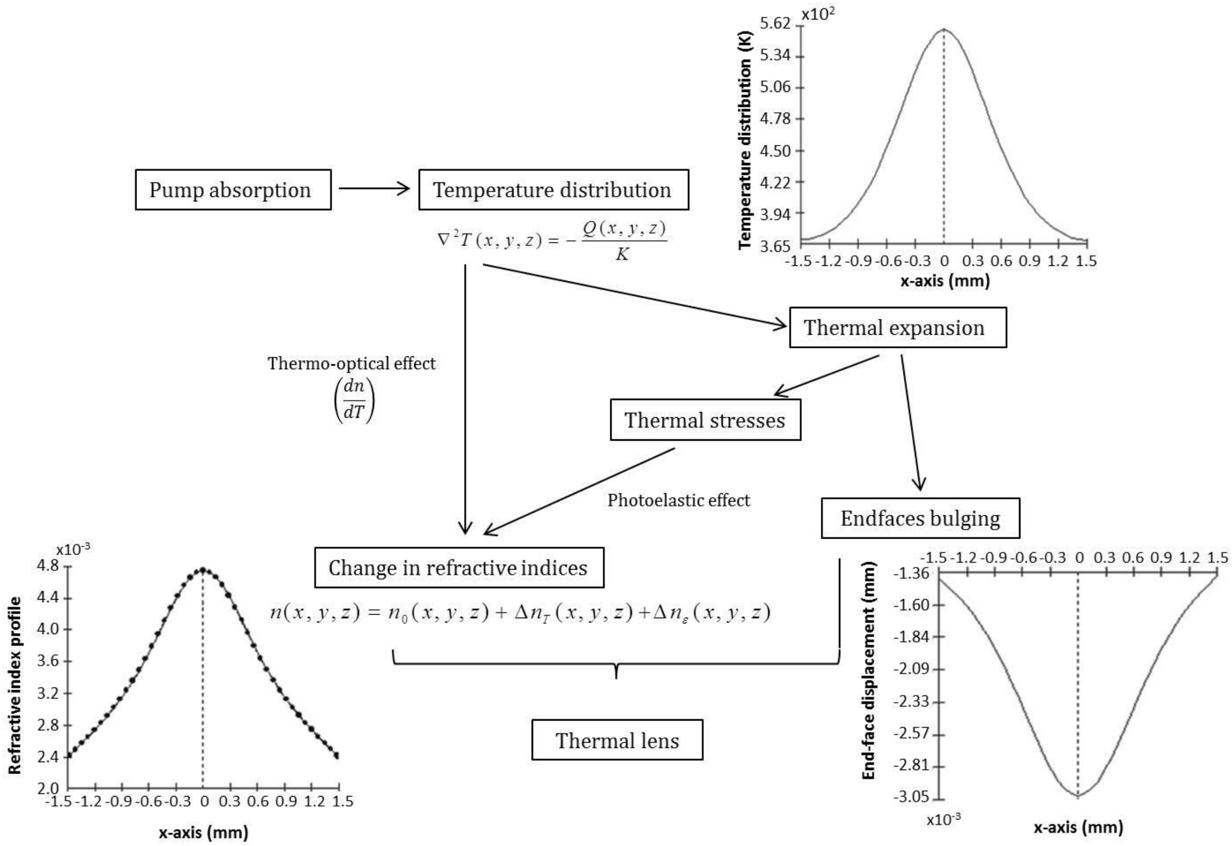

Fig. 2-3 Connection between multiple factors contributing to thermal lensing effect.

Optically, the heating of the crystal changes the material's refractive index (n) via thermo-optical effect creating a lens-like refractive index profile. Mechanically, the expansion throughout the crystal results in the change in the shape of crystal surfaces that is sometimes called thermally induced surface bulging. Moreover, it generates stress inside the crystal which is another source for the change in refractive index. Typically the largest contribution to thermal lensing in Nd:YVO_4 is the thermo-optical effect.

The analytical solution for the thermal lens has been described by Chenais et al. and Siegman's textbook [8,9] and can only be obtained under several strict assumptions including isotropic crystal. The solution is applicable only to the inside of the crystal pump volume, negligible pump divergence, and temperature, stress, strain, refractive index are considered integrated along the whole rod. The general form of thermal lens for the end-pumping geometry is then described as

$$D_{th} = \frac{1}{f_{th}} = \frac{\eta_h P_{abs}}{2\pi w_p^2 K_c}\left[\left(\frac{dn}{dT}\right)_{\varepsilon} + (n-1)(1+v)\alpha_T + 2n_0^3 \alpha_T C_{r,\theta}\right] \tag{2-5}$$

where D_{th} is the dioptric power of the thermal lens, f_{th} is the focal length of the thermal lens, n_h is the fractional thermal load, P_{abs} is the absorbed pump power, w_p is the pump radius (constant in this analysis), K_c is the thermal conductivity in $Wm^{-1}K^{-1}$, α_T is the thermal expansion coefficient in K^{-1}, n_0 is the refractive index at the center of the rod, and $C_{r,\theta}$ are the functions of the elasto-optical coefficients of the crystals.

One noteworthy observation here is that the thermal lens dioptric power (D_{th}) is inversely proportional to the area of the pump beam. This must be taken into account when comparing thermal lens data from various sources.

Analytical solution for conditions closer to the real world systems with all the thermal effects combined are more complicated and therefore, finite element analysis (FEA) is usually required in order to calculate the effective dioptric power of the thermal lens under thermodynamic equilibrium.

2.2 Thermal lensing measurement methods

Even when taken into account, the unwanted effects such as aberrations and induced birefringence often make an accurate simulation of thermal effects extremely complex. Therefore, realistic values of thermal lens are usually obtained experimentally. There are multiple techniques for measuring thermal lens effect which can be classified into two main groups, the geometrical methods and wavefront measurements.

The geometrical methods are the commonly used methods to measure thermal lens. They utilize the changes in beam size and divergence at various locations to determine changes made to the cavity from thermal effects.

The most straight forward way is to launch an external probe beam with comparable dimension as the laser beam through the laser gain medium in order to see the focusing or defocusing of the probe beam (Fig. 2-3(a)). If a much smaller probe beam is used, point-by-point deflection from different location of the gain material can be obtained. The thermal lens can also be measured by monitoring the changes in the laser output beam given that the conditions for stable laser operation remain constant.

Another way is to focus on the effect of the stability of the laser cavity itself by designing the cavity in such a way that the condition for stable standing wave resonator of the cavity depends heavily on the lens created inside the crystal as shown in Fig. 2-3(b). The introduction to cavity design parameters will be described more in section 2.3.1.

In wavefront measurements, one relies on the difference between phase shifts of the wave propagating along the optical axis and the wave propagating at the edge of the beam, which can be determined using interferometric techniques such as Michelson interferometer as shown in Fig. 2-3(c). Practically, the wavefront measurement methods are not suitable for end-pumping schematic due to the small dimension (100s μm) of thermal lens created in the gain medium which creates much smaller phase shift than 1 wavelength and therefore not enough phase shift to generate fringe pattern within the cross-sectional area of the beam [8]. The drawings for different methods of thermal lens measurements are shown in Fig. 2-3.

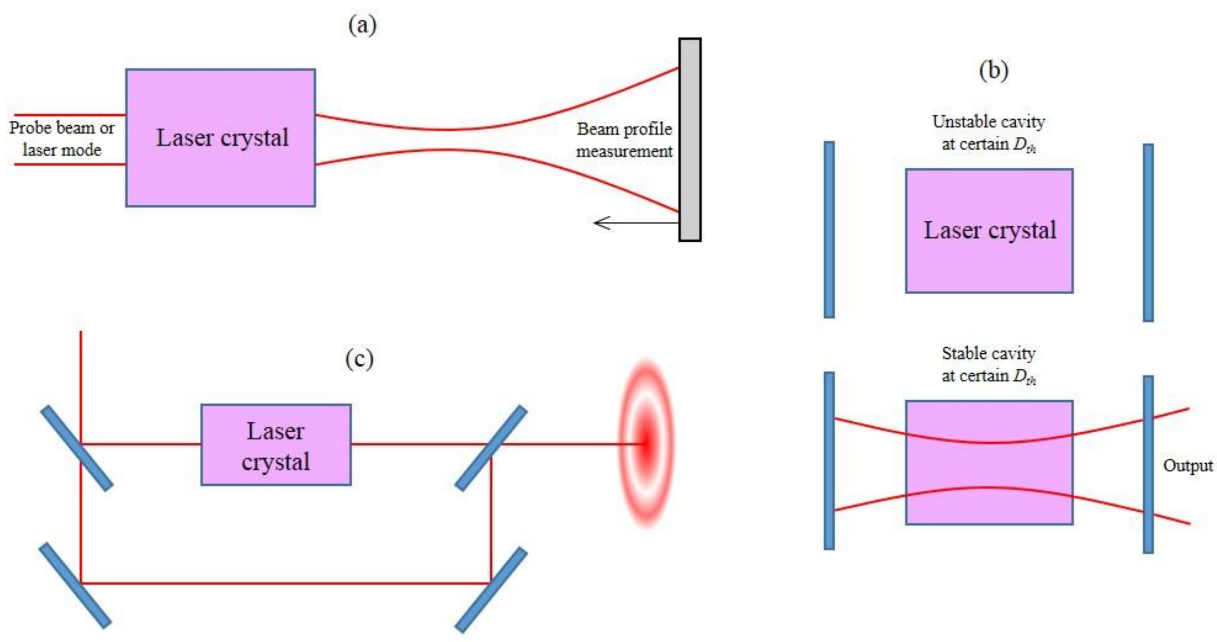

Fig. 2-3 Arrangements of different thermal lens measurement methods. (a) Geometrical method based on intensity profile measurement; (b) stability condition; (c) interferometric method.

Therefore, this chapter utilizes geometrical method where the beam width measurements similar to Fig. 2-3(a) are used with ABCD matrix analysis in order to calculate the dioptric power of the thermal lens inside the laser crystal. Several sets of FEA simulations were also done to study different aspects of the experimental results.

2.3 Absorption of Nd:YVO_4 crystal under different pump wavelengths

It is important to mention the different values of absorption at the four main absorption lines at 808, 880, 888, and 914 nm which will be used in finite element analysis calculation in section 2.5. For a 4-level system as in the case of neodymium lasers, the assumption of exponential decay is valid for the pump power inside the crystal since the absorption saturation does not occur [8]. First of all, absorption cross-section (σ_{abs}) describes the probability of the absorption process. Consider a pump light incident on to a laser crystal with area *A* and thickness *dz* with dopants concentration *N*. Then the number of dopant ions (Nd^{3+}) illuminated by the pump is $N \cdot A \cdot dz$. The change in light intensity (*I*) due to the probability of light being absorbed across the thickness *dz* is

$$-dI = \frac{I\sigma_{abs}NA}{A}dz \tag{2-6}$$

which, through integration on both sides, gives the Beer-Lambert Law.

$$I = I_0 \exp(-\sigma_{abs}Nz) \tag{2-7}$$

This is related to the unsaturated (unbleached) absorption coefficient through

$$\alpha = N\sigma_{abs}. \tag{2-8}$$

The dopant concentration of Nd:YVO_4 is usually given in terms of molar percentage of the number of Y^{3+} ions replaced by the Nd^{3+} ions. For a 1% doped Nd:YVO_4, this number is equal to $1.24\times10^{20}/cm^3$. Due to the laser gain medium being non scattering, absorption inside the crystal can be accurately described by the equation (2-7). Table 2-1 provides the values for peak and average absorption cross-section at all wavelengths of interest.

Table 2-1. Absorption cross-sections of Nd:YVO_4 crystal with 1% doping concentration [10,11]

Wavelength	FWHM (σ) (nm)	Peak abs (σ)	Average σ_{abs} (σ) across FWHM	FWHM (π) (nm)	Peak abs (π)	Average σ_{abs} (π) across FWHM
808	1.68	14.03	9.26	2.732	32.0	18.5
880	3.05	5.02	3.38	2.70 nm	13.41	8.54
888	4.56	1.66	1.145	3.19 nm	1.228	0.711
914	**4.63**	**0.453**	**0.394**	**4.6 nm**	**0.567**	**0.453**

As can be seen from table 2.1, there are large differences between the absorption cross-sections between two polarizations ($\sigma_{abs,\sigma}$ and $\sigma_{abs,\pi}$), the largest one reaching 1:1.5 ratio at 880 nm. In a fiber-coupled diode-pumped system the pump is generally randomly polarized meaning that the laser diode provides 50% power for π- and σ- polarization over a period of time. Taken into account various real experimental setups, however, there are multiple factors involved which perturb the steady-state operation such as mechanical vibration, twisting, and stress in the optical fiber all of which can change the polarization components of the pump and could lead to a lower stability. At 914 nm, the pump experiences smaller changes in absorbance. The first derivative of equation (2-7) rewritten in terms of power is

$$\frac{dP_{abs}}{dz} = P_0 \sigma_{abs} N \exp(-\sigma_{abs} N z) \tag{2-9}$$

which describes the power absorbed at each position inside the gain medium. Fig 2-4 shows the power deposited into the crystal from two different polarizations.

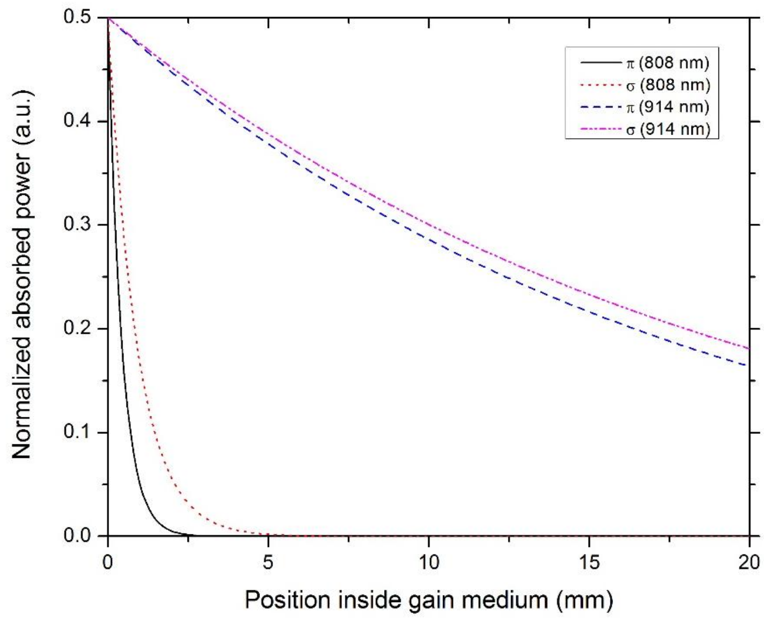

Fig. 2-4 Normalized absorbed power for each polarization for pumping at 808 and 914 nm

Clearly, in the 808 nm pumping case the pump power is absorbed in an order of magnitude shorter crystal length and any fluctuation between the two polarizations due to perturbations could cause more instability than pumping at 914 nm.

2.4 Thermal lensing experiment

The first design constraint for all of the upcoming experiments which are all end-pumped solid-state laser systems is the overlapping or 'mode-matching' between the volume of the pump beam from the fiber-coupled laser diode and the oscillating laser mode inside the laser cavity. Due to the significantly different quality of the two light beams, the basic concepts of Gaussian beam and beam quality are given in section 2.4.1.

2.4.1 Gaussian beam and mode-matching

Considering one frequency or one of the fundamental resonator modes traveling inside the laser cavity, the representation of electric field (U) with paraxial approximation is

$$U(r,z) = A_0 \frac{w_0}{w(z)} \exp\left(-\frac{r^2}{w^2(z)}\right) \exp\left(-jkz - jk\frac{r^2}{2R(z)} + j\varphi(z)\right) \tag{2-10}$$

where k is the wavenumber, w_0 is the initial radius where the intensity drops to $1/e^2$ (≈ 0.135) of the maximum value at the center, z is the distance along the propagation direction from the beam waist, w is the radius of the propagating beam defined as

$$w(z) = w_0 \sqrt{1 + \left(\frac{z}{z_R}\right)^2} \tag{2-11}$$

and Z_R is the Rayleigh range defined as

$$z_R = \frac{\pi w_0^2}{\lambda}, \tag{2-12}$$

$$R(z) = z\left[1 + \left(\frac{z_R}{z}\right)^2\right], \tag{2-13}$$

$$w_0 = \sqrt{\frac{\lambda z_0}{\pi}}, \tag{2-14}$$

R(z) is the radius of the wave front of the propagating Gaussian beam, and λ is the wavelength the propagating beam. A Gaussian beam can be fully described by the divergence of the beam (θ) and the beam waist (w_0), meaning that the product of the two parameters is constant. This leads to the definition of the beam quality parameter or M-squared (M^2) as

$$M^2 = \frac{\pi}{\lambda}\theta w_0 \tag{2-15}$$

which equals to 1 for a perfect Gaussian beam. To take into account the deviation from the perfect Gaussian beam shape, a particular beam can have the M^2 value larger than 1. For example, the comparison between the light beams with M^2 values equal to 1, 25, and 50 is shown in Fig. 2-5.

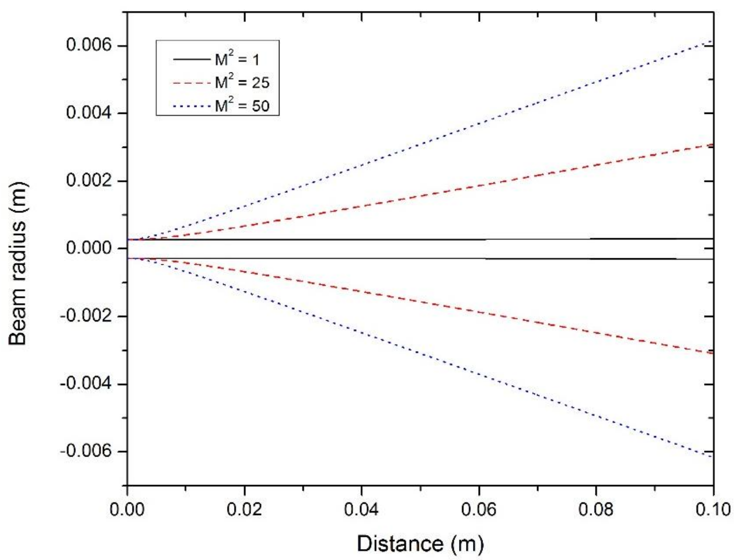

Fig. 2-5 Evolution of a beam radius with respect to distance for M^2 = 1, 25, and 50

The Gaussian beam radius with the M^2 factor taken into account then becomes

$$w(z) = w_0\sqrt{1+\left(\frac{M^2\lambda z}{n\pi w_0^2}\right)^2} \; . \tag{2-16}$$

Even though the pump sources for the end-pumped solid-state lasers generally use a fiber-coupled laser diode, the propagation modes especially for single-mode fibers are very close to a Gaussian shape. Therefore Gaussian approximation can be used to calculate the beam propagation in this case.

For a commercially available, fiber-coupled laser-diode module, the value for numerical aperture (*NA*) and core diameter of the laser diode module are usually given by the manufacturer. *NA* is defined as $n\cdot \sin(\theta)$ where θ is the divergence angle from the fiber core. For a small angle of divergence,

$$M^2 \cong \frac{\pi \cdot NA \cdot d_{core}}{2\lambda} \tag{2-17}$$

where d_{core} is the fiber core diameter similar to the beam waist in free space. The pump module used in this thesis had a multimode fiber with a low NA of around 0.118, core diameter of 110 μm, and the M^2 value of 22.3.

In most of the lasers higher order modes are usually avoided by design of good mode-matching. The mode-matching condition (for the best beam quality M^2) requires the volume of the fundamental mode (TEM_{00}) beam of the resonator to match approximately with the volume occupied by the pumping beam. Spherical aberration from the thermal lensing are also negligible while the laser mode is kept smaller than the pumped area. Due to the higher M^2 of the pump (low beam quality of fiber-coupled laser-diode as the pump source), the smallest pump spot size is limited by the overlapped volume. When the laser mode size radius is 275 μm and fully overlaps with the pump at the center of the crystal, the mode size mismatch at the end-face of the 12-mm-long crystal is less than 11.1% as shown in Fig. 2-6.

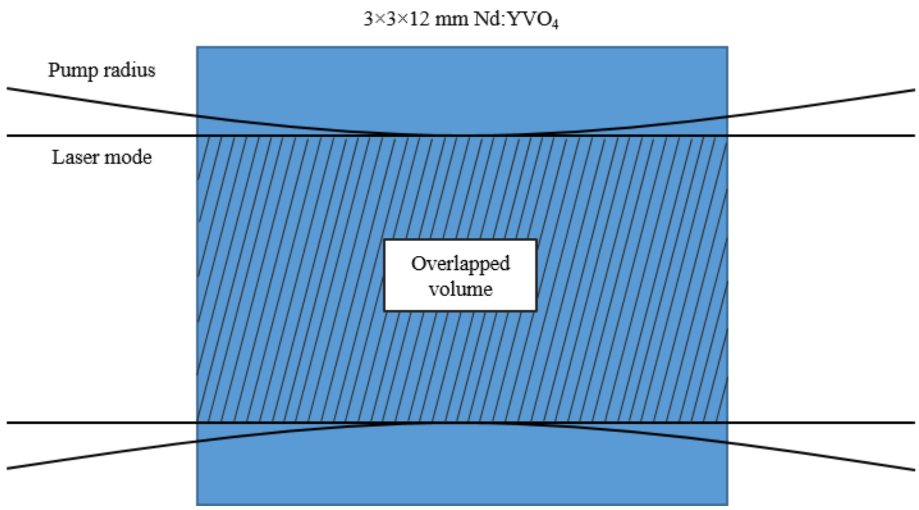

Fig. 2-6 Overlap of laser and pump mode sizes (mode matching) inside the laser gain medium.

For a representation of mode-matching quality, we start with the normalized pump volume,

$$\iiint r_p(r,z)dV = 1 \tag{2-18}$$

with normalized pump intensity distribution, $r_p(r,z)$, represented by

$$r_p(r,z) = \frac{2\alpha}{\pi w_p^2} \exp\left(-\frac{2r^2}{w_p^2}\right) \eta_{abs} \exp(-\alpha z) \tag{2-19}$$

where η_{abs} equals to 1/(1-exp(-αl)) and is the normalizing factor for the absorbed power exp(-αz) and similarly the normalized laser mode volume,

$$\iiint s(r,z)dV = 1 \tag{2-20}$$

with normalized cavity mode intensity distribution, $s(r,z)$, where

$$s(r,z) = \frac{2}{\pi w_{Laser}^2 l} \exp\left(-\frac{2r^2}{w_{Laser}^2}\right) \tag{2-21}$$

where l is the length of the laser gain medium. The maximum value for mode-matching occurs when both beams are in fundamental Gaussian mode (TEM_{00}) and $M^2 = 1$,

$$\iiint s(r,z) r_p(r,z) dV = \frac{2}{l\left(w_{Laser}^2 + w_p^2\right)\pi}. \tag{2-22}$$

With the assumption of Gaussian beams for both pump and resonator mode with M^2 taken into account, mode-matching quality (η_m) can then be quantified as [7]

$$\eta_m = \frac{\pi l\left(w_{Laser}^2 + w_p^2\right)}{2} \iiint s(r,z) r_p(r,z) dV \tag{2-23}$$

This quantification of the mode-matching quality between the pump and laser modes shows us that in order to obtain the optimum results in diode-pumped laser, η_m should be as close to unity as possible which usually can be obtained with a good beam quality from the pump laser diode. In the following sections, three sets of laser diodes with different performance were used, one for Chapter 2, one for Chapter 3, 4, and 5, and one for Chapter 6.

2.4.2 Cavity design and parameters

With ABCD matrices formulation [12], a laser resonator design was done by properly choosing lens system and distances between each elements. Optical resonator design is an iterative process and there is no unique solution since the same round trip ABCD matrix of the optical resonator can be obtained from multiple different lens system. One simple example is the possibility of artificially extending the laser cavity by a telescope configuration [13] which can extend a stable resonator indefinitely. This can be useful in some situations such as reducing the repetition rate in pulsed operation. Additional features for resonator design can be specified such as certain values of beam radii at certain optical components, high tolerance against misalignment, or having particular cavity length to control the repetition rate.

Therefore, the design constraints for thermal lensing measurement are as follows: 1) small change in mode-matching of pump and laser mode while thermal lens power changes due to the change in absorbed power and 2) observable mode size changes at the output coupler. These two requirements can be met using a 3-mirror cavity.

In the laser resonator design process for thermal lensing experiment, the effective thermal lens was treated as a lens positioned at the center of the laser crystal for ABCD matrix calculation as shown in the equivalent laser resonator schematic in Fig. 2-7. The picture was from reZonator software.

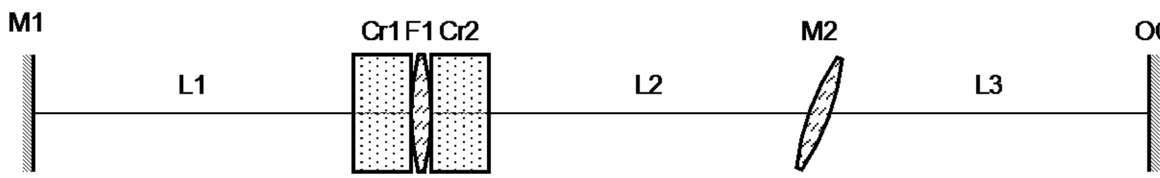

Fig. 2-7 Schematic diagram of the laser cavity used in ABCD matrix calculation.

where, M1 is the first mirror, L1, L2, and L3 are the propagation distances in free space, Cr1 and Cr2 are the first and second halves of the laser crystal, F1 is the effective thermal lens, M2 is the convex lens equivalent to a concave mirror used in the experiment, and OC is the output coupler.

According to the design constraint listed above, the laser resonator in this section was designed in such a way that the cavity mode size at the output coupler can change freely with the strength of the induced thermal lens while having small changes in size at the pump waist inside the crystal to ensure relatively constant mode matching in order to maintain a good beam quality. The parameters of each optical element are given in Table 2-2.

Table 2-2 Parameters for optical resonator in this section

Parameter	Mirror (M1)	Space (L1)	Crystal (Cr1)	Thermal lens (F1)	Crystal (Cr2)	Space (L2)	Curved mirror (M2)	Space (L3)	Output mirror (OC)
	Optical elements								
Distance (mm)	-	21	6	-	6	329	-	265	-
Focal length (mm)	-	-	-	500	-	-	500	-	-
n	-	1	2.17	-	2.17	1	-	1	-
Transfer matrix	$\begin{bmatrix} 1 & 0 \\ 0 & 1 \end{bmatrix}$	$\begin{bmatrix} 1 & 21 \\ 0 & 1 \end{bmatrix}$	$\begin{bmatrix} 1 & \frac{6}{2.17} \\ 0 & 1 \end{bmatrix}$	$\begin{bmatrix} 1 & 0 \\ -\frac{1}{500} & 1 \end{bmatrix}$	$\begin{bmatrix} 1 & \frac{6}{2.17} \\ 0 & 1 \end{bmatrix}$	$\begin{bmatrix} 1 & 329 \\ 0 & 1 \end{bmatrix}$	$\begin{bmatrix} 1 & 0 \\ -\frac{1}{500} & 1 \end{bmatrix}$	$\begin{bmatrix} 1 & 265 \\ 0 & 1 \end{bmatrix}$	$\begin{bmatrix} 1 & 0 \\ 0 & 1 \end{bmatrix}$

The designed laser mode size throughout the resonator is plotted in Fig. 2-8 where T designates the tangential plane which is the plane containing resonator's elements (parallel to the optical table) and S designates the sagittal plane which contains the element's optical axis.

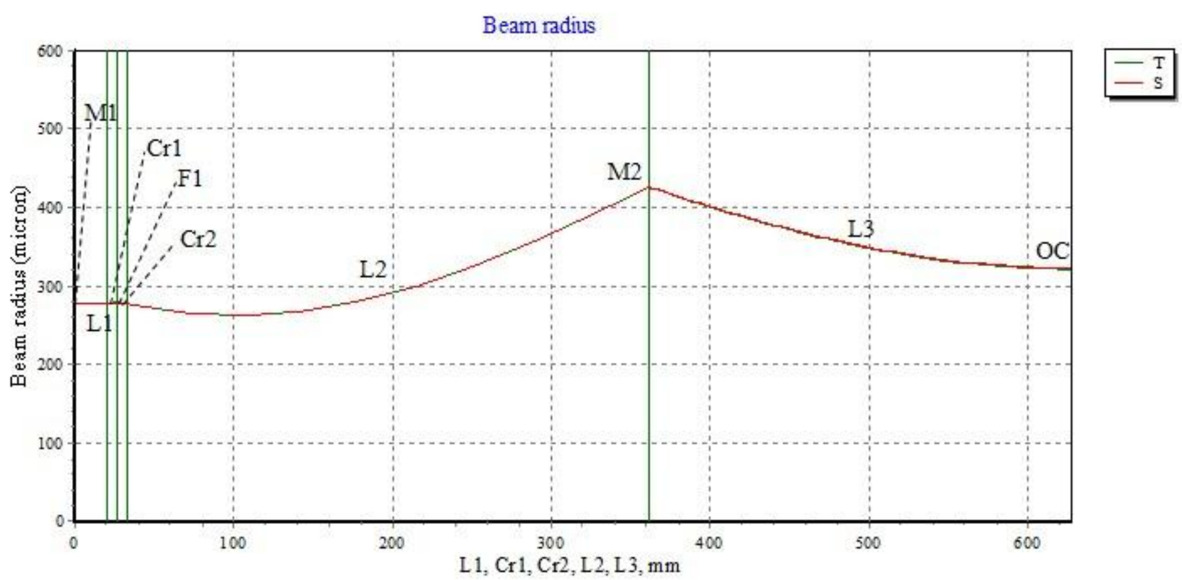

Fig. 2-8 Designed laser beam radius inside a stable resonator.

The beam size at the center of the gain medium and at the output coupler (OC) with respect to the different thermal lens values are shown in Fig. 2-9.

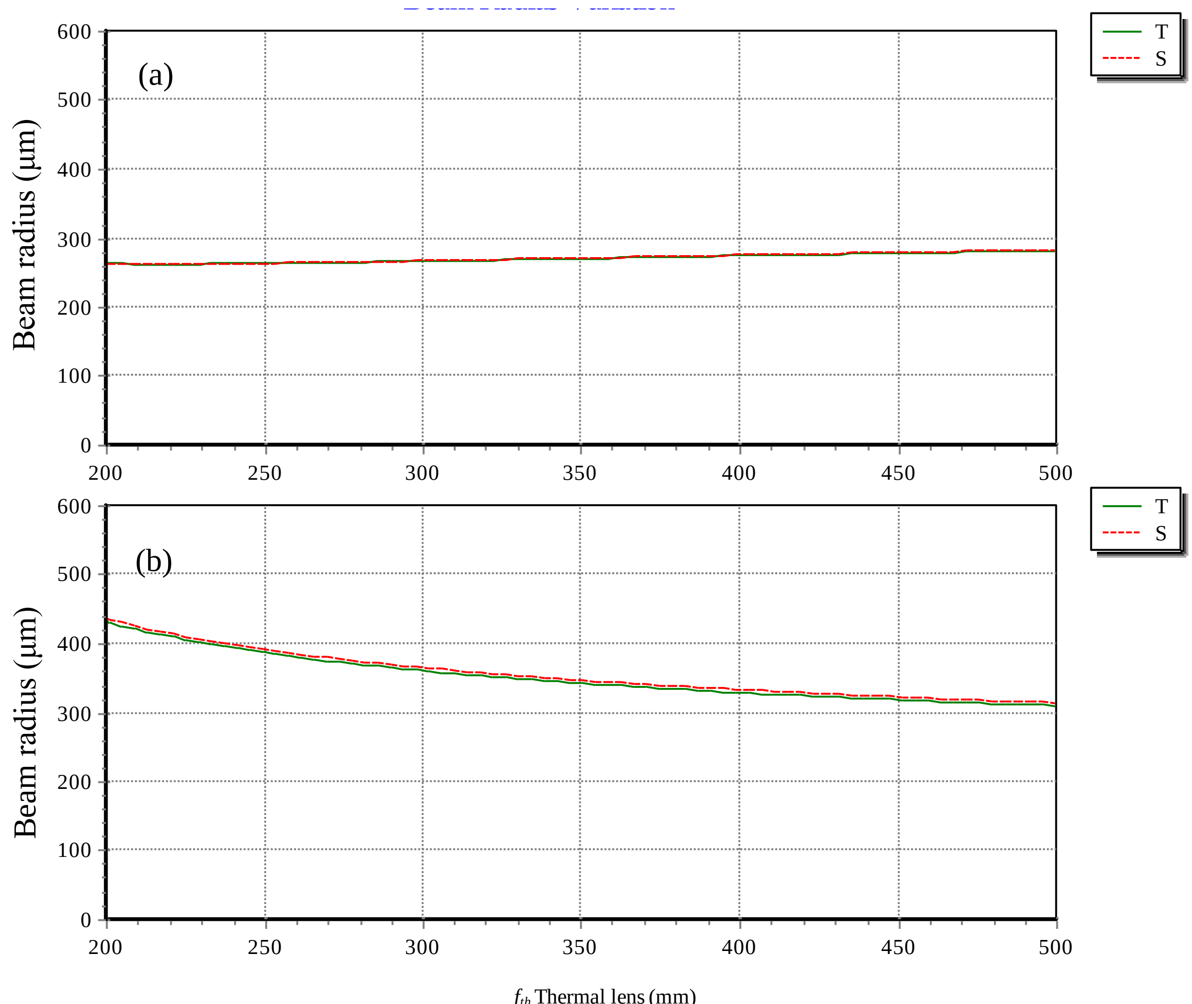

Fig. 2-9 Laser beam radius at the center of the crystal (a) and at the output coupler (b) with respect to the focal length of the thermal lens.

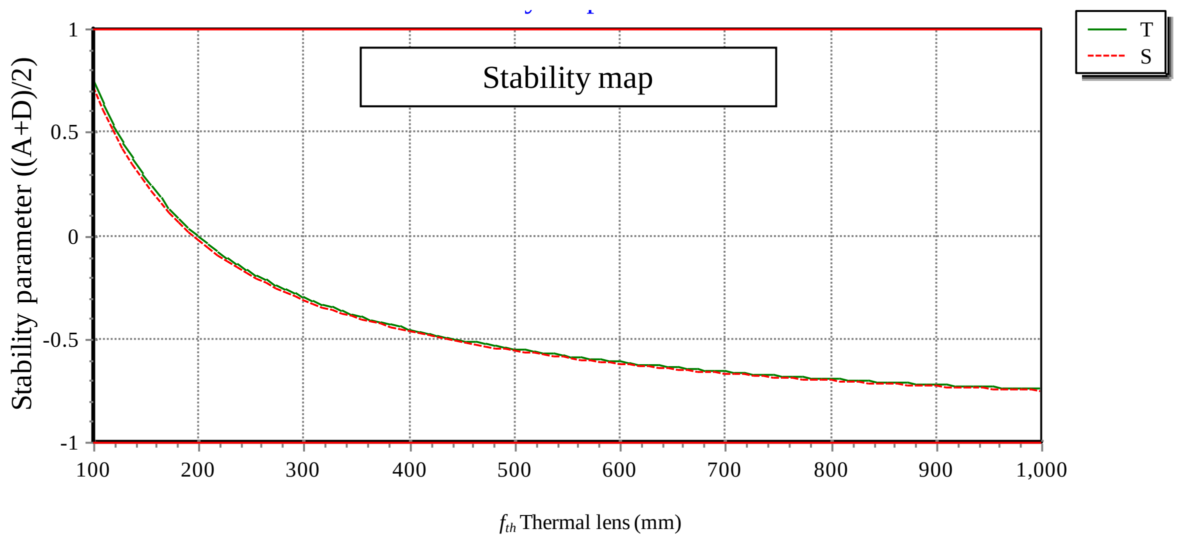

Fig. 2-10 Stability map of the designed resonator with respect to the focal length of the thermal lens.

As shown in the stability map in Fig. 2-10, the designed cavity is stable (i.e. stability parameter lies within ±1) from thermal lens values of 100 to more than 1000 mm.

2.4.3 Pump performance and its absorption

A fiber-coupled laser diode at 914 nm from iPG Photonics was used as the pump source. The core diameter of the fiber was 110 μm and numerical aperture was 0.118. The output power from the diode and its corresponding center wavelength over the operational output power range are shown in Fig. 2-11. The operating voltage of the diode was 3.2 V. The maximum output power obtained from this laser diode was 32.0 W at 12 A of drive current. The wavelength of the laser diode starts at 905 nm at threshold and continues to increase with the drive current until 916.5 nm with spectral width of 3.8 nm.

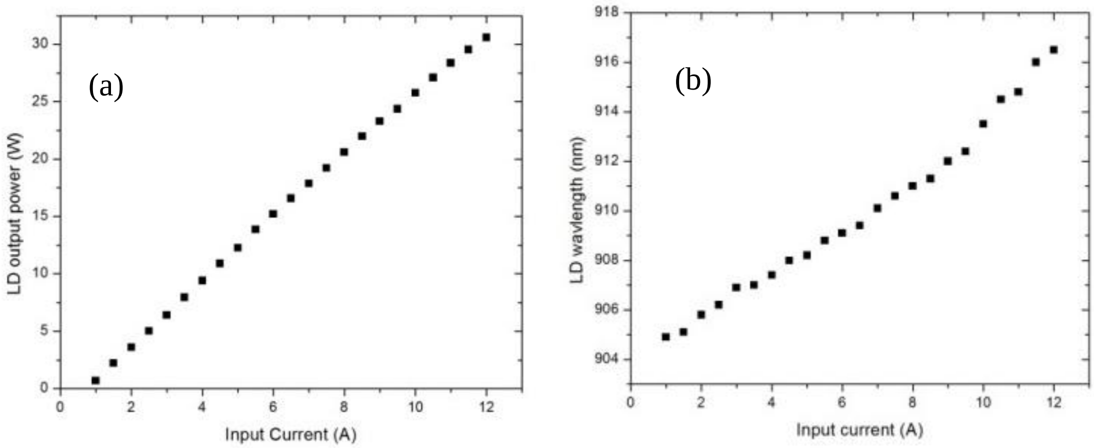

Fig. 2-11 (a) Output power versus drive current of the laser diode. (b) Output wavelength versus drive current of the laser diode.

The laser diode power after passing through the Nd:YVO_4 crystal was also measured in order to obtain the absorbed power at different wavelengths as shown in Fig. 2-12. The nonlinearity in relationship between laser diode drive current and absorbed power is due to the crystal absorption spectrum and the shifting of laser diode center wavlength at higher power due to its temperature change.

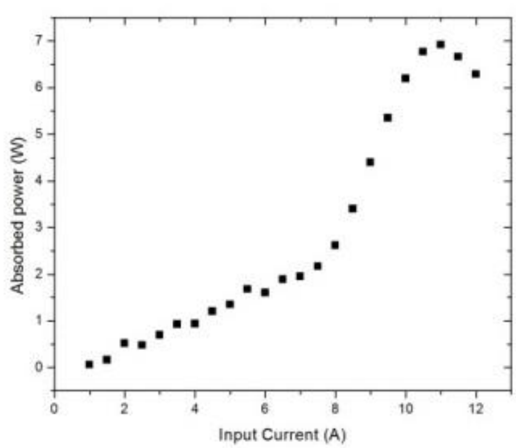

Fig. 2-12. Nd:YVO_4 crystal absorbed power versus the laser diode drive current.

The difference between absorption under lasing and non-lasing conditions was also investigated. As expected from a 4-level laser system, the difference between the two was very small and relatively constant throughout all pump power levels. At maximum pump power (10 A of drive current), the absorption was ~2 % lower under the lasing condition whereas at 5.1 A of drive current, the absorption under lasing condition was ~1% lower than under non-lasing condition.

At 914 nm, the measured absorption coefficient was 0.23 cm^{-1} which is comparable to other literature values considering that the crystal used here had the doping concentration of 0.5% (0.53 cm^{-1} reported by D. Sangla et al. [11] and 0.6 cm^{-1} from X. Ding et al. [14] both for Nd:YVO_4 crystal with 1% doping concentration). Due to the low absorption coefficient of Nd:YVO_4 at 914 nm when compared to other absorption lines, longer crystal, multiple pass pumping scheme, or higher doping concentration must be utilized in order to increase the absorbed pump power further.

2.4.4 Continuous wave (CW) Nd:YVO_4 laser performance

The experimental setup is shown in Fig. 2-13. The Nd:YVO_4 crystal was constantly water-cooled at the flow rate of 1 liter/minute on the top and bottom surfaces at 16° C. The first mirror is a mirror with high reflectivity (HR) at laser wavelength (1064 nm). The laser crystal was anti-reflection (AR) coated at pump (914 nm) and laser wavelengths (1064 nm) on the front and back surfaces. The folding mirror M2 is a concave HR mirror. An output coupler transmittance was 10% and resulted in the highest output power from this laser setup.

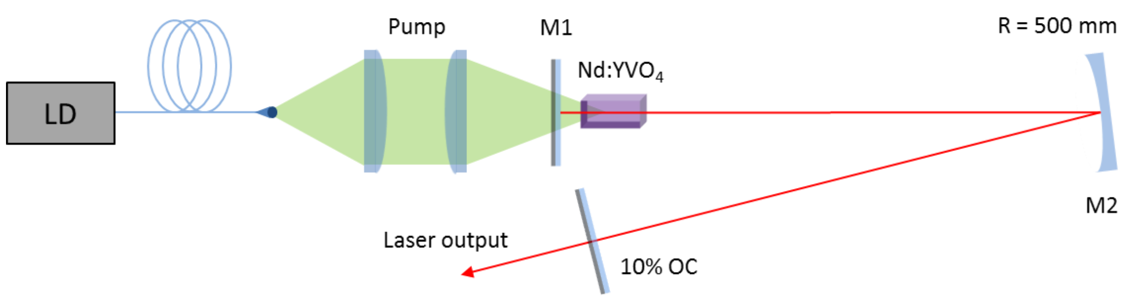

Fig. 2-13. Experimental setup used for CW experiments. M1 is an HR mirror at 1064 nm. M2 is a concave HR mirror. OC is a plane output coupler with 10% transmission.

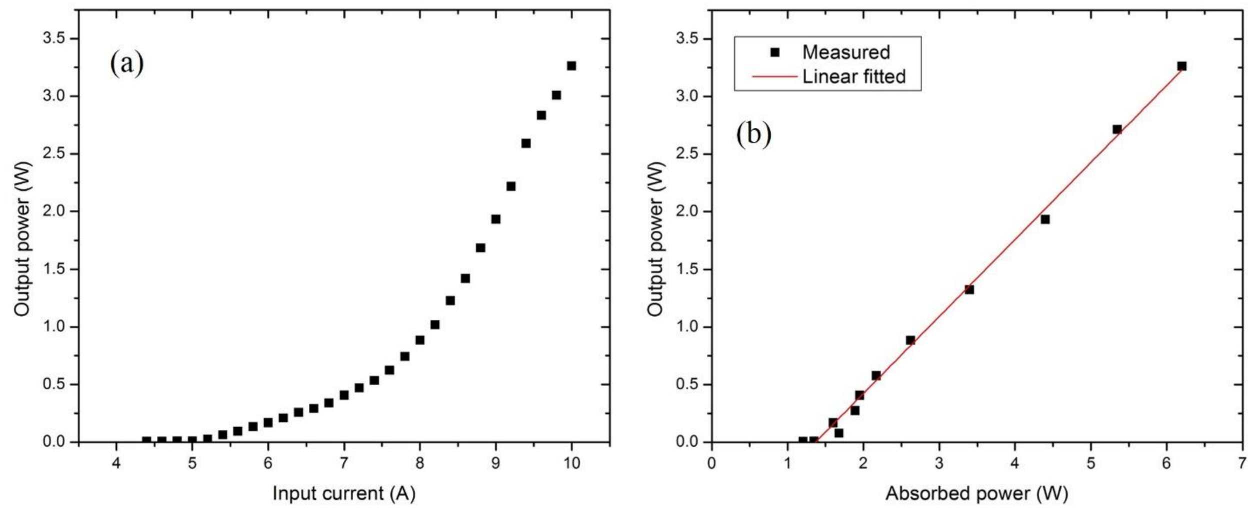

Fig 2-14 (a) CW laser output power versus laser diode drive current. (b) Output power versus the absorbed pump power.

Fig. 2-14 shows the experimental results for the laser output power versus the drive current of the laser diode (a) and versus the absorbed pump power (b). The slope efficiency (η_s) is defined as

$$\eta_s = \frac{dP_{out}}{dP_{abs}}, \tag{2-24}$$

while the optical-to-optical efficiency ($\eta_{o\text{-}o}$) determines the efficiency at specific output power,

$$\eta_{o-o}(x) = \frac{P_{out}(x)}{P_{abs}(x)}. \tag{2-25}$$

The slope efficiency was 66.9%. The laser system produced the highest output power of 3.52W with 56.8% optical efficiency. The laser threshold was at 1.34 W of absorbed pump power.

2.4.5 Thermal lensing measurement and results

Since the thermal lens directly modifies the laser resonator and its stability as explained in the laser cavity design section 2.4.2, the change in beam width of the laser output and beam quality (M^2) factor was also required to identify the effective dioptric power of the induced thermal lens inside the $Nd:YVO_4$ crystal. The experimental setup shown in Fig. 2-15 was used to record the beam radii (spot size radius) and the beam quality factors as the laser beam propagated through the positive lens outside of the laser cavity. A dichroic mirror (DM) with high reflectivity at output wavelength was inserted before all the power, spectra, beam size measurements, etc. to filter out the residual pump light.

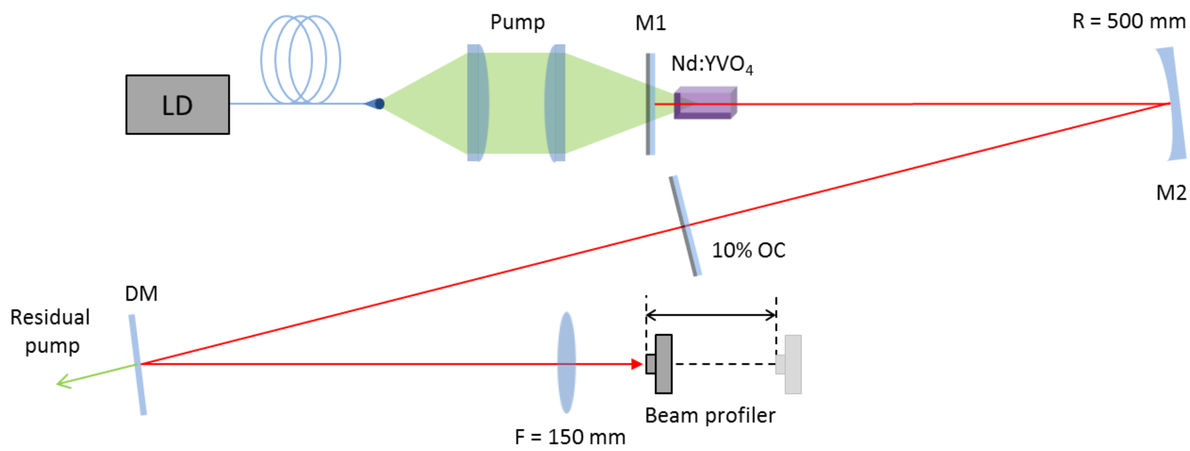

Fig. 2-15 Experimental setup in thermal lensing measurement. DM is a dichroic mirror and a convex lens was added in order to measure beam quality factor (M^2).

A THORLABS slit-based beam profiler was used to measure laser spot size at multiple distances along the z-axis after the focusing lens.

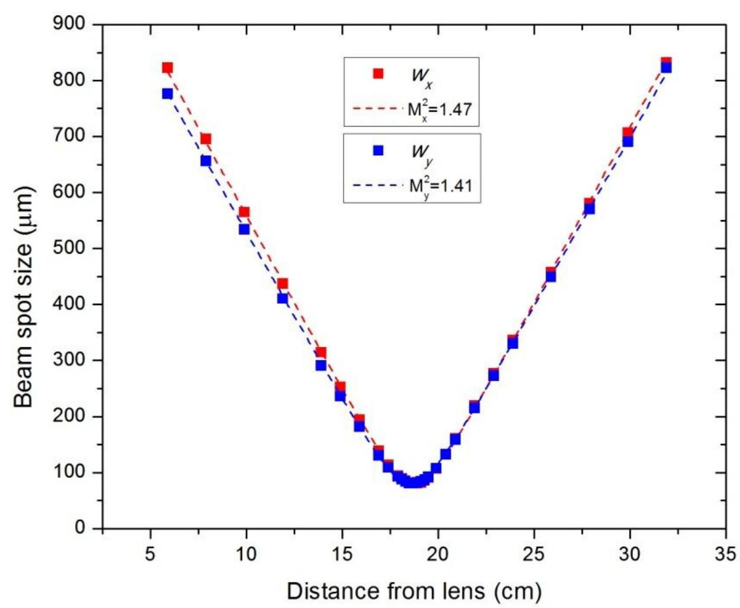

Fig. 2-16 Measured beam spot sizes and their corresponding beam quality factor (M^2).

The beam quality factor (M^2) was then calculated by fitting the measured spot sizes as shown in Fig. 2-16 with equation (2-16). The M^2 factor was found to be 1.47 at the highest output power.

Fig. 2-17 (a) shows the evolution of the beam spot size at the beam waist after the focusing lens as output power increases. The change in the beam size and shape is an evidence of the thermal lens change inside the laser cavity. The M^2 factors were also measured for each output power level and are shown in Fig 2-17 (b).

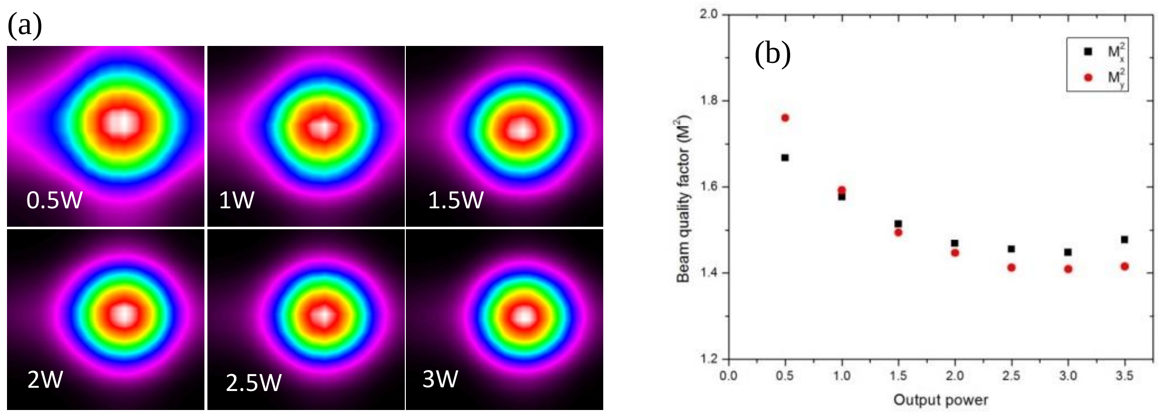

Fig 2-17 (a) Evolution of beam profile at the same position as the output power changed. (b) The M^2 values at difference output power level.

The system was allowed to reach thermal equilibrium at each power level where a change in output power and beam spot size no longer occur (> 5 minutes) before each beam spot size measurement.

The equivalent laser cavity and laser beam propagation simulated using the ABCD matrix calculation with commercial LASCAD software is illustrated in Fig. 2-18. The thermal lens was modeled as a thin lens with variable focal length inside the laser crystal.

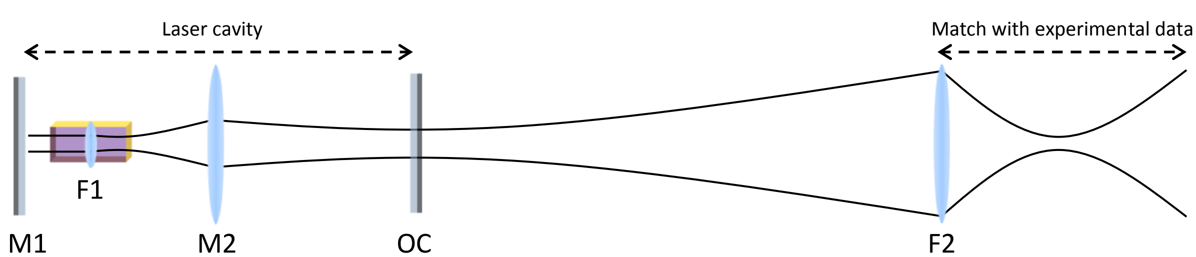

Fig. 2-18 The equivalent laser cavity used in LASCAD software.

With the recorded beam spot size after the positive lens (F2) and the M^2 factor for each power level from the experiment, the dioptric power of the effective thermal lens was calculated as a function of output power [15]. The focal length of thermal lens at each output power is shown in Fig. 2-19 (a) and dioptric power is shown in Fig. 2-19 (b). FTx and FTy refers to the horizontal and vertical focal lengths of the thermal lens, respectively.

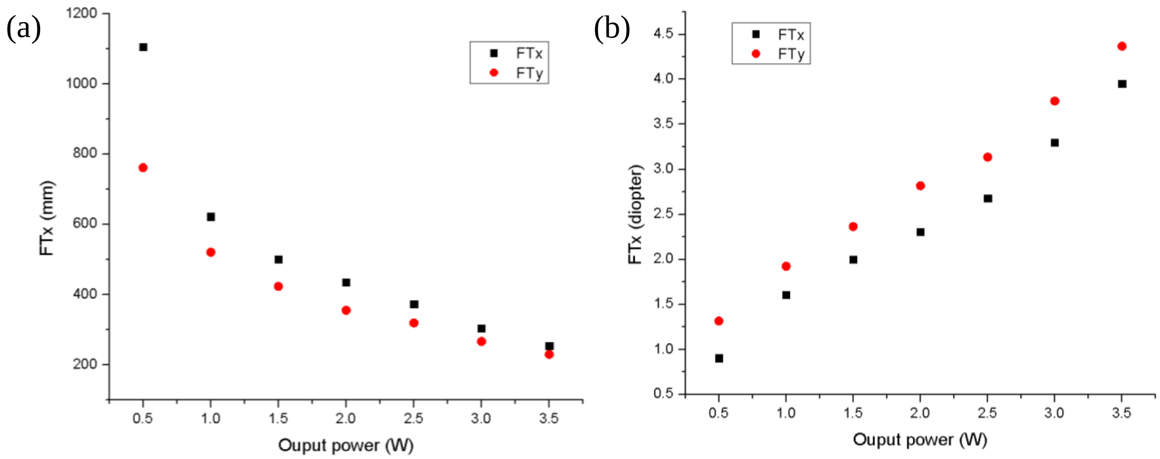

Fig. 2-19 Calculated (a) focal length and (b) dioptric power of thermal lens.

The calculated thermal lens dioptric powers were 3.95 m^{-1} horizontally and 4.37 m^{-1} vertically at 3.52 W of output power. Thermal lensing was stronger in the vertical direction because of the larger difference in temperature gradient due to the direction of cooling. When compared to the previous records of thermal lensing in an a-cut $Nd:YVO_4$ crystal pumped at 808 nm [17,19], this method of pumping the $Nd:YVO_4$ crystal at 914 nm created a weaker thermal lens at the same level of absorbed pump power. This will be discussed in more detail in section 2.6.

2.5 Finite element analysis (FEA) simulations

With proper boundary conditions, crystal thermal properties, and dimensions, FEA method can be used to simulate the temperature and stress fields inside the laser crystal by solving the complex heat diffusion differential equation. FEA of thermal lensing under the same pumping geometry as the experiment (275 μm pump beam waist radius) was done to verify the accuracy of the experimental results using the commercially available LASCAD program to calculate the temperature distribution, deformation, and stress. The parameters used for the FEA calculations are given in table 2-3.

Table 2-3 Parameters used in the FEA simulation (a-cut crystal) [7,16]

Parameters	Values	Parameters	Values
K_x	5.23 W/m·K	n_x	2.165
K_Y	5.1 W/m·K	n_y	1.957
K_z	5.1 W/m·K	n_z	1.957
α_x	11.37 $\times10^{-6}$ K^{-1}	dn/dT	8.5 $\times10^{-6}$ K^{-1}
α_y	4.43 $\times10^{-6}$ K^{-1}	α_{abs} (absorption coefficient)	0.23 cm^{-1}
α_z	4.43 $\times10^{-6}$ K^{-1}	w_0 (radius)	275 µm
Young's modulus	133 GPa	Pump beam divergence	23 mrad
Poisson's ratio	0.33	Distance of pump waist from left end face	6 mm

K_x, K_y, K_z are the coefficients of thermal conductivity, α_x, α_y, α_z, are the expansion coefficients, and n_x, n_y, n_z are the refractive indices.

The resulting temperature profile is shown in Fig. 2-20.

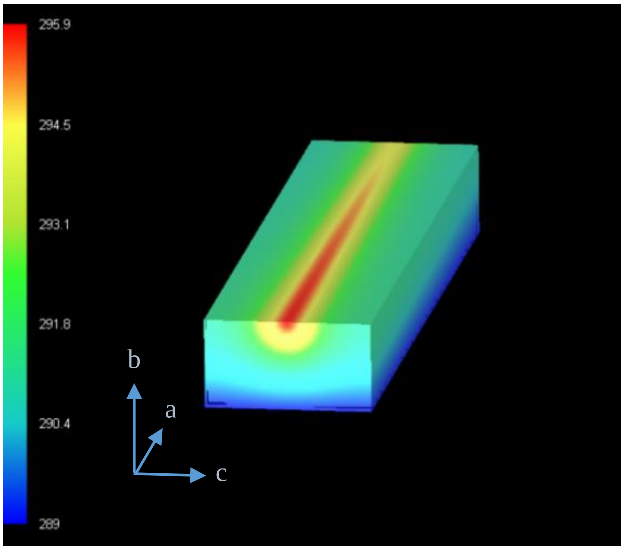

Fig. 2-20 Temperature profile of 914 nm pumped Nd:VYO_4. A lower half of the crystal is shown.

The results from FEA are given in the form of refractive index profile along the x- (coincides with the c-axis) and y- (coincides with the b-axis) axes as shown in Fig. 2-21. The a, b, and c axes are labeled to show the crystal orientation compared to Fig. 1-1.

A parabolic fit of the temperature distributions was calculated for the effective focal length of the thermal lens. As can be seen, the refractive index profiles over the cross-sectional area of the pump and resonator modes (-0.275 to +0.275 mm) closely follows the parabolic shape. The calculated thermal lens dioptric powers were 3.798 m^{-1} horizontally and 4.025 m^{-1} vertically at 6.55 W of absorbed pump power.

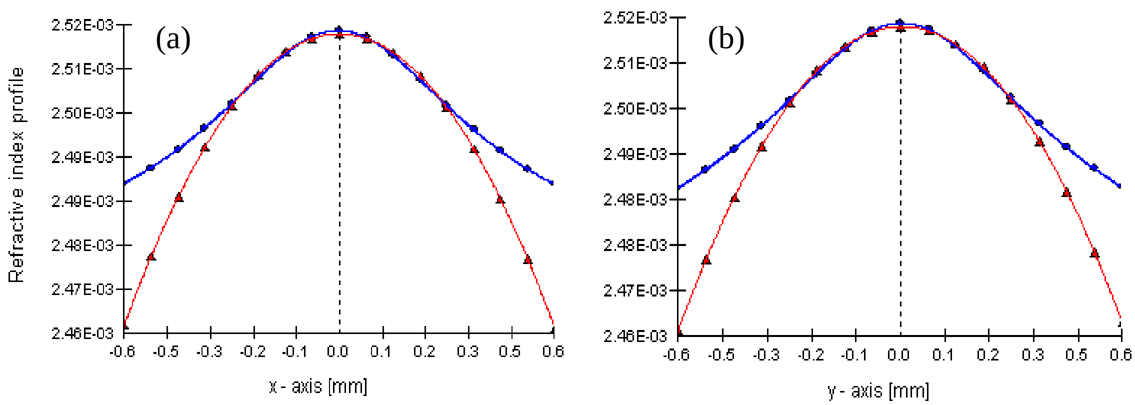

Fig. 2-21 Refractive index profiles calculated from FEA (lines with solid dots) and their parabolic fit (lines with solid triangles).

In Fig. 2-22 FEA simulation results were compared to the dioptric powers of thermal lens obtained from the ABCD matrix calculations from the experimental data to verify the accuracy of the measurement. The simulated thermal lens dioptric power is in good agreement with experimental data.

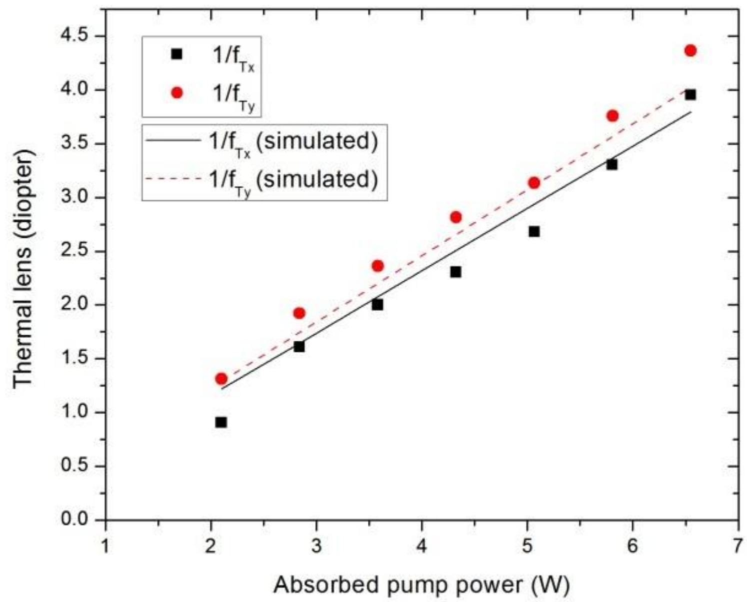

Fig. 2-22 Calculated thermal lens power and FEA analysis simulation results (line) for horizontal and vertical direction.

FEA was also done for 888, 880, and 808 nm pumping wavelengths under the same pumping condition (absorbed pump power, pump spot size, and pump divergence) as in 914 nm pumping case. The differences between pumping at different wavelengths are quantum defect and absorption coefficient (α_{abs}). The absorption coefficients (α_{abs}) of 0.5% doped a-cut $Nd:YVO_4$ crystal used in the FEA simulations were 0.23, 0.73, 5.3, and 7.0 cm^{-1} and the fractional thermal loadings were 14.1, 16.5, 17.2, and 24.1% for 914, 888, 880, and 808 nm pumping schemes, respectively [2,3,11,18]. The simulated results are compared in Fig. 2-23 showing the highest thermal lens dioptric power for 808 nm pumping as expected.

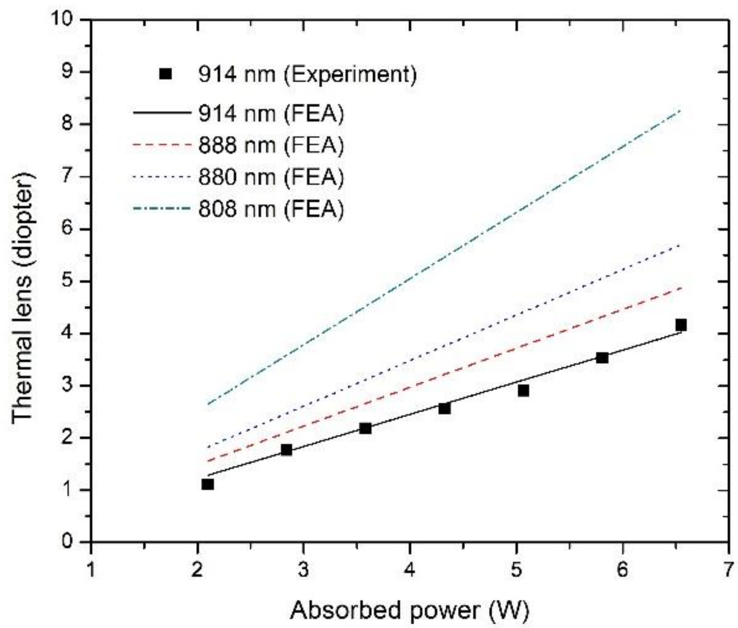

Fig. 2-23 Thermal lens dioptric powers simulated from FEA with four different pumping schemes and the one experimentally obtained from 914 nm pumping.

Using the laser crystal thermal lens sensitivity factor (M_{th}) defined as

$$M_{th} = \frac{dD_{th}}{dP_{abs}} \tag{2-26}$$

which describes how much the optical power of the induced lens changes due to the absorbed pump power, the results above show that thermal lens power with 914 nm pumping is reduced by a factor of 2.1 when compared with the 808 nm pumping.

Temperature distribution plots inside the gain media under different pump wavelengths obtained from FEA simulations at 6.55 W of absorbed pump power are shown in Fig. 2-24. Due to the low absorption coefficient at 914 nm, the heat load was spread in a larger volume, thus minimizing stress and temperature rise. This reduction in mechanical stress and temperature gradient changed the geometry of the thermal lens and ultimately reduced its dioptric power.

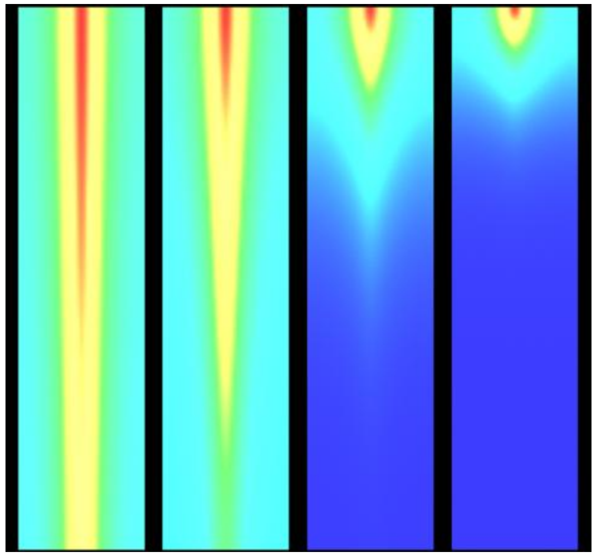

Fig. 2-24 Temperature distribution plots from FEA simulations for 0.5 at. % Nd:YVO_4 pumped with (a) 914, (b) 888, (c) 880, and (d) 808 nm at the same level of the absorbed pump power of 6.55 W(heat load). The highest temperatures are 295.9, 299.7, 327.1, and 398.1 °C, respectively.

To verify the last statement, the contribution of lens geometry and crystal surface deformation on the final strength of the thermal lens were investigated. Multiple sets of FEA calculation were done under the condition that the crystal was under the same heat load (Q). The pump power in the calculation was changed accordingly to accommodate this restriction.

Chosen from the two extreme examples to illustrate the effect of thermal lens shape and deformation, the pump absorption geometry in case of the 808 nm pumping was changed by varying the absorption coefficient from 1 cm^{-1} to 10 cm^{-1} while the fractional thermal load (η_h) was kept constant at 24.1%. This assumption holds true in the case of small pump wavelength shift away from the absorption peak, in which case the minute change of pump wavelength negligibly affects the quantum defect.

The resulting (averaged) thermal lens dioptric powers (D_{th}) are 7.07 m^{-1} for α equal to 1 cm^{-1} and for 8.83 m^{-1} for α equal to 10 cm^{-1}. The temperature and z-displacement profiles designating the crystal expansion are shown in Fig. 2-25 (a) and (b), respectively.

(a) (b)

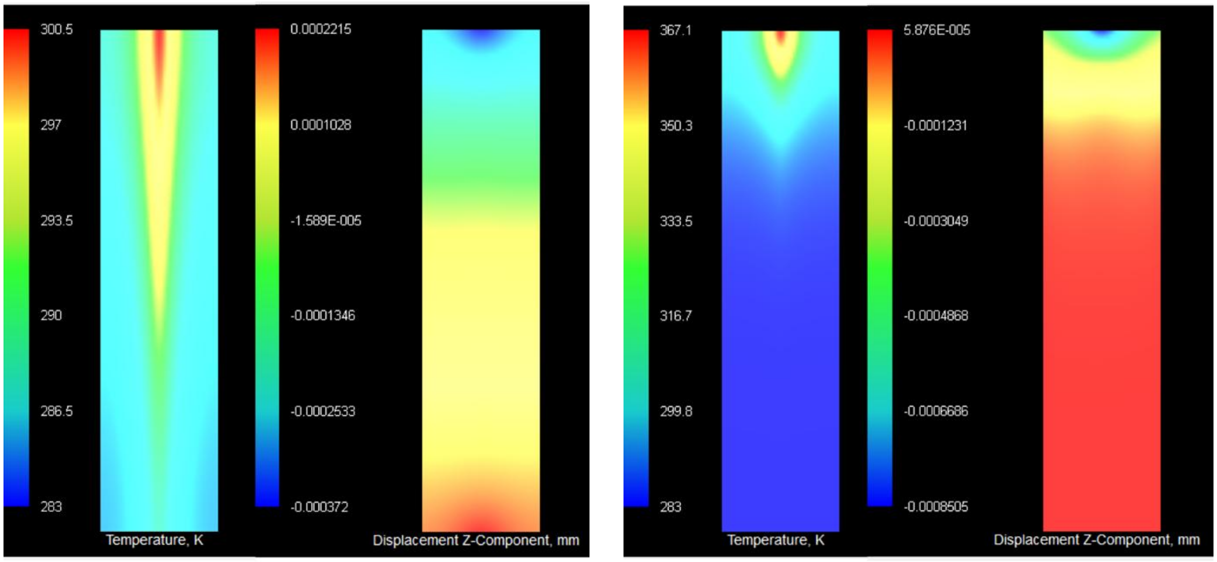

Fig. 2-25 Temperature distribution and z-displacement for crystals with absorption coefficients equal to (a) 1 cm^{-1} and (b) 10 cm^{-1} at the same heat load (Q).

When the surface deformation (z-displacement) was removed from the simulation leaving only the effect of the change of refractive indices as can be seen in Fig. 2-26, the resulting D_{th} became 6.47 m^{-1} and 6.62 m^{-1}, respectively.

(a) (b)

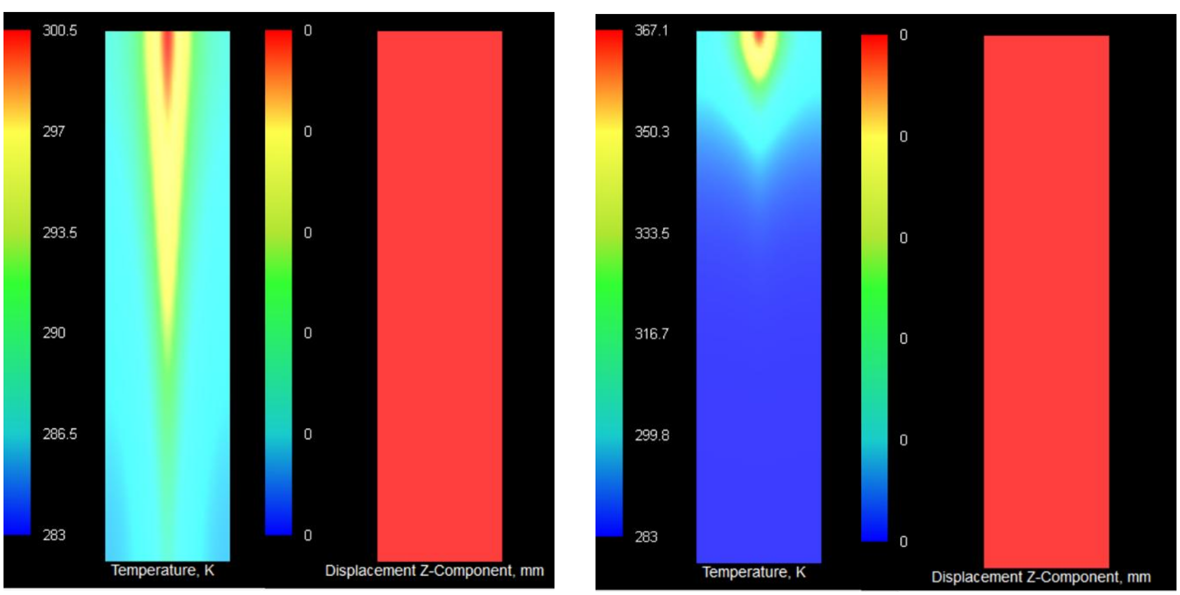

Fig. 2-26 Temperature distribution with z-displacement equals to 0 for crystals with absorption coefficients equal to (a) 1 cm^{-1} and (b) 10 cm^{-1} at the same heat load (Q).

This result shows that the thermal lens geometry had a small effect (≈ 2.4%) over the overall thermal lensing effect when large difference in absorption coefficient is considered. The significant contribution from severe surface deformation at high absorption coefficient (33.4%) was also shown. The results also confirm our statement that by using the pump wavelength with lower absorption, even when under the same heat load, it is beneficial to the resonator in that it can significantly reduce the thermal lensing effect by changing the lens geometry and decreasing the surface deformation.

Another parameter that can also affect thermal lens dioptric power is the pump spot size, since thermal lens dioptric power is inversely proportional to its area as described by equation (2-5). Therefore, thermal lens to some extent can be controlled by the selection of a larger pump spot size albeit at the expense of the increased threshold pump power and thus lower output power.

2.6 Comparison with other results from different pumping wavelengths

Since this is the first experimental measurement of the thermal lensing effect of Nd:YVO_4 under the 914 nm pumping, it is necessary to compare the newly obtained results to other experimentally measured values from other pump wavelengths. Table 2-4 shows the comparison between the reported values of thermal lens from 808 and 888 nm pump wavelengths and the results given in this thesis.

As shown in the analytical solution of the thermal lensing effect in equation (2-5) the resulting thermal lens also depends on the pump area (πw_p^2). Therefore the effect of the pump area on the value of thermal lens dioptric power has to be canceled off before any comparison can be made. In the following comparison in Table 2-4 between the 808 and 914 nm pumping, the parameter $f_{th}/\pi w_p^2$ was used to compare the strength of thermal lens at 6.55 W of absorbed pump power and under lasing condition. The smaller the value of $f_{th}/\pi w_p^2$ translates to the stronger the effect of thermal lensing.

Table 2-4 Reported values of thermal lens under different pump wavelength.

Pump wavelength (nm)	f_{th} (mm)	w_p (µm)	$f_{th}/\pi w_p^2$ (10^3 m^{-1})	Ref.
808	10.9	105	**315**	J. L. Blows et al. [19]
808	670.2	604	**584**	Feng Song et al. [17]
808	590.0	570	**578**	Feng Song et al. [17]
888	1540.8	825	**720**	L. Donagh et al. [18]
914	3715.0	320	**11548**	D. Sangla et al. [11]
914	255.69	275	**1076**	[This work]

As can be seen above, the values of $f_{th}/\pi w_p^2$ suggested that the thermal lensing effect is much stronger under the shorter pump wavelengths. However, the initial estimate from D. Sangla et al. suggested that the thermal lens was 1 order of magnitude lower even with 18.25 times higher absorbed power which is far from our findings [11]. This result is not realistic considering the fact that quantum defect was reduced only by ~40%.

2.7 Conclusion

In this chapter, the thermal lensing effects in a 914 nm diode-pumped $Nd:YVO_4$ laser have been studied in order to assess its strength. FEA simulation was also done to verify the experimentally obtained results and compared the thermal lensing effect with the 914, 888, 880, and 808 nm pumping wavelengths. A comparison was also done under the same absorbed pump power level. The results show that the thermal lens power was significantly reduced because of two reasons: one, the difference in quantum defect and two, the thermal lens geometry. The obtained results indicate that in-band pumping at 914 nm offers significant advantages for the development of high average power $Nd:YVO_4$ and other laser oscillators in continuous wave regime. This concept will be particularly useful for crystals that have poor thermal properties. The current limit to this particular pumping scheme was due to the low amount of the total pump power absorbed (~25% absorption). This was caused by low doping concentration (0.5% at.) of the laser crystal and short crystal length available to us at the time of experiments. For further power scaling, longer crystal, multiple pass pumping scheme, higher doping concentration, higher pump power, or any combination of the above can be utilized in order to increase the absorbed pump power further.

References

[1] A. Sennaroglu, "Experimental determination of fractional thermal loading in an operating diode-pumped Nd:YVO_4 minilaser at 1064 nm," Appl. Opt. 38, 3253 (1999).

[2] F. Song, C. Zhang, X. Ding, J. Xu, G. Zhang, M. Leigh, and N. Peyghambarian, "Determination of thermal focal length and pumping radius in gain medium in laser-diode-pumped Nd:YVO_4 lasers," Appl. Phys. Lett. 81, 2145 (2002).

[3] Z. Xiong, Z. G. Li, N. Moore, W. L. Huang, and G. C. Lim, "Detailed investigation of thermal effects in longitudinally diode-pumped Nd:YVO_4 laser," IEEE J. Quantum Electron. 39, 979, (2003).

[4] X. Huai and Z. Li, "Thermal stress analysis of a Nd:YVO_4 laser medium end pumped by a Gaussian beam," Appl. Phys. Lett. 92, 041121 (2008).

[5] R. Soulard, A. Zinoviev, J. L. Doualan, E. Ivakin, O. Antipov, and R. Moncorge, "Detailed characterization of pump-induced refractive index changes observed in Nd:YVO_4, Nd:$GdVO_4$ and Nd:KGW," Opt. Express 18, 1553 (2010).

[6] Y. R. Peng, Y. Xin, C. D. Ying, C. Fei, L. X. Dong, M. Y. Fei, and Y. J. Hua, "The thermal effect in diode-end-pumped continuous-wave 914-nm Nd:YVO_4 laser," Chin. Phys. B 21(2), 024208 (2012).

[7] W. Koechner, *Solid-state Laser Engineering*, 6th ed. (Springer, 2006).

[8] S. Chénais, F. Druon, S. Forget, F. Balembois, P. Georges, "On thermal effects in solid-state lasers: The case of ytterbium-doped materials," Progress in Quantum Electron. 30(4), 89-153 (2006).

[9] A. Siegman, *Lasers* (University Science Books,Mill Valley, CA, 1986).

[10] R. D. Peterson, H. P. Jenssen, and A. Cassanho, "Investigation of the spectroscopic properties of Nd:YVO_4," in Advanced Solid-State Lasers: Trends in Optics and Photonics Series (Optical Society of America, 2002), paper TuB17.

[11] D. Sangla, M. Castaing, F. Balembois, and P. Georges, "Highly efficient Nd:YVO_4 laser by direct in-band diode pumping at 914 nm," Opt. Lett. 34, 2159 (2009).

[12] H. Kogelnik and T. Li, “Laser beams and resonators”, Appl. Opt. 5(10), pp. 1550-1567 (1966).

[13] H. Zhao and A. Major, “Megawatt peak power level sub-100 fs Yb:KGW oscillators,” Optics Express Optics Express 22, 30425-30431 (2014).

[14] X. Ding, S. J. Yin, C. P. Shi, X. Li, B. Li, Q. Sheng, X. Y. Yu, W. Q. Wen, and J. Q. Yao, “High efficiency 1342 nm Nd:YVO_4 laser in-band pumped at 914 nm,” Opt. Express 19, 14315 (2011).

[15] H. Mirzaeian, S. Manjooran, and A. Major, “A simple technique for accurate characterization of thermal lens in solid state lasers,” Proc. SPIE 9288, 928802 (2014).

[16] Y. Sato and T. Taira, “Highly accurate interferometric evaluation of thermal expansion and dn/dT of optical materials,” Opt. Mater. Express 4, 876-888 (2014).

[17] F. Song, C. Zhang, X. Ding, J. Xu, G. Zhang, M. Leigh, and N. Peyghambarian, “Determination of thermal focal length and pumping radius in gain medium in laser-diode-pumped Nd:YVO_4 lasers,” Appl. Phys. Lett. 81, 2145 (2002)

[18] L. McDonagh, R. Knappe, A. Nebel, and R. Wallenstein, “Optimized Pumping of Nd:YVO_4 with Polarization-Insensitive Absorption for High Power Applications,” CLEO Technical Digest (CD) (Optical Society of America, 2005), paper CMS5.

[19] J. L. Blows, T. Omatsu, J. Dawes, H. Pask, and M. Tateda, “Heat Generation In Nd:YVO With and Without Laser Action,” IEEE Photon. Technol. Lett. 10, 1727 (1998).

Chapter 3

Discrete on-demand wavelength tuning of a diode-pumped $Nd:YVO_4$ laser at 1064, 1073, and 1085 nm

As was mentioned in Chapter 1, $Nd:YVO_4$ laser crystal provides many advantages such as high absorption and emission cross-sections which make it suitable for compact and efficient diode-pumping in medium range power applications. Now that the benefits of pumping at 914 nm in terms of thermal management were demonstrated, we turn to look at the available oscillation frequencies from the $Nd:YVO_4$ lasers.

According to the emission spectrum of a $Nd:YVO_4$ crystal shown in Fig. 1-3, apart from standard 1064 nm line from the $^4F_{3/2} \rightarrow {}^4F_{11/2}$ transition, laser generation at 1073 nm and 1085 nm from the adjacent Stark energy levels of the same manifold are also possible which, for example, can be used to generate other wavelengths through nonlinear frequency conversion [1,2]. Particularly, the transition lines at 1073, 1080, and 1084 nm have specific applications that cannot be provided by 1064 nm lasers. These wavelengths are used for optical pumping of superfluid helium and related scientific studies such as atomic and molecular spectroscopy [3-7]. Although the laser operations at 1080 and 1084 nm are not possible directly from $Nd:YVO_4$ the method described in this chapter can be directly applied to other sister material such as $Nd:GdVO_4$ which has stronger emission cross-section around 1070 and 1080 nm. Moreover, the emission cross-section of $Nd:YVO_4$ is also highly polarized, which guarantees the polarization of oscillation and allows for high efficiency in the further frequency conversion process. This is particularly beneficial since the frequency doubled output from the 1085 nm is around 543 nm, which corresponds to the excitation wavelength of the commonly used fluorophores [8].

There are multiple methods to manipulate the laser oscillation wavelengths and obtain higher round trip gain at other wavelengths than at 1064 nm. This can be done with various optical elements such as diffraction grating or specifically coated mirror [9-11]. Etalons are also normally used to achieve 1085 nm [12] output while 1073 nm laser operation is relatively more difficult to obtain due to its proximity to the 1064 nm line which has a much higher gain.

A stable Nd:YVO_4 laser operating at 1073 nm from a Nd:YVO_4 crystal was only recently reported by Pang et al. [13] with the use of a Type I phase-matching LiB_3O_5 crystal acting as a filter with maximum output power of 300 mW and the optical-to-optical efficiency of 7%. The 1085 nm operation has been reported in single and multi-wavelength operation together with 1064 nm [1,14-17]. Wavelength selectivity between these three laser operations, which is particularly attractive for agile wavelength extension of lasers, however, was not demonstrated. This chapter discuss the method used to obtain wavelength tuning among the closely separated Stark electronic levels. Further modification to obtain stable dual-wavelength or tri-wavelength will be discussed in the next chapter.

3.1 Wavelength selection

Suppression of 1064 nm can also be done using birefringent filter (BRF) where transmission window can be used to control the net round trip gain of adjacent emission lines by introducing wavelength dependent intracavity loss. The following explanation will describe the wavelength suppression ability of the BRF filter inserted into the laser cavity.

In order to have one laser wavelength oscillating and not the others, we need to look at the threshold condition of a diode-pumped solid-state laser system as described in [18]. The threshold power (P_{th}) for a 4-level laser system can be described as

$$P_{th,i} = \frac{L_{\lambda_i} - \ln\left(1 - T_{oc,i}\right)}{2\eta_i} \frac{hv_i}{\sigma_i \tau_i} \frac{1}{\eta_m} \frac{\pi\left(w_i^2 + w_p^2\right)}{2}, \tag{3-1}$$

$$i = 1, 2, 3,$$

where i refers to each laser wavelength, L_i is the round trip intracavity loss, T_{oc} is the transmission of the output coupler, hv_p is the pump photon energy, l is the length of the crystal η_i is the quantum defect efficiency, σ_i is the emission cross-section at the laser wavelength, τ is the upper state lifetime of the upper level, η_m is the mode-matching quality between pump beam and resonator modes as defined in the equation (2-19), w_i and w_p are the beam radii of the resonator mode and the pump beam, respectively.

Comparison between the two threshold powers at two competing wavelengths for oscillation can be made while considering the condition in the experiment where the same cavity was used for selectable multi-wavelength lasers. In this particular case, $T_{oc,\lambda_1} = T_{oc,\lambda_2} = T_{oc}$, $\tau_{\lambda_1} = \tau_{\lambda_2}$, $w_{\lambda_1} = w_{\lambda_2}$, and $\eta_{1064} = 85.9\%$, $\eta_{1073} = 85.18\%$, $\eta_{\lambda_{1085}} = 84.23\%$.

In order for λ_1 to oscillate instead of λ_2, $P_{th,\lambda_2} > P_{th,\lambda_1}$ or

$$\frac{L_{\lambda_2} - \ln\left(1 - T_{oc}\right)}{\sigma_{\lambda_2}\eta_{\lambda_2}} > \frac{L_{\lambda_1} - \ln\left(1 - T_{oc}\right)}{\sigma_{\lambda_1}\eta_{\lambda_1}} \quad . \tag{3-2}$$

In the case of BRF tuning

$$L_{\lambda_i} = L_{in} + L_{BRF} \tag{3-3}$$

where L_{in} is the round trip intracavity loss without BRF filter and L_{BRF} is the loss introduced by the BRF.

3.2 Intracavity Birefringent filter (BRF)

Birefringent crystal such as the one shown in Fig. 3-1 introduces phase retardation between the ordinary ray (o-ray) travelling with polarization perpendicular to its optical axis and the extraordinary ray (e-ray) travelling with polarization in the direction of the optical axis.

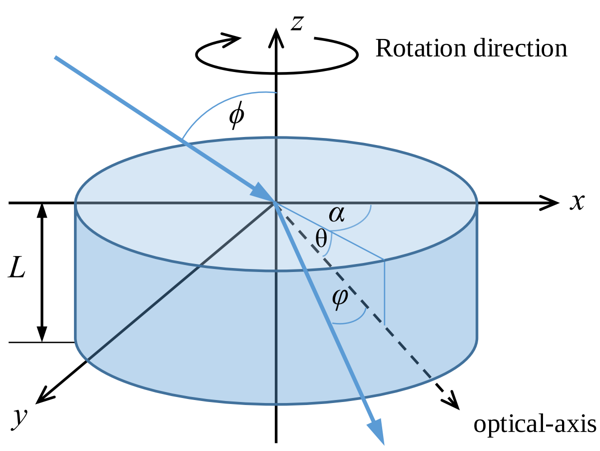

Fig. 3-1 A drawing of the birefringent plate, angles, and the corresponding notations.

This phase retardation is represented as the two distinct values of refractive indices n_e and n_o, and results in polarization rotation of the incident ray which can be represented as [19]

$$\Delta\delta = \sin^2\varphi\left(\frac{2\pi}{\lambda}\frac{\Delta nd}{\cos\phi}\right), \tag{3-4}$$

where $\Delta\delta$ is the phase retardation between the o-ray and e-ray, φ is the angle between the refracted ray traveling inside the birefringent plate and the optical axis, λ is the central wavelength of the laser, $\Delta n = n_e - n_o$, ϕ is the incident angle, and d is the thickness of the birefringent plate. Therefore, for a *p*-polarized ray with a fixed incident angle equal to Brewster's angle, a birefringent plate will exhibit maximum transmission for a set of wavelengths described by

$$\lambda = \frac{\Delta nd\sin^2\varphi}{m\sin\phi}, \tag{3-5}$$

where m is an integer, while other wavelengths that do not satisfy the condition above will experience polarization rotation and partial loss due to Fresnel reflection at both surfaces of the birefringent plate [20]. From the relation above, the set of wavelengths experiencing minimum loss can be selected by changing the thickness of the birefringent plate itself or changing the angle φ (through changing the angle α by rotating the BRF plate).

While the wavelengths that experience transmission peaks can be easy determined by the equation (3-5) above, which is similar to the case of BRF plates between the polarizers placed outside the laser cavity as seen in [21], the complete information on transmission must be calculated by Jones calculus which requires matrix formulation representing polarization changes through each surfaces of the optical elements are needed. The calculation method was thoroughly described by K. Naganuma et al. [22] and the detailed formulation of the Jones matrix method used in this calculation is given in Appendix B.

The calculated transmission through an intracavity 0.5-mm-thick and 4-mm-thick plates versus rotation angle (α) is shown in Fig. 3-2.

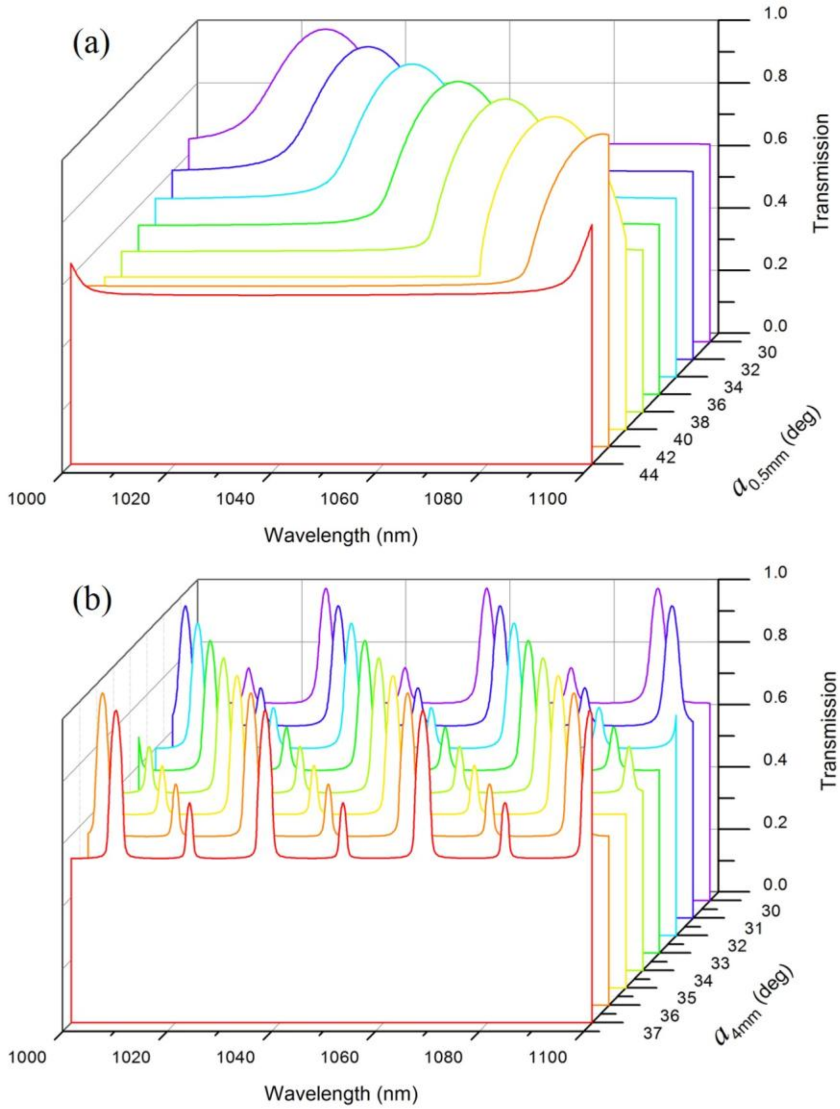

Fig. 3-2 Transmission of (a) 0.5-mm-thick (b) 4-mm-thick BRF plates versus rotation angle (α).

Since the emission spectrum of Nd:YVO_4 for π-polarization consists of discrete sharp and well separated emission lines unlike gain medium with broad emission spectrum such as Yb-doped lasers, it is more important to see the changes in transmission versus rotational angle only at the wavelengths of interest. This change is presented in Fig. 3-3. It can be seen that the high transmission bands are much broader versus the rotational angle for the 0.5-mm-thick BRF plate than for the 4-mm-thick plate. This leads to the overlapping of the 1064 nm transmission band with others which is undesirable for wavelength tuning. There are also fewer high transmission peaks for all wavelengths in 0.5-mm-thick plate case.

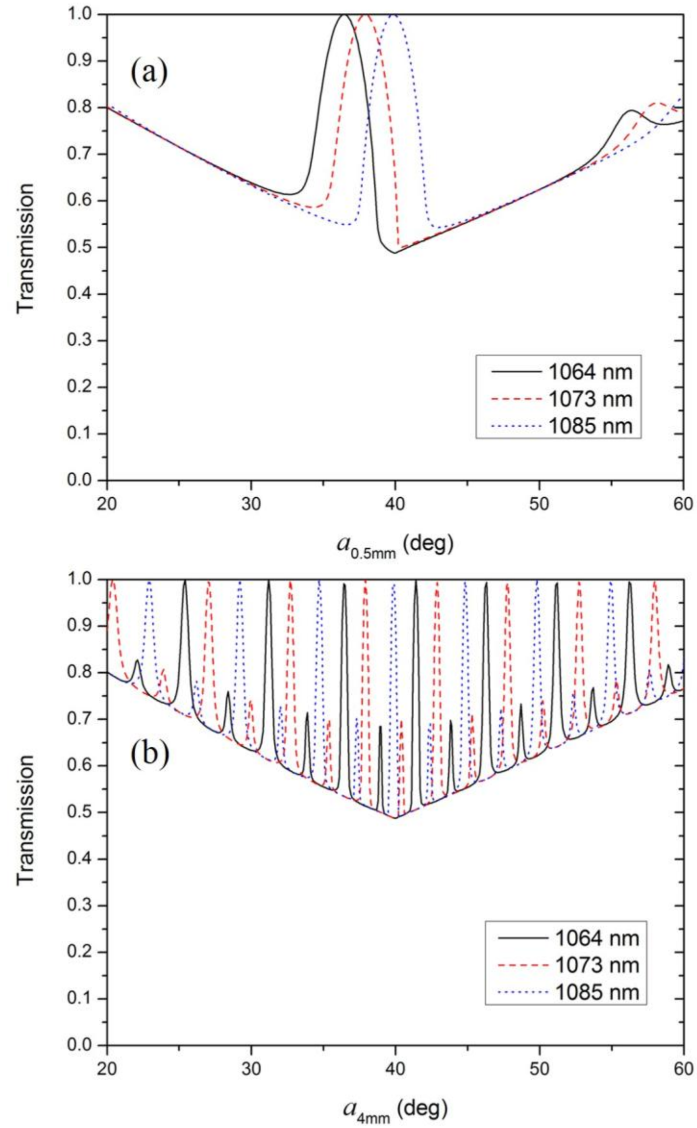

Fig. 3-3 Transmission for each emission wavelength versus α for (a) 0.5-mm-thick (b) 4-mm-thick plate.

From equation (3-2), to allow a successful oscillation at 1073 nm the following condition must be met:

$$\frac{L_{1064}-\ln\left(1-T_{oc}\right)}{\sigma_{1064}\eta_{1064}}>\frac{L_{1073}-\ln\left(1-T_{oc}\right)}{\sigma_{1073}\eta_{1073}}<\frac{L_{1085}-\ln\left(1-T_{oc}\right)}{\sigma_{1085}\eta_{1085}}. \quad (3\text{-}6)$$

As can be seen in the equation above, there is also a competition between 1073 nm and 1085 nm lines. However, due to their similar emission cross-sections, a small difference in transmission is enough to fully suppress one or the other. Therefore, further discussion will only state the requirement for successful suppression of the much stronger 1064 nm emission line.

Assuming that L_{in} is approximately 3% based on preliminary experiments without BRF and T_{oc} = 2.1% the relationship between the condition for lasing wavelength 1064 nm and 1073 nm becomes,

$$L_{BRF_{1064}} > 8.44 L_{BRF_{1073}} + 0.253 \tag{3-7}$$

In Fig. 3-4, let's consider only one pair of wavelengths competing for threshold condition. The greyed out areas under required transmission at 1064 nm line in both plots are all the possible values for transmission at 1064 nm which will result in successful suppression of the much easier to initiate 1064 nm laser operation and allows the competing gain (1073 nm line in this case) to dominate the process.

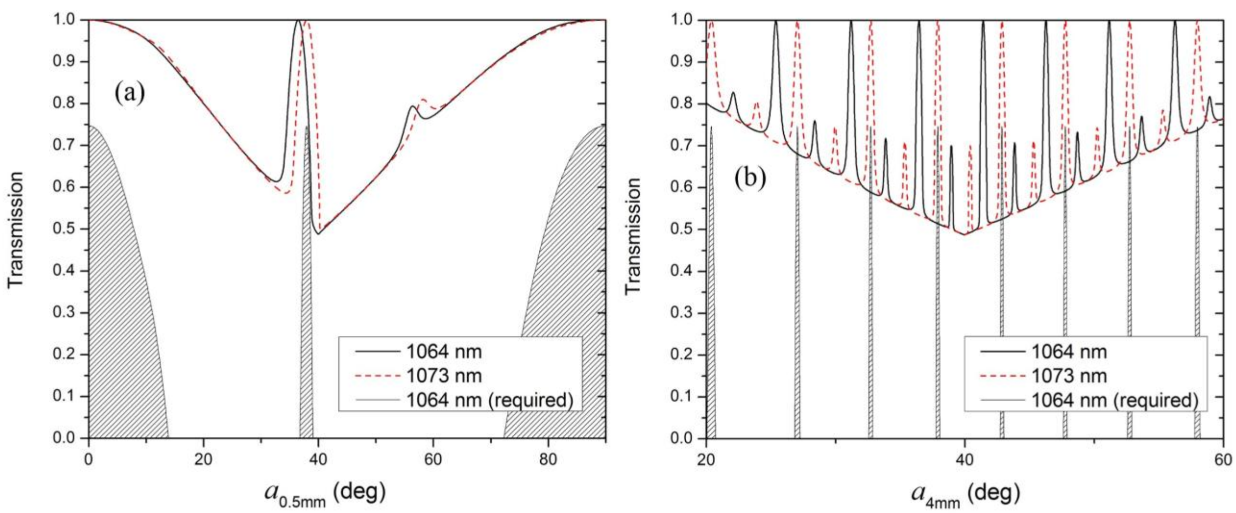

Fig. 3-4 shows that the BRF plate with 0.5 mm thickness cannot successfully suppress the 1064 nm oscillation while 4 mm-thick plate can at several angles.

Fig. 3-4 (a) shows that the BRF plate with 0.5 mm thickness cannot successfully suppress the 1064 nm oscillation while the 4-mm-thick plate can do it at several angles. It is also worth noting that, at the point where the transmission line (solid black) briefly crosses into the greyed out area in Fig. 3-4(b), the oscillation can enter the equilibrium between the two oscillating wavelengths and result in dual-wavelength operation. However, due to the sensitivity of this setup to the minute changes in the angle of rotation it is difficult to maintain such a regime over a long period of time. The dual-wavelength operation will be discussed in more detail in the next chapter.

3.3 Discrete tuning results and discussion

For our particular case, a quartz birefringent plate cut at its normal axis was used and the angle α can be changed by rotating the birefringent plate around its surface normal. We utilized this BRF in order to suppress the large gain at 1064 nm. This chapter reports a laser operation at 1064 nm, 1073 nm, and 1085 nm with discrete wavelength selectivity using a single birefringent plate which allows to select "on demand" any of these three wavelengths. This allows for a simpler cavity configuration and more economically feasible design than other methods involving specifically designed grating or mirror coating.

A 20-mm-long a-cut 1.5% doped Nd:YVO_4 was used in a 5-mirror cavity as shown in the schematic diagram in Fig. 3-5. The crystal aperture was 3x3 mm^2 and it was pumped by a fiber-coupled diode laser with a fiber core diameter of 110 μm and a numerical aperture of 0.12. The maximum pump power in the experiment was limited to 16.7 W. The pump was then coupled into the crystal with a set of achromatic doublets with 50 mm and 200 mm focal lengths. The spot size of the pump beam at the center of the gain medium was 275 μm.

The crystal was wrapped in an indium foil and cooled on the top and bottom surfaces in a copper holder kept at 16 °C. The gain medium was in-band pumped at 914 nm to reduce the thermal effects and increase the stability of the laser system [23]. Both surfaces of the Nd:YVO_4 crystal were anti-reflection coated (R < 0.5%) at 914 and 1064 nm. M_3 was a dichroic mirror with high reflection at 1064 nm (T_{DM} > 99.9%). A 4-mm-thick birefringent filter plate was inserted into the cavity before the output coupler at Brewster's angle to achieve the discrete wavelength tuning.

Output couplers (OC) with 1.6, 2.1, 5, 10, 15% transmission in the 1040-1090 nm range were used in the experiment in order to obtain the highest output power and optical efficiency for all three output wavelengths under the chosen pumping configuration.

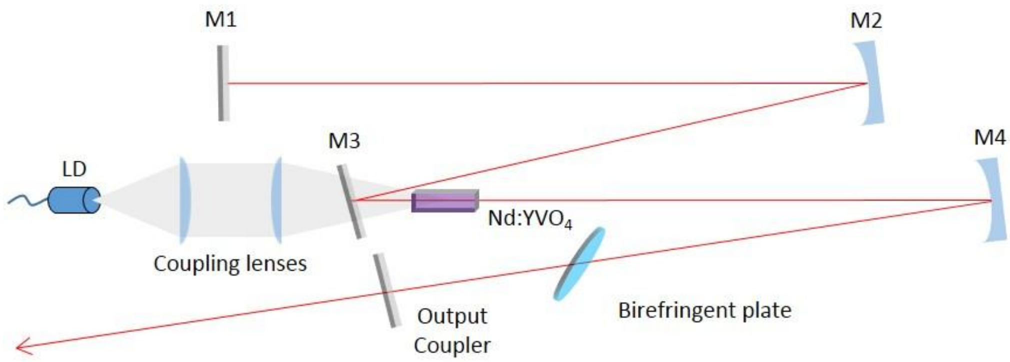

Fig. 3-5. Experimental setup for discrete tuning Nd:YVO_4 laser operation.

Three discrete CW laser operations around 1064 nm, 1073 nm, and 1085 nm were achieved by rotating the birefringent plate. Several birefringent plates that were available with 0.5, 1, and 2 mm thicknesses were tested with no tunability observed. A comparison between the maximum output powers obtained for different output couplers is shown in Fig. 3-6(a). The large disparity between the three wavelengths comes from the fact that both the threshold power and the maximum output power levels are affected by the much lower stimulated emission cross-sections at the output wavelengths of 1073 nm and 1085 nm as was shown in Fig. 1(a). As reported by Y. Sato et al., the emission cross-sections were 13.4×10^{-19} cm^2 for 1064 nm, 1.6×10^{-19} cm^2 for 1073 nm, and 1.7×10^{-19} cm^2 for 1085 nm [24]. Furthermore, the crystal anti-reflection coating was optimized for the 1064 nm. In our particular case, we chose to optimize the output power and the optical-to-optical efficiency at both 1073 and 1086 nm wavelengths.

The highest output powers obtained with a single (2.1%) output coupler at 1064 nm, 1073 nm, and 1085 nm were 4.78 W, 3.89 W, and 3.92 W, respectively. The output power levels from each laser line are shown in Fig. 3-6 (b). The output powers were measured as a function of the absorbed pump power at 914 nm. At the highest level of pump power, the slope and optical-to-optical efficiencies were 49.8% and 43.3% at the 1064 nm output, 46.5% and 35.2% at the 1073 nm output, and 45.7% and 35.5% at the 1085 nm output. The beam quality factors (M^2) were lower than 1.43 throughout the experiment for any of the three wavelengths and were shown to be TEM_{00} as seen in the inset of Fig. 3-6 (b).

(a)

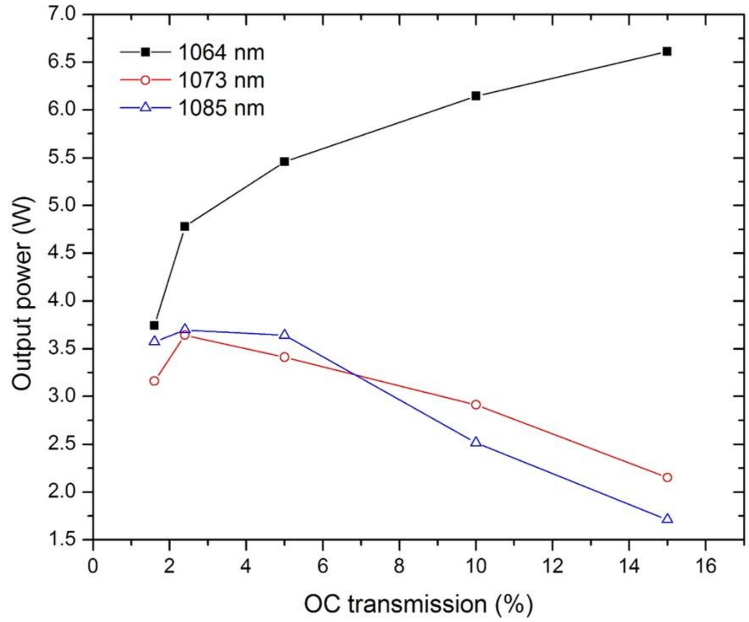

(b)

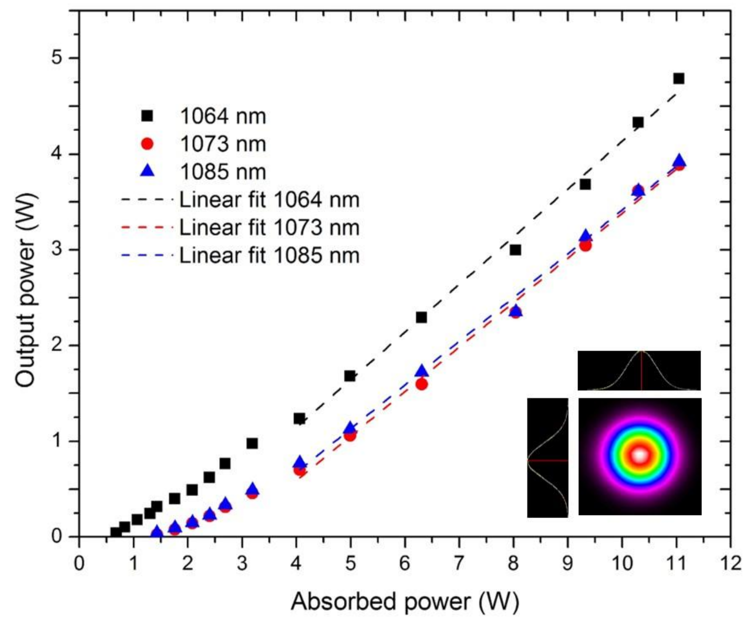

Fig. 3-6. (a) Maximum output power obtained with different output couplers (OC). (b) Output power for three different output wavelengths, 1064, 1073, and 1085 nm and 2.1% OC.

The three laser output spectra are shown in Fig. 3-7. The peaks of the laser output spectra are at 1064.02 nm, 1073.05 nm, and 1085.25 nm with linewidths of about 0.07 nm and are limited by the resolution of the available optical spectrum analyzer. Wavelength tunability around the 1085 nm wavelength from 1084.5 to 1086.1 nm was also observed.

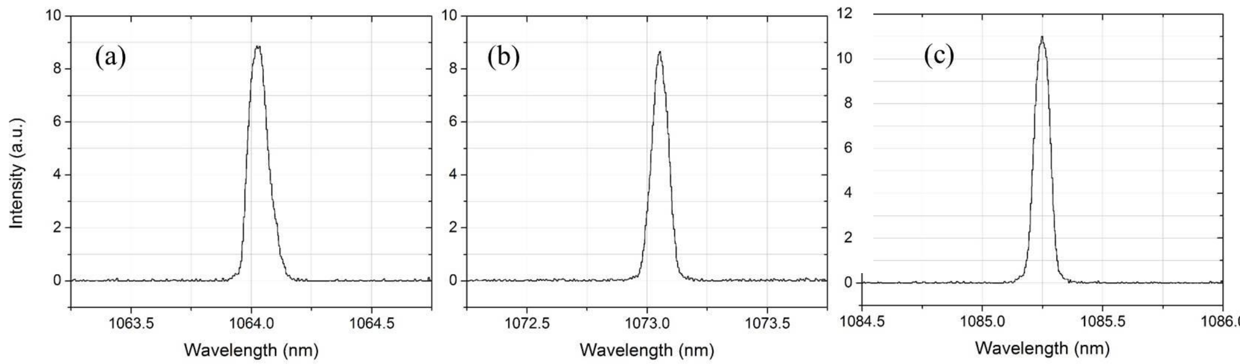

Fig. 3-7. Laser spectra at (a) 1064 nm, (b) 1073 nm, and (c) 1085 nm.

3.4 Conclusion

In summary, to the best of our knowledge, the discrete tuning of the $Nd:YVO_4$ laser operating at three wavelengths, 1064.0 nm, 1073.1 nm, and 1085.2 nm was demonstrated for the first time and with the highest slope and optical-to-optical efficiencies. Using a 5-mirror laser cavity, a 4-mm-thick birefringent filter plate, and the 914 nm pumping, the output powers of more than of 3.8 W at 11.2 W of absorbed pump power, slope efficiencies of more than 40%, and optical to optical efficiencies of more than 35% for any of the three wavelengths were achieved.

Such multi-wavelength operating regime can lead to discretely tunable multi-wavelength visible laser sources via nonlinear frequency conversion. A comparison with other results is given in table 3-1.

Table 3-1 Other notable results from 1073 and 1085 nm lines

Crystal	Wavelength	Output power (W)	Slope efficiency (%)	Opt-to-opt efficiency (%)	Reference
$Nd:YVO_4$	1073.2	0.3	-	7	Q. S. Pang [13]
Nd:YAP	1073	5.2	35.8	33.5	Y. S. Tzeng [25]
	1084	0.57	-	12	
$Nd:LuVO_4$	1089.5	3.6	35	30	Y. P. Huang [26]

Nd:$GdVO_4$	1083	3.4	30	28	Y. F. Chen [15]
Nd:$GdVO_4$	1083	10.1	37	31	L. Chen [27]
Nd:YVO_4	1064.1	**4.78**	**49.8**	**43.3**	This work
	1073.1	**3.89**	**46.5**	**35.2**	
	1085.3	**3.92**	**45.7**	**35.5**	

References

[1] G. Shayeganrad and L. Mashhadi, "Dual-wavelength CW diode-end-pumped a-cut Nd:YVO_4 laser at 1064.5 and 1085.5 nm," Appl. Phys. B 111, 189–194 (2013).

[2] A. J. Lee, D. J. Spence, J. A. Piper, and H. M. Pask, "A wavelength-versatile, continuous-wave, self-Raman solid-state laser operating in the visible," Opt. Express 18, 20013-20018 (2010).

[3] L. D. Schearer and P. Tin, "Tunable lasers at 1080 nm for helium optical pumping," J. Appl. Phys. 68(3), 943– 949 (1990).

[4] E. F. Stephens, R. Vandiver, P. Tin, and M. R. Kokta, "Continuous-wave operation and tuning characteristics of Nd:$LuAlO_3$ at 1083 nm for 3 He and 4 He optical pumping," J. Appl. Phys. 78(5), 3543–3545 (1995).

[5] P. C. Pastor, G. Giusfredi, P. De Natale, G. Hagel, C. De Mauro, and M. Inguscio, "Absolute frequency measurements of the 23 S1→23 P 0,1,2 atomic helium transitions around 1083 nm," Phys. Rev. Lett. 92(2), 023001 (2004).

[6] W. G. Rellergert, S. B. Cahn, A. Garvan, J. C. Hanson, W. H. Lippincott, J. A. Nikkel, and D. N. McKinsey, "Detection and imaging of He2 molecules in superfluid helium," Phys. Rev. Lett. 100(2), 025301 (2008).

[7] W. Guo, J. D. Wright, S. B. Cahn, J. A. Nikkel, and D. N. McKinsey, "Metastable helium molecules as tracers in superfluid liquid ^4He," Phys. Rev. Lett. 102, 235301 (2009).

[8] C. Dongre, J. V. Weerd, N. Bellini, R. Osellame, G. Cerullo, R. V. Weeghel, H. J. W. M. Hoekstra, and M. Pollnau, “Dual-Point Dual-Wavelength Fluorescence Monitoring of DNA Separation in a Lab on a Chip,” Biomed. Opt. Express 1(2), 729-735 (2010).

[9] M. Hemmer, Y. Joly, L. Glebov, M. Bass, M. Richardson, “Volume Bragg Grating assisted broadband tunability and spectral narrowing of Ti: sapphire oscillators,” Opt. Express 17, 8212–8219 (2009)

[10] H. Y. Shen, R.R. Zeng, Y.P. Zhou, G.F. Yu, C.H. Huang, Z.D. Zeng, W.J. Zhang, Q.J. Ye, “Simultaneous multiple wavelength laser action in various neodymium host crystals,” IEEE J. Quantum Electron. 27, 2315–2319 (1991)

[11] S. Zhuang, D. Li, X. Xu, Z. Wang, H. Yu, J. Xu, L. Chen, Y. Zhao, L. Guo, X. Xu, “Continuous-wave and actively Q-switched Nd:LSO crystal lasers,” Appl. Phys. B 107, 41–45 (2011).

[12] C. Y. Li, Y. Bo, J.L. Xu, C.Y. Tian, Q.J. Peng, D.F. Cui, Z.Y. Xu, “Simultaneous dual-wavelength oscillation at 1116 and 1123 nm of Nd:YAG laser,” Opt. Commun. 284, 4574–4576 (2011)

[13] Q. S. Pang, J. Fu, L. Chang, M. Chen, Y. Liu, L. Z. Xu, Z. A. Bai, W. R. Guo, and G. Li, “1073 nm continuous-wave Nd:YVO_4 laser with Type I phase-matching LiB_3O_5,” Opt. Lett. 36, 1266-1268 (2011).

[14] G. Shayeganrad, Y.-C. Huang, L. Mashhadi, “Tunable single and multiwavelength continuous-wave c-cut Nd:YVO_4 laser,” Appl. Phys. B 108(1), 67-72 (2012).

[15] Y. F. Chen, M. L. Ku, and K. W. Su, "High-power efficient tunable Nd:$GdVO_4$ laser at 1083 nm," Opt. Lett. 30, 2107-2109 (2005).

[16] Xiao-Zhong Wang et al., “A 1064 nm, 1085 nm Dual-Wavelength Nd:YVO_4 Laser Using Fabry–Perot Filters as Output Couplers,” in IEEE Photonics Technology Letters 26(19), 1983-1985 (2014).

[17] Y. Lü, J. Xia, H. Liu, and X. Pu, “Simultaneous triple 914 nm, 1084 nm, and 1086 nm operation of a diode-pumped Nd:YVO_4 laser” J. Appl. Phys. 116, 163107 (2014).

[18] T. Y. Fan and R. L. Byer, “Diode laser-pumped solid-state lasers,” IEEE J. Quantum Electron. 24, 895–912 (1988).

[19] S. Zhu, “Birefringent filter with tilted optic axis for tuning dye lasers: theory and design,” Appl. Opt. 29, 410–415 (1990).

[20] A. L. Bloom, “Modes of a laser resonator containing tilted birefringent plates”, J. Opt. Soc. Am. 64 (4), 447 (1974).

[21] C. G. Trevino-Palacios, O. J. Zapata-Nava, E. V. Mejia-Uriarte, N. Qureshi, G. Paz-Martinez, O. Kolokolstev, “Dual wavelength continuous wave laser using a birefringent filter,” J. European Opt. Soc. 8, 13021 (2013).

[22] K. Naganuma, G. Lenz, and E. P. Ippen, “Variable bandwidth birefringent filter for stable femtosecond lasers,” IEEE J. Quantum Electron. 28(10), 2142-2150 (1992).

[23] X. Delen, F. Balembois, O. Musset, and P. Georges, “Characteristics of laser operation at 1064 nm in Nd:YVO_4 under diode pumping at 808 and 914 nm,” J. Opt. Soc. Am. B 28, 52-57 (2011).

[24] Y. Sato and T. Taira, “Spectroscopic properties of neodymium-doped yttrium orthovanadate single crystals with high-resolution measurement,” Jpn. J. Appl. Phys. 41(10), 5999-6002 (2002).

[25] Y. S. Tzeng, Y. J. Huang, C. Y. Tang, K. W. Su, W. D. Chen, G. Zhang, and Y. F. Chen, “High-power tunable single- and multiwavelength diode-pumped Nd:YAP laser in the $^4F_{3/2} \rightarrow {}^4I_{11/2}$ transition,” Opt. Express 21, 26261–8 (2013).

[26] Y. P. Huang, C. Y. Cho, Y. J. Huang, and Y. F. Chen, “Orthogonally polarized dual-wavelength Nd:$LuVO_4$ laser at 1086 nm and 1089 nm,” Opt. Express 20, 2107-2109 (2012).

[27] L. Chen, Z. Wang, H. Yu, S. Zhuang, S. Han, Y. Zhao, and X. Xu, “High-power single-and dual-wavelength Nd: $GdVO_4$ lasers with potential application for the treatment of telangiectasia,” Appl. Phys. Express 5(11), 112701 (2012).

Chapter 4

Dual-wavelength operations at 1064 & 1073 and 1064 & 1085 nm

Dual-wavelength lasers (lasers with two simultaneous outputs at different frequencies) have been a focus of several recent studies due to multiple promising applications in biomedicine such as blood analysis, DNA sequencing, flow cytometry, microscopy, and optogenetics [1-7].

Looking at the possible dual-wavelength operation regimes that the crystal of Nd:YVO_4 can offer based on the three emission lines discussed in Chapter 3, one can see that 1064 & 1073 nm and 1064 & 1085 nm wavelength pairs are possible. The latter pair can be used to generate 532 and 543 nm (when frequency-doubled) which are used in flow cytometry and generally come from two different laser systems, Nd:YAG and He-Ne lasers, with the power of He-Ne usually being the limiting factor (less than 2.0 mW).

These pairs can also be converted to 2.4 and 5.6 THz coherent radiation through proper difference frequency generation (DFG) such as the one demonstrated by M. Scheller et al. [8]. Such THz radiation has a promising potential for imaging, sensing, and spectroscopy applications [9-11]. Moreover, the 1073 nm emission line has not been reported in dual-wavelength operation even though its stimulated emission cross-section is comparable to the one at 1086 nm. This is possibly due to its proximity to the 1064 nm emission line. This chapter demonstrates the ability to achieve gain balancing (two or more laser oscillations with the same round trip gain and thus oscillating simultaneously) by using two intracavity birefringent plates.

4.1 Gain balancing

There are multiple methods to achieve dual-wavelength operation from laser gain media with sharp emission lines as seen in Nd-doped crystalline gain media. All of them try to achieve balanced gains at two or more wavelengths. Dual-wavelength generation in solid-state lasers can be separated into three main categories.

First method to obtain dual-wavelength operation is to have two crystals with similar emission cross-sections in order to have two comparable gains. This method can also be extended to incorporate hybrid laser gain medium [12] or gain medium with multiple dopants

[13]. Second method utilizes the fact that in some uniaxial or biaxial crystals, emission peaks for horizontal and vertical polarizations occur at different frequencies. Therefore, by choosing a proper direction, orthogonally-polarized laser operation can take place [14,15]. These first two approaches in obtaining a dual-wavelength operation rely on a very strict balance of round-trip gain which can be easily disturbed by cavity conditions such as thermal lensing or fluctuation in power. This can lead to poor control of power ratio between the two oscillating wavelengths.

The last type of dual-wavelength generation is achieved by inserting an extra loss element inside the laser cavity. This is generally done by using a specific coating of the output coupler to intentionally have higher reflectivity at wavelength with low emission cross-section and low reflectivity at wavelength with high emission cross-section [16-17]. However, specific coating on the OC also means that the dual-wavelength regime will again operate on a strict condition and will only work at a certain power level. To allow for more flexibility in the setup, tunable loss elements such as etalons, Fabry-Perot filters, or birefringent filters are better suited for dual-wavelength generation.

In order for two wavelengths to start oscillating at the same time, it is required that the threshold power for both wavelengths, e.g. 1064 and 1073 nm, was the same [13,18]. From equation (3-2) in the last chapter, the condition for the same threshold power for the two laser wavelength becomes,

$$\frac{L_{1064}-\ln\left(1-T_{oc}\right)}{\sigma_{1064}\eta_{1064}}=\frac{L_{1073}-\ln\left(1-T_{oc}\right)}{\sigma_{1073}\eta_{1073}}. \tag{4-1}$$

where *T* is the transmission of the OC. It is worth noting that equal threshold condition described by equation (4-1) does not automatically translate into the equal power ratio between the oscillating wavelengths *above* the threshold. Unlike other methods of dual-wavelength generation, the benefit of using BRF plates is that they enable not only to select the correct threshold condition via changes in the L_{1064} and L_{1073} losses (i.e. BRF introduced losses) but also to reach 50% power ratio at all power levels which is generally much more complicated [19].

Fig. 4-1 gives a closer look at the change in transmission at 1064 and 1073 nm induced by the 4-mm-thick BRF plate across 17 degrees of rotation angle (full range of angles was shown in Fig. 3-4(b) in Chapter 3) and T_{oc} = 2.1%. The condition described by equation (4-1) is possible at a certain angle of the BRF plate where the transmission at 1064 nm (black) is exactly equals to the required transmission (blue). As seen in Fig. 4-1, this condition was met when α_{4mm} is equal to 27.0°, 27.1°, 32.6°, and 32.8°.

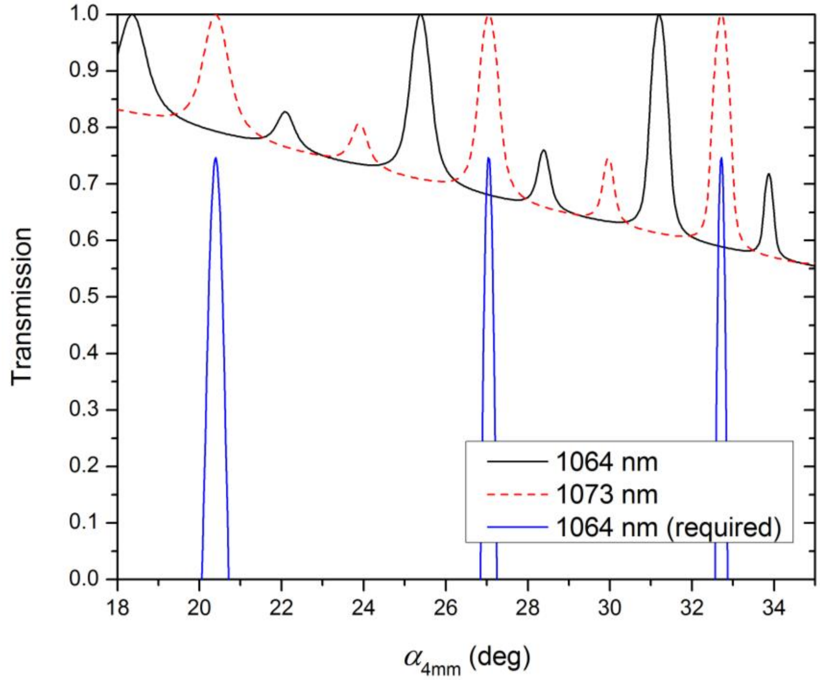

Fig. 4-1. (a) Transmission at 1064 and 1073 nm and the required transmission at 1064 nm for dual-wavelength operation using a 4-mm-thick BRF.

Although in all four cases above the two wavelengths (1064 and 1073 nm) will experience the same P_{th}, our first problem with using only the 4-mm-thick plate is that the angular tolerance for this condition is very small, making it hard to perfectly achieve in practice, and thus causing unstable power ratio of the generated wavelengths over a long period of time.

Furthermore, the same threshold condition as described in equation (4-1) does not take into account the gain competition above threshold, which is our second problem. To illustrate the problem of gain balancing at power levels at and beyond P_{th}, we recall that the laser output power (P_{out}) beyond the threshold power is described by

$$P_{out} = \frac{-\ln(1-T_{oc})}{-\ln(1-T_{oc})+L_{\lambda_i}} \frac{v_L}{v_p} \left(P_{abs} - P_{th,\lambda_i} \right), \quad (4\text{-}2)$$

$$i = 1, 2,$$

where λ_i refers to each laser wavelength, ν_L is the laser frequency, ν_p is the pump frequency, and P_{abs} is the absorbed pump power.

With this in mind, let us consider the starting case where there is *no* intracavity BRF plate in the laser cavity. The intracavity losses are the same at both wavelengths in this case (let's say, $L_{1064} = L_{1073}$) whereas $P_{th,1064} < P_{th,1073}$ from equation (3-1) because of the difference between the emission cross-sections ($\sigma_{1064} > \sigma_{1073}$). This laser operation is drawn in Fig. 4-2(a). As P_{abs} increases, the output power (P_{out}) at 1064 nm also increases with the slope efficiency ($\eta_{s,1064}$) with *no* dual-wavelength operation.

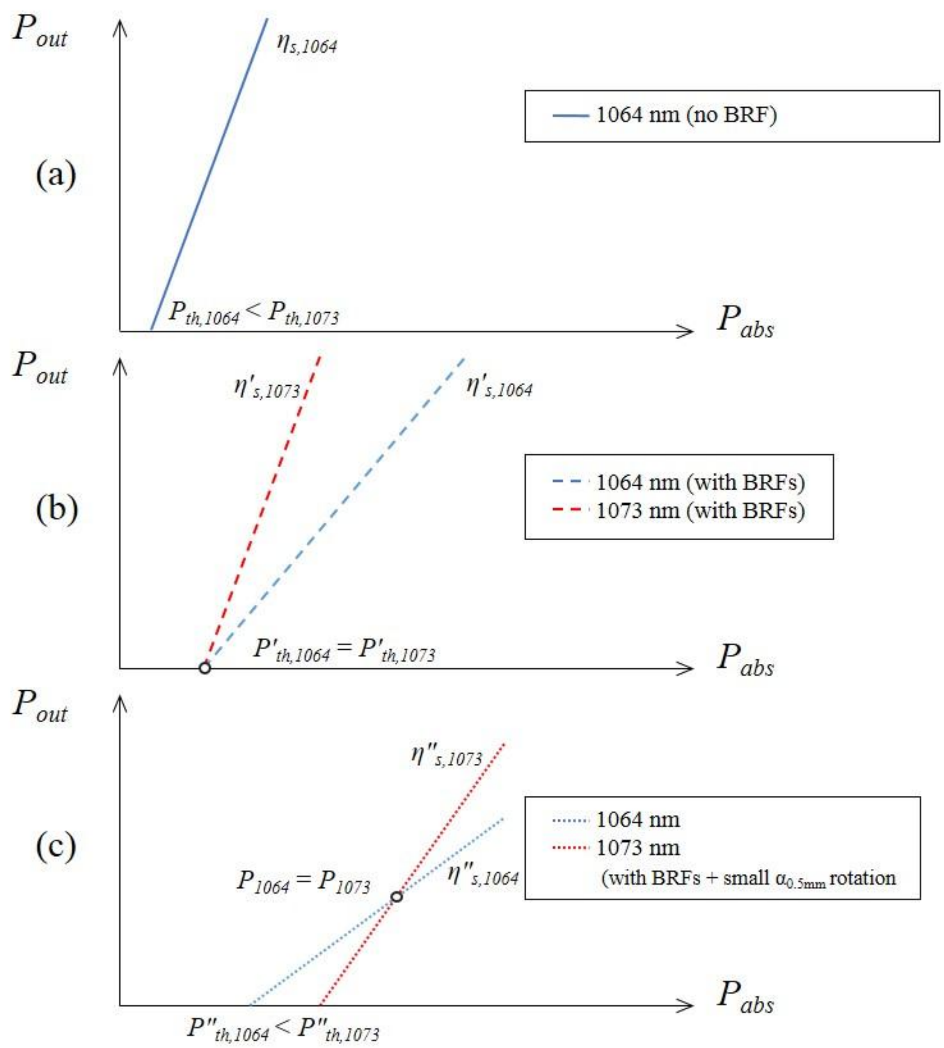

Fig. 4-2. Simple illustration of the change in output power versus absorbed power of single wavelength lasers for various conditions involving birefringent tuning.

The second case (Fig. 4-2(b)) is where we introduced a 4-mm-thick BRF plate into the cavity which helps fulfill the exact condition described by equation (4-1) (α_{4mm} = 27.0°, where $L_{BRF,1064}$ = 0.32, $L_{BRF,1073}$ = 0, for example) which has $P_{abs} = P'_{th,1064} = P'_{th,1073}$. This point is shown as the starting point (white circle) in Fig. 4-2(b). Equation (4-2) shows, however, that the higher loss introduced at 1064 nm (high $L_{BRF,1064}$ and, ultimately, high L_{1064}) in order to achieve the same threshold pump power will result in the lower slope efficiency ($\eta'_{s,1064}$) than at 1073 nm ($\eta'_{s,1073}$). Therefore, at $P_{abs} > P'_{th,1064} = P'_{th,1073}$, the levels of P_{out} at the two wavelengths will start to diverge. As shown by the two lines in Fig. 4-2(b), this means that the dual-wavelength operation with equal power ratio for the oscillating wavelengths can only be achieved at a certain level of P_{abs} which describes our second problem mentioned above.

In order to solve the first problem (i.e. increase angular tolerance of the starting condition) and to solve the second problem (i.e. maintain the equal power dual-wavelength operation far above the threshold power ($P_{out,1064} = P_{out,1073}$ at $P_{abs} \gg P_{th}$)), we can use an *extra* loss element with lower angular sensitivity ($dL_{BRF}/d\alpha$), which can be found in thin BRF plates. The effect of having two BRFs in the cavity is shown in Fig 4-2(c). As can be seen, the introduced extra loss reduces the slopes and increases the thresholds for both wavelengths. Most importantly, it shifts the threshold of 1073 nm to a higher value of the absorbed pump power than that for 1064 nm. Therefore, by breaking the condition of equal thresholds, one can achieve equal power dual-wavelength oscillation well above the threshold. As a side effect, at each pump power level this regime would require a slightly different loss which can be conveniently found by rotation of a thin BRF. A 0.5-mm-thick quartz plate, which was the thinnest one available to us in the experiments, can be used in this case as the second BRF.

Consider again the transmissions at 1064 and 1073 nm wavelengths with the 4-mm-thick BRF plate kept at 27.0° rotation (α_{4mm} = 27.0°) as the starting point. At this point, $L_{BRF,1064}$ = 0.32, $L_{BRF,1073}$ = 0. We have established before and in Fig. 4-2(b) that these parameters will result in dual-wavelength operation only around the threshold power. From this point, a 0.5-mm-thick BRF plate is inserted into the cavity. Fig. 4-3(a) shows a transmission plot versus rotation angle of this newly inserted 0.5-mm-thick BRF plate. The overlapped sections (in red circles) of the 1064 nm transmission and the required transmission at 1064 nm represents $P_{th,1073} \approx P_{th,1064}$ and will have the largest angular tolerance when the slopes of both lines are at the minimum. As can be seen this occurs at 0° and 90° of rotation angles of the $\alpha_{0.5mm}$. Fine tuning of the starting condition can then be accomplished by rotation of $\alpha_{0.5mm}$ away from 0° and 90°. Therefore, two birefringent filters allow for more precise control over the conditions of the two oscillating wavelengths thus solving our first problem and allow for higher long term stability.

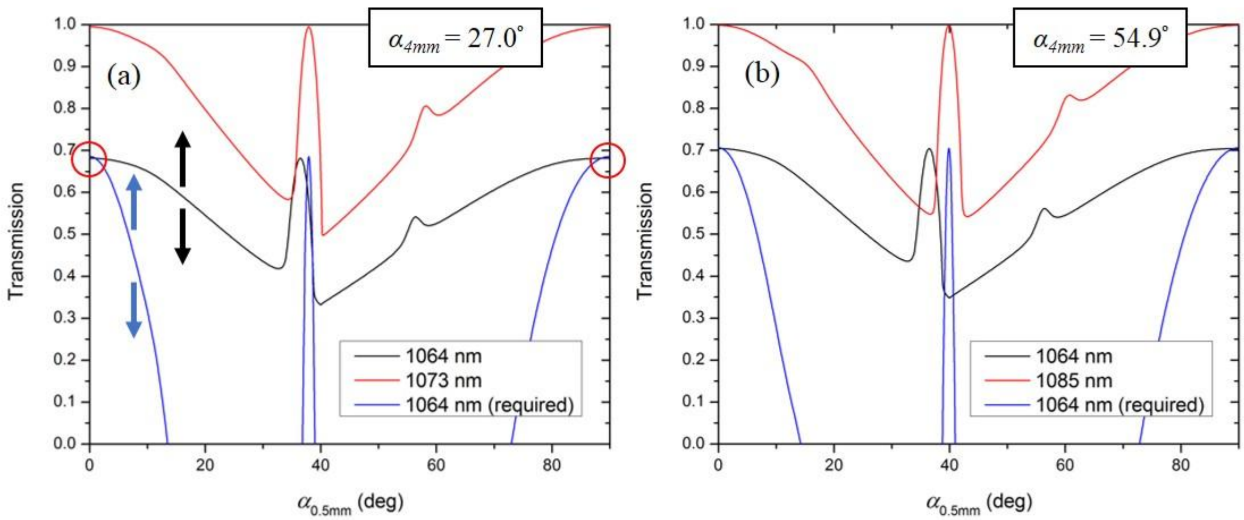

Fig. 4-3. Transmission through both 0.5-mm-thick and 4-mm-thick BRF plates: (a) transmission at 1064 and 1073 nm and the required transmission at 1064 nm for dual wavelength operation and (b) transmission at 1064 and 1085 nm and the required transmission at 1064 nm versus the rotation angle of the 0.5-mm-thick BRF plate. The fixed angles of the 4-mm-thick BRF plates are indicated in each graph.

The second problem of how to maintain the equal power ratio ($P_{out,1064} = P_{out,1073}$ at $P_{abs} \gg P_{th}$) can also be accomplished by the rotation of $\alpha_{0.5mm}$ away from 0° and 90° rotation angles. Qualitatively, since by rotating the 0.5-mm-thick BRF plate we are reducing transmission at both wavelengths simultaneously (i.e. increasing losses by $\Delta L_{BRF,1064} \approx \Delta L_{BRF,1073} \approx \Delta L_{BRF}$), equation (4-1) tells us that this causes $P''_{th,1073}$ to be higher than $P''_{th,1064}$ because the right side of equation (4-1) is much more sensitive to the change of intracavity loss which was previously kept at the minimum value. Equation (4-2) makes sure that the resulting slope $\eta''_{s,1064}$ after the rotation of $\alpha_{0.5mm}$ away from 0° and 90° (with $\Delta L_{BRF,1064} \approx \Delta L_{BRF,1073} \approx \Delta L_{BRF}$) is still lower than $\eta''_{s,1073}$ due to the larger total intracavity loss ($L_{1064} = L_{in} + L_{BRF,1064} + \Delta L_{BRF} > L_{1073} = L_{in} + L_{BRF,1064} + \Delta L_{BRF}$).

The two restrictions set by the equations (4-1) and (4-2) above mean that at *all* of the levels of P_{abs} beyond the starting point ($P_{abs} > P'_{th,1064} = P'_{th,1073}$), it would be always possible to find a $P_{out,1064} = P_{out,1073}$ situation since there will always be an intersection between the two output power lines as shown in Fig. 4-2(c). This can be ensured providing that the introduced ΔL_{BRF} intracavity loss by rotation of the thin BRF plate shifts the threshold condition away from the starting point. The effect of maintaining equal power ratio is illustrated in Fig. 4-2(c) where only one intersection was shown (white circle) indicating $P_{out,1064} = P_{out,1073}$. This also means that for a specific intracavity loss introduced by the two BRFs it would be possible to find the equal power dual-wavelength regime simply by adjusting the pump power level rather than the loss. Therefore, equal power regime can be stabilized either by the proper level of loss or pump power.

Therefore, two birefringent filters allow for more precise control over the initial conditions ($P'_{th,1064} = P'_{th,1073}$) of the two oscillating wavelengths thus allowing for higher long term stability as well as help in maintaining the equal power ratio at subsequent output power levels.

As a side note, the overlapping of the transmission at 1064 nm and the required transmission at the starting point as shown in Fig. 4-3(a) can be ensured by two factors.

First, by changing between different values of α_{4mm} (to other values besides 27.0°, for example) where transmission of 1073 nm is at maximum, the starting points of 1064 nm transmission can also be discretely selected (black arrows in Fig. 4-3(a)).

Secondly, it is worth noting that aside from changing the angle of α_{4mm}, the insertion angle can be purposefully chosen slightly off from the Brewster's angle, therefore increasing L_{in} and changing the level of the required transmission at 1064 nm (blue arrows). With these two factors chosen carefully, the starting points as seen in Fig. 4-3(a) can be achieved.

Finally, similar conditions can also be found in the case of dual-wavelength operation between the 1064 and 1085 nm as seen in Fig 4-3(b).

4.2 Dual-wavelength operation: experimental results and discussion

In the experiment, the 5 mirror-cavity as shown in Fig. 4-4 was used with cavity lengths adjusted to accommodate the extra insertion loss from the 2nd BRF. Two birefringent filter plates, 4 mm and 0.5 mm, were used at the Brewster's angle in the laser cavity. The 4-mm-thick birefringent filter plate was inserted into the cavity first and rotated until the 1073 nm laser output was observed. This birefringent plate ensured that the 1064 nm line fell into the low transmission band of the filter. The second plate with 0.5 mm thickness was then inserted and both plates were finely adjusted until both wavelengths were present and had the highest output power. Among multiple OCs available, the one with the 2.1% transmission in the 1040-1090 nm range was found to provide the highest output power in dual-wavelength operation.

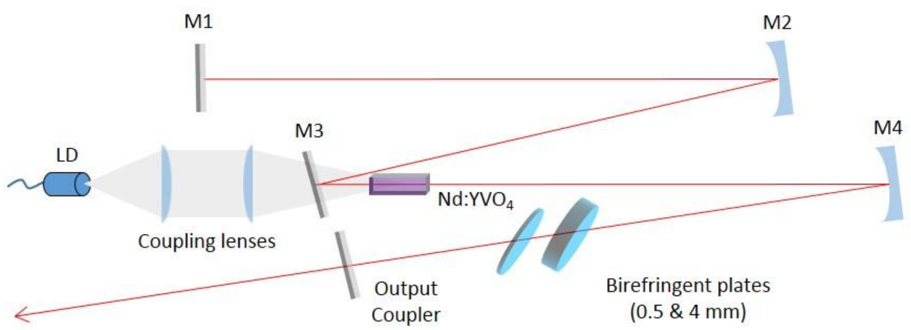

Fig. 4-4. Experimental setup for dual-wavelength operation of Nd:YVO_4.

Dual-wavelength oscillation was maintained within the range of 3-5 degrees of rotation of $\alpha_{0.5mm}$. At 11.2 W of absorbed pump power (16.7 W of incident pump power), the dual-wavelength operation was observed after carefully adjusting the two birefringent filters. The output power with 1:1 power ratio is plotted in Fig. 4-5.

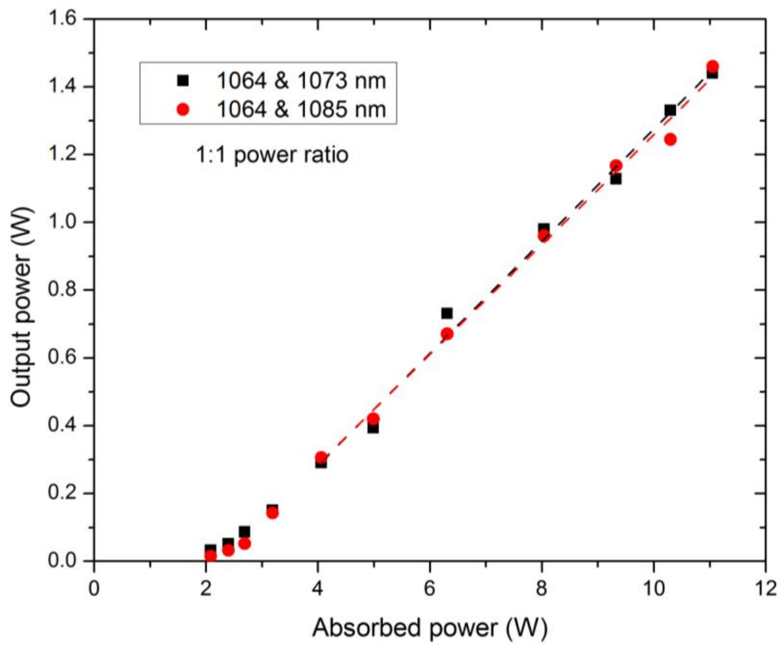

Fig. 4-5. Dual-wavelength output power at 1:1 power ratio versus absorbed power.

The maximum output power when each wavelength had a similar spectral intensity (1:1 power ratio) was 1.44 W in 1064 & 1073 nm operation. The slope efficiency was 16.53% in this case.

The same procedure was followed and 1.46 W of output power was obtained in 1064.1 & 1085.3 nm dual-wavelength operation with the slope efficiency of 16.2%. When the birefringent filter plate was rotated until the laser was operating at a single laser wavelength again, the output powers were increased to 4.61 W, 3.83 W and 3.74 W for 1064.1, 1073.1, and 1085.3 nm wavelengths, respectively. Fig. 4-6 and Fig. 4-7 show the output spectra for 1064.1 & 1073.1 nm and 1064.1 & 1085.3 nm operations, respectively. As expected, power ratio could be adjusted either by the BRFs or pump power level.

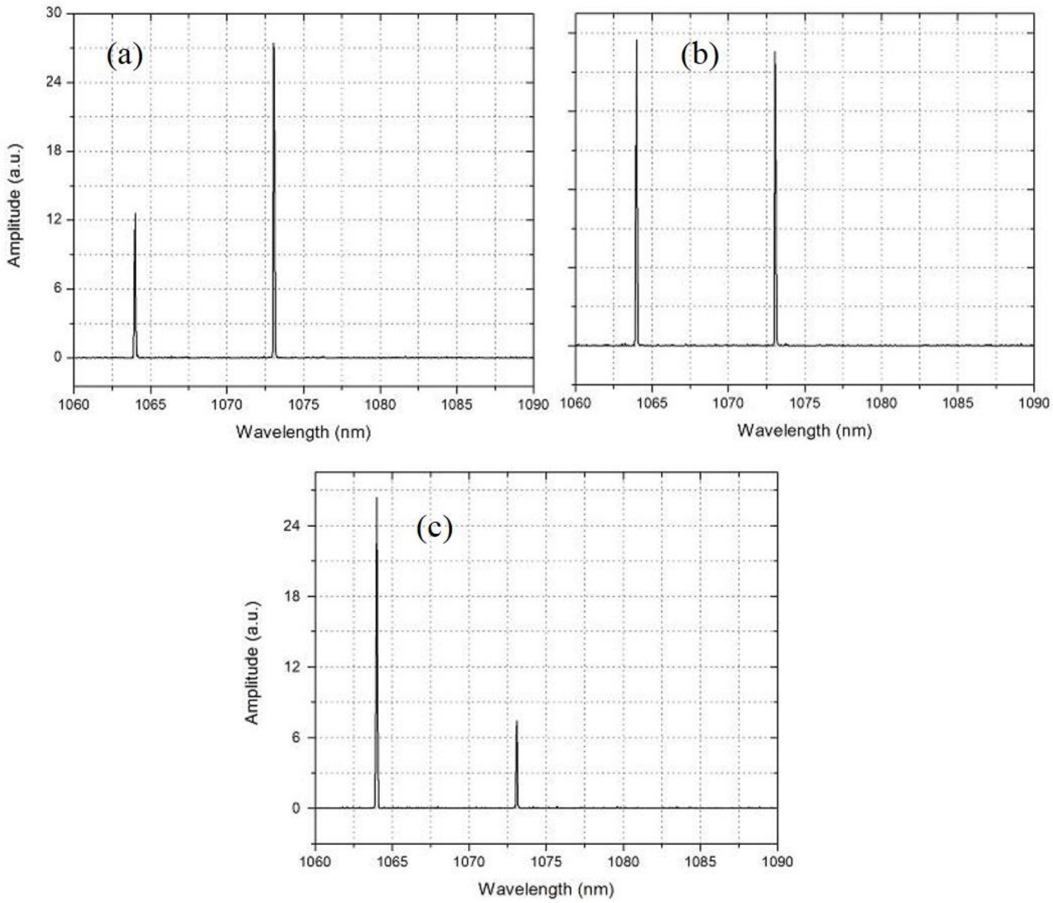

Fig. 4-6. Dual-wavelength operation spectra at 1064.1 and 1073.1 nm. (a), (b), and (c) show the change in power ratio between the two output wavelengths by adjusting the rotation angle of the 0.5-mm-thick BRF plate.

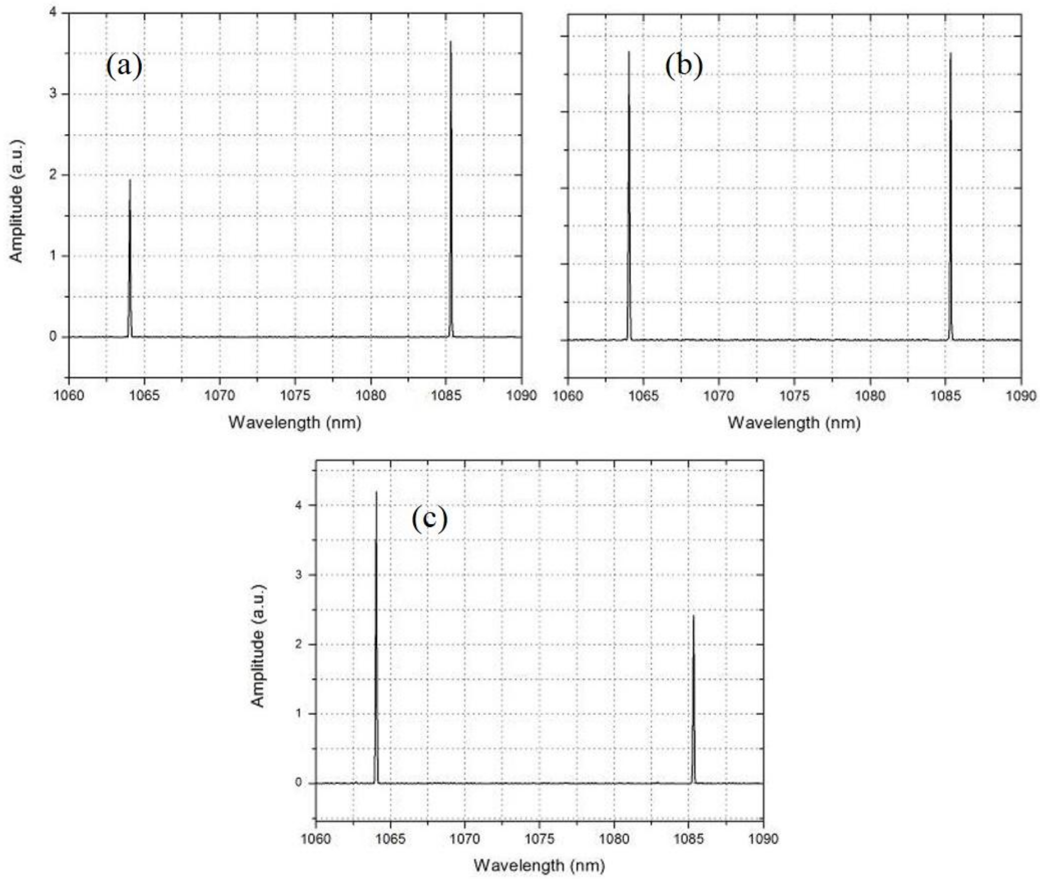

Fig. 4-7. Dual wavelength operation spectra at 1064.1 and 1085.3 nm. (a), (b), and (c) show the change in power ratio between the two output wavelengths by adjusting the rotation angle of the 0.5-mm-thick BRF plate.

Although the power ratio of the dual-wavelength output was still sensitive to the change in the pump power level of the system and specific power ratio could only be maintained within a limited range of output power without the change in cavity parameters, it could be adjusted back to 1:1 throughout all of the output power levels by rotating the 0.5-mm-thick birefringent plate. The long-term stability of the average laser output power at the highest power level was better than 1% over 2 hours with the fluctuation in the spectral power ratio of 2.14% obtained from the optical spectrum analyzer data (starting from 1:1 power ratio, the maximum deviation of intensity at 1073 nm over 1064 nm was recorded ($\Delta I_{1073} / I_{1064}$)). The linewidths of each wavelength were ~0.1 nm and were limited by the resolution of the available spectrometer.

4.3 Comparison with other dual-wavelength operations

To compare the results achieved in this work, the following table shows several notable results of dual-wavelength Nd-doped lasers.

Table 4-1. Notable results of dual-wavelength Nd-doped lasers

References	Crystal	Wavelength pair (nm)	Freq. difference (THz)	Method	Tunable power ratio	P_{out} (W) at 1:1 power ratio	Opt-to-opt efficiency at 1:1 power ratio
Y. P. Huang et al. [14]	$Nd:LuVO_4$	1086/1089	0.7	2 polarizations	No	0.74	17.5
F. Zhang et al. [16]	Nd:YAG	1064/1319	67.8	2 OCs	No	0.65	12.0
G. Shayeganrad et al. [20]	$Nd:YVO_4$	1066/1083, 1085,1088	5.6	Etalon	No	-	8
G. Shayeganrad et al. [6]	$Nd:YVO_4$	1064/1085	5.57	Specific OC coating	No	N/A	N/A
L. J. Chen et al. [16]	Nd:LYSO	1075/1079	1.06	Specific OC coating	No	0.7	27.7
C. Y. Li et al. [21]	Nd:YAG	1116/1123	1.86	Etalon	No		9.2
X. Wang et al. [22]	Nd:YAG	1064/1073	2.4	Fabry–Perot filter	Yes	0.581	10.9
X. Wang et al. [19]	$Nd:YVO_4$	1064/1085	5.6	Fabry–Perot filter	Yes	0.156	1.38
This work	$Nd:YVO_4$	1064/1073	2.39	2 BRFs	**Yes**	**1.44**	**13.0**
		1064/1085	5.62	2 BRFs	**Yes**	**1.46**	**13.2**

As can be seen from Table 4-1, our result is the first dual-wavelength operation with two wavelength pairs at 1064 & 1073 nm and 1064 & 1085 nm achieved with the same laser setup without the need to replace an optical element. The highest optical-to-optical efficiencies with controllable spectral power ratio was demonstrated for both wavelength pairs which is desirable for the generation of THz radiation. We have achieved the highest output power as well.

4.4 Conclusion

In conclusion, to the best of my knowledge, the results shown in this work were the first demonstration of the dual-wavelength 1064.1 & 1073.1 nm and 1064.1 & 1085.3 nm $Nd:YVO_4$ lasers with adjustable output power ratios and operating with high stability. The explanation on how multiple BRFs are required to achieve the power ratio tunable dual-wavelength laser was also given here. Both dual-wavelength pairs can be obtained with one setup with minor adjustments. The observed dual-wavelength output is very promising for applications in THz generation because the frequency difference corresponds to the desirable range of THz radiation (1-10 THz). The high output power and efficiency from this method could lead to a better source of THz radiation. Finally, it is worth mentioning that multiple BRF plates can also be used to generate a more complex transmission shape and ultimately to balance the gain for more than 1 pair of wavelengths at a time. This can lead to even tri-wavelength operation which is much harder to achieve with other tuning methods.

References

[1] J. Wang, Y. Wang, B. Li, D. Feng, J. Lu, Q. Luo, and P. Li, “Dual-wavelength laser speckle imaging to simultaneously access blood flow, blood volume, and oxygenation using a color CCD camera,” Opt. Lett. 38, 3690-3692 (2013).

[2] C. W. Pirnstill, B. H. Malik, V. C. Gresham, and G. L. Cote, “In Vivo Glucose Monitoring Using Dual-Wavelength Polarimetry to Overcome Corneal Birefringence in the Presence of Motion,” Diabetes Technology & Therapeutics 14(9), 819-827 (2012).

[3] H. M. Shapiro, *Practical Flow Cytometry* (4th Edition, Wiley-Liss, 2003).

[4] M. R. Jafarfard, S. Moon, B. Tayebi, and D. Y. Kim, “Dual-wavelength diffraction phase microscopy for simultaneous measurement of refractive index and thickness,” Opt. Lett. 39, 2908-2911 (2014).

[5] M. Prigge, F. Schneider, S. P. Tsunoda, C. Shilyansky, J. Wietek, K. Deisseroth, P. Hegemann, “Color-tuned channelrhodopsins for multiwavelength optogenetics,” J. Biol. Chem. 287(38), 31804-12 (2012).

[6] G. Shayeganrad and L. Mashhadi, “Dual-wavelength CW diode-end-pumped a-cut Nd:YVO_4 laser at 1064.5 and 1085.5 nm,” Appl. Phys. B 111, 189–194 (2013).

[7] P. Hering, J.P. Lay, and S. Stry, *Laser in environmental and life sciences: modern analytical method* (Springer, Heidelberg, Berlin, 2003).

[8] M. Scheller, J. M. Yarborough, J. V. Moloney, M. Fallahi, M. Koch, and S. W. Koch, “Room temperature continuous wave milliwatt terahertz source,” Opt. Express 18, 27112-27117 (2010).

[9] J. F. Federici, B. Schulkin, F. Huang, D. Gary, R. Barat, F. Oliveira, and D. Zimdars, “THz imaging and sensing for security applications—explosives, weapons and drugs,” Semicond. Sci. Technol. 20(7), S266–S280 (2005).

[10] J. B. Baxter and G. W. Guglietta, “Terahertz spectroscopy,” Anal. Chem. 83(12), 4342–4368 (2011).

[11] C. B. Reid, E. Pickwell-MacPherson, J. G. Laufer, A. P. Gibson, J. C. Hebden, and V. P. Wallace, “Accuracy and resolution of THz reflection spectroscopy for medical imaging,” Phys. Med. Biol. 55(16), 4825–4838 (2010).

[12] A. J. Singh, S. K. Sharma, P. K. Mukhopadhyay, S.M. Oak, “Dual wavelength operation in diode-end-pumped hybrid vanadate laser,” Pramana J. Phys. 75, 929 (2010).

[13] B. M. Walsh, “Dual wavelength lasers,” Laser Phys. 20: 622 (2010).

[14] Y. P. Huang, C. Y. Cho, Y. J. Huang, and Y. F. Chen, “Orthogonally polarized dual-wavelength Nd:$LuVO_4$ laser at 1086 nm and 1089 nm,” Opt. Express 20, 2107-2109 (2012).

[15] H. Zhao and A. Major, “Orthogonally polarized continuous wave dual-wavelength Yb:KGW laser induced by thermal lensing,” Appl. Phys. B. 122(6), 163 (2016).

[16] F. Zhang, M. Gaafar, C. Möller, W. Stolz, M. Koch and A. Rahimi-Iman, “A serially-connected two-chip VECSEL for dual-wavelength emission,” 2016 International Conference Laser Optics (LO), St. Petersburg, R3-18-R3-18(2016).

[17] L. Chen, X. Xu, Z. Wang, D. Li, H. Yu, J. Xu, S. Zhuang, L. Guo, Y. Zhao, and X. Xu, “Efficient dual-wavelength operation of Nd:LYSO laser by diode pumping aimed toward the absorption peak,” Chin. Opt. Lett. 9, 071403-071403 (2011).

[18] Chen, Y. “cw dual-wavelength operation of a diode-end-pumped Nd:YVO_4 laser,” Apply Phys B 70, 475 (2000).

[19] X. Wang, Z. Wang, Y. Bu, L. Chen, G. Cai, W. Huang, Z. Cai, and N. Chen, “Power-ratio tunable dual-wavelength laser using linearly variable Fabry–Perot filter as output coupler,” Appl. Opt. 55, 879-883 (2016).

[20] G. Shayeganrad, Y. Huang, and L. Mashhadi, “Tunable single and multiwavelength continuous-wave c-cut Nd:YVO_4 laser,” Appl. Phys. B 108, 67 (2012).

[21] C. Y. Li, Y. Bo, J.L. Xu, C.Y. Tian, Q.J. Peng, D.F. Cui, Z.Y. Xu, “Simultaneous dual-wavelength oscillation at 1116 and 1123 nm of Nd:YAG laser,” Opt. Commun. 284, 4574–4576 (2011).

[22] X. Z. Wang, Z. F. Wang, Y. K. Bu, L. J. Chen, G. X. Cai and Z. P. Cai, “A 1064- and 1074-nm Dual-Wavelength Nd:YAG Laser Using a Fabry–Perot Band-pass Filter as Output Mirror,” in IEEE Photonics Journal 6(4), 1-6 (2014).

Chapter 5

Highly efficient CW mode-locked operation of $Nd:YVO_4$ laser in-band pumped at 914 nm

The previous chapters have only discussed the continuous-wave (CW) operations of lasers where the laser power is delivered continuously in time. In this chapter, an overview of picosecond pulse generation from $Nd:YVO_4$ lasers is presented. The detailed theories of different short pulse generation techniques have been extensively studied and the information given here has been selected to accompany the experimental results within the scope of this thesis.

Diode-pumped continuous wave passively mode-locked (ML) lasers with high efficiency and high output power with picosecond (ps) pulse duration are used in multiple fields such as micromachining, nonlinear optics, and bioimaging such as multi-photon microscopy [1] and coherent anti-Stokes Raman scattering (CARS) microscopy [2]. The use of Nd:vanadate ($Nd:YVO_4$) crystal instead of the other Nd-doped laser crystals such as Nd:YAG allows for an overall more efficient laser system under ML operation. This is possible due to its very high emission cross-section, broader absorption band suitable for diode-pumping, and birefringence which is useful for further frequency conversion processes [3-5].

However, $Nd:YVO_4$ suffers from its inferior thermal properties in comparison to Nd:YAG and has been extensively studied in order to determine the thermal effects which are the main factor preventing it from being used in very high power applications [6-11]. The reduction in the thermal effect and resultant improvement in terms of thermal management have been discussed and demonstrated in Chapter 2.

As opposed to changing the cavity design parameters or the geometry of the laser crystal in order to partially compensate for the thermal effects, recent increase in availability and feasibility of the laser diodes at longer wavelengths allowed $Nd:YVO_4$ crystal to utilize other absorption lines further away from the strongest and standard one at 808 nm.

Lower QD from longer pump wavelength affects the laser system in two ways. First, it lowers the heat generation per stimulated photon which ultimately results in lower thermal load inside the gain medium. The reduction of thermal effects due to lower QD has been reported for

880, 888, and 914 nm pump wavelengths [12-16]. Moreover, the lower absorption at 880, 888, and 914 nm, allows for the absorbed pump power to be more optimally spread across a larger volume, thus further lowering the thermal lensing effects. This contributes to a better stability of the system and opens up a way for laser power scaling.

Secondly, recall again the equation describing the output power in the equation (4-2), where pumping at longer wavelength elevates the intrinsic limitation in efficiency of the laser system imposed by the QD (in terms of the ratio between ν_p and ν_L). The slope efficiency (η_s) is defined as

$$\eta_s = \frac{-\ln(1-T)}{-\ln(1-T)+L_{\lambda_i}}\frac{\nu_L}{\nu_p} \approx \frac{T_{oc}}{T_{oc}+L_{\lambda_i}}\frac{\lambda_P}{\lambda_L} \tag{5-1}$$

and is dominated only by the ratio of the pump and laser wavelengths when $L_{\lambda i} \rightarrow 0$ [17]. Therefore, the theoretical upper limit of slope efficiency of the laser system (operating at 1064 nm) can increase from 75.9% in 808 nm pumping case to 85.9% in the case of 914 nm pumping. Fortunately, high-brightness laser diodes around this wavelength are widely used for pumping of Yb-doped fiber lasers. Therefore, as was mentioned in Chapters 1 and 2, in-band pumping at 914 nm offers an attractive possibility to simultaneously achieve both high output power and high slope efficiency. Indeed, Nd:YVO_4 lasers in continuous wave regime achieved slope efficiency of up to 81% [15]. At the same time, Nd:YVO_4 lasers in mode-locked (ML) regime under 808, 880, and 888 nm pumping have been also reported [18–20]. The highest reported slope efficiency to date in ML regime was 71% in [19]. However, there was only one report by Liang et al. [21] on mode locking performance of a Nd-doped gain medium with low quantum defect pumping at the 0.9 μm absorption lines of the $^4F_{3/2} \rightarrow {}^4I_{9/2}$ transition. A diode-pumped and mode-locked Nd:$Gd_{0.6}Y_{0.4}VO_4$ laser demonstrated optical-to-optical efficiency of 27% and slope efficiency of only 44% which was caused by the non-optimal mode-matching condition for TEM00 mode as described by the authors [21].

This chapter reports the first results in ML regime under in-band pumping at 914 nm with a maximum average power of 6.7 W with 16 ps pulse duration and slope efficiency of up to 77% which, to the best of my knowledge, is the highest to date among the mode-locked Nd-doped lasers.

The principle of Semiconductor Saturable Absorber Mirror (SESAM) mode locking is outlined in the following sections along with the general design rules for laser cavity operating in mode-locked regime. Finally, the experimental setup and results showing highly efficient mode locking of Nd:YVO_4 laser will be shown and compared to the previously reported results from other Nd-doped mode-locked lasers.

5.1 Principle of mode locking

Short optical pulses are optical energy that is confined in small time windows and have a lot of applications due to either the strength of the electric field it can generate or the intense power. There are multiple ways to achieve short optical pulses. Laser systems can achieve this modulation in output optical power by varying the conditions of the cavity via introducing different mechanisms of intracavity loss modulation.

A strong loss modulation can create higher barrier for the lasing condition or higher P_{th} and results in higher number of electrons being kept in the upper energy state before being released in a short period of time when the loss is removed. This method is called Quality-switching or "Q-switching" and can be categorized as active or passive from the loss modulator. Q-switched lasers are generally used to generate nanosecond pulses [22].

In order to generate short pulses in the pico- & femtosecond range, mode locking technique is required. First, let us examine a laser under the continuous wave operation where multiple laser longitudinal modes are allowed to oscillate inside the laser cavity. Three main factors dictating the oscillating frequencies are the bandwidth of the gain medium, the laser cavity, and intracavity loss. Through standing wave condition, the possible oscillating frequencies are described as

$$v = \frac{c}{2L} q, \tag{5-1}$$

where v is the oscillating frequency, c is the speed of light, L is the cavity length, and q is a positive integer. The oscillating frequencies are illustrated in Fig. 5-1.

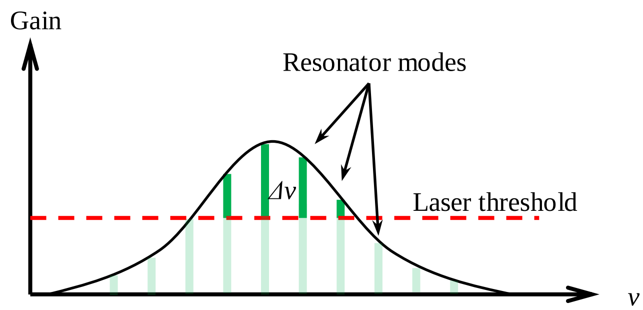

Fig. 5-1. Oscillating laser modes in the continuous wave laser operation within the gain spectrum of a laser medium.

For example, considering the case in the experiment in this chapter where the cavity length is 172.6 cm, the longitudinal mode spacing is $\Delta v = c/2L$ = 86.9 MHz or in terms of wavelength it is

$$\Delta\lambda = \frac{\lambda^2}{2L} = 3.28\ 10^{-13}\ \mathrm{m} = 3.28\ 10^{-4}\ \mathrm{nm}.$$

If the measured spectrum of the laser output is 0.07 nm (resolution of our spectrometer), it means that there are approximately 213 modes oscillating simultaneously.

Naturally, without mode locking, all modes are oscillating with random phases independent of each other and the intensity (electric field amplitude squared) of the output beam has a form as shown in Fig. 5-2(a). When all the allowed modes travel with well-defined phase relationship and the electric fields interfere constructively at a common point in the cavity, there will only be one light pulse traveling inside the laser cavity and the laser output becomes a periodic train of short pulses and is said to be mode-locked [23-25]. An example of the intensity of seven oscillating modes with locked phases is shown in Fig. 5-2(b).

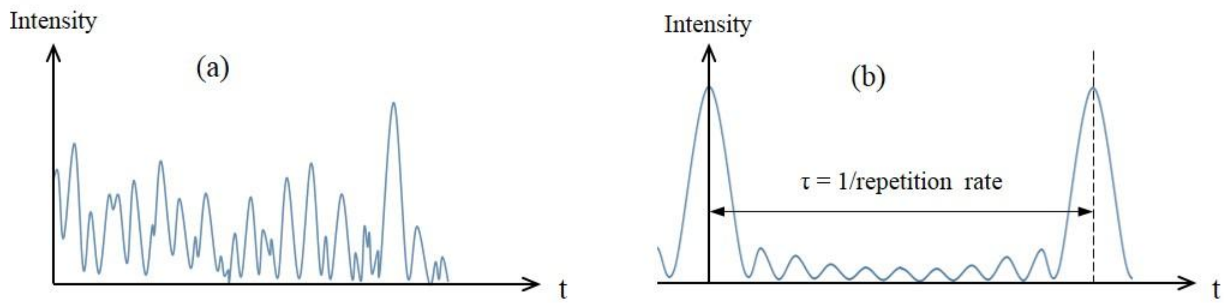

Fig 5-2. Example of electric field amplitude squared (intensity) of the output beam (a) without mode locking and (b) with mode locking.

In mode-locked operation, pulse formation can be described as controlling of the phase relationship between multiple oscillating modes traveling inside of an optical resonator (laser cavity) by introducing an additional optical element that is responsible for introducing either amplitude or phase modulation.

Mathematically, the process of mode locking starts with the oscillating mode with the highest gain determined by the enveloping laser crystal gain spectrum and represented by the electric field of a plane wave ($E(t)$). The periodic loss modulation can be written as

$$L(t) = M(1 - \cos(\omega_m t)), \tag{5-2}$$

where M is the modulation depth and ω_m is the modulation frequency. Fourier transform of the product of $E(t)$ and $L(t)$ describes the result of the plane wave with loss modulation in frequency domain and is written as

$$FT\{M(1-\cos(\omega_0 t)) \times E(t)\} = 2\pi M \delta(\omega_0) - 2\pi \frac{M}{2}\left[\delta(\omega_0 + \omega_m) + \delta(\omega_0 - \omega_m)\right], \tag{5-3}$$

which shows that two more frequency components, $\omega_0 + \omega_m$ and $\omega_0 - \omega_m$, or side bands, are generated from the original wave after one round of loss modulation. As this process continues, more frequency components that are supported by the laser crystal gain spectrum will be generated with fixed phase relationship. This will couple all of the produced modes in phase, resulting in their constructive interference and pulse formation.

To achieve mode locking, an optical element capable of weak optical loss modulation is introduced into the laser cavity in order to allow short moments at which the net laser gain becomes positive. In active mode locking, this periodic loss modulation is done through either acousto-optic or electro-optic modulators. In passive mode locking, the loss modulation intervals are governed by the high intensity of the laser pulse itself by utilizing passive optical elements such as semiconductor saturable absorber mirror (SESAM) or Kerr medium inside the laser cavity and thus ensuring a faster response time. Unlike Kerr-lens mode locking, SESAM mode locking provides far more tolerance to misalignment, more flexibility to the cavity design, and also the ability to achieve mode locking operation at the center of the cavity stability region. However, due to the static parameters of the SESAM, it is possible to encounter a certain type of unstable mode locking which will be covered more in detail in section 5.1.2.

5.1.1 Mode locking with SESAM

A semiconductor saturable absorber mirror (SESAM) consists of two important parts, an InGaAs quantum well (QW) absorber and a Bragg reflector on a semiconductor substrate. The typical structure of a SESAM is shown in Fig. 5-3 (a). Recent advancements in saturable absorber include quantum wires, or single-walled carbon nanotubes (SWCNT) showing semiconductor-like behavior, and quantum dots, which could provide better pulse shaping and allow for faster recovery time and can help or, in some cases, replace KLM as the main pulse shaping mechanism. They have been demonstrated alongside the original QW saturable absorber mirror with comparable results as seen in [27] whereas the main advantages of using SWCNT-SA is mainly due to the simplicity in fabrication which can now provide a real low-cost solution to produce mode-locked ultrafast lasers.

The interest in this thesis, however, emphasizes on the overall efficiency of the ML laser with 914 nm pumping scheme which can be demonstrated using various types of saturable absorbers. Therefore, the QW semiconductor saturable absorber mirrors were used in the experiments.

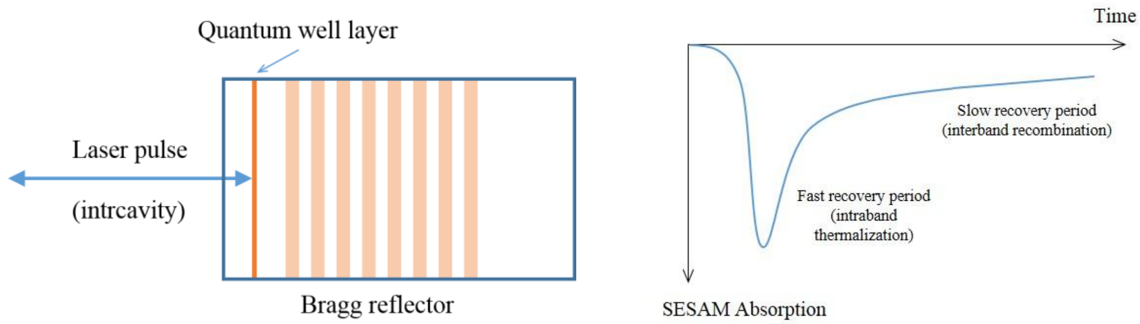

Fig. 5-3 (a) Structure of a SESAM and (b) SESAM recovery mechanisms.

A Bragg reflector part of a SESAM is a periodic set of layers with slightly different refractive indices. For the wavelength that satisfies the Bragg condition,

$$\lambda = 2n\Lambda , \tag{5-5}$$

where λ is the wavelength, n is the refractive index, and Λ is the thickness of one period of the Bragg reflector, the reflected wave constructively interferes resulting in a very high reflection. Therefore Bragg reflector acts as a wavelength dependent semiconductor HR mirror. The role of Bragg reflector is to reduce the electric field intensity incident on QW layer and increase the damage threshold of the SESAM itself which cannot be accomplished with one reflective surface.

The quantum well absorber introduces the loss into the laser resonator by absorbing photons with enough energy to excite its electrons from the valence band to the conduction band. However, if the excitation rate is strong enough (which happens at high light intensity), the valence band can become depleted thus reducing the loss and resulting in the SESAM becoming saturated.

Important parameters of a SESAM are

1. Center wavelength and reflection band of the Bragg mirror (λ_0, $\Delta\lambda$).
2. Saturable loss (ΔR, i.e. modulation depth) indicates the maximum difference in the level of reflectivity under maximum absorption and no absorption.
3. Non-saturable (parasitic) loss (A_{ns}) as shown in Fig. 5-4.
4. Saturation fluence ($F_{sat,SESAM}$, pulse energy per unit area) which is defined as the fluence that can reduce the absorption of SESAM to 1/e of its initial value. Therefore, the higher

intensity pulses are favored for oscillation inside the laser cavity and the lower intensity light is suppressed.

5. Recovery time of the SESAM governed by slow interband recombination (~ps-ns) which can be reduced by proton bombardment at the expense of the higher non-saturable loss and ultimately higher threshold for laser operation.

At the start of the mode-locked operation, a random fluctuation of intensity inside the laser cavity that is strong enough to bleach the SESAM will see a lower loss and therefore will allow for the time windows with higher net gain. During the subsequent round-trips a pulse narrowing will take place where the leading edge of the pulse gets shaved off by the bleaching of the SESAM, eventually leading to its final pulse duration.

5.1.2 Q-switching instabilities and multi-pulsing

Ranges of mode-locked operation can be classified into the 3 main categories, continuous-wave mode locking regime (CW-ML), Q-switched mode locking regime (QS-ML, not to be confused with Q-switching), and multi-pulsing. The latter two are generally undesirable and thus are called mode locking instabilities and can occur due to the recovery dynamics of the SESAM.

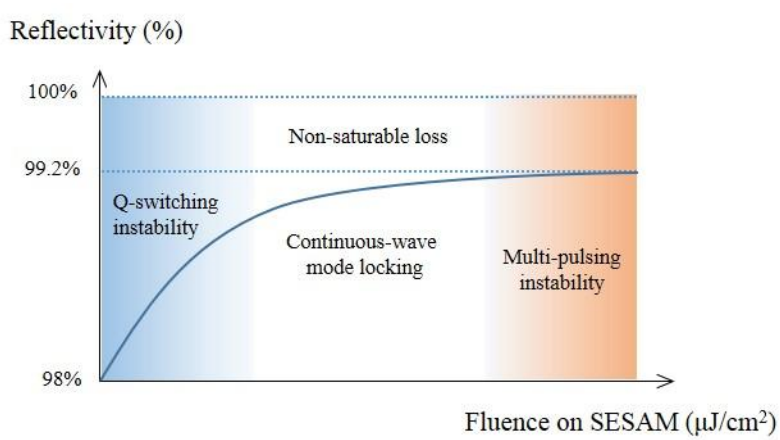

Fig. 5-4 Reflectivity versus fluence on SESAM showing the regions prone to Q-switching and multi-pulsing instabilities.

The examples of the pulse trains relative to their round-trip time (τ_P) for different ranges of operation are shown in Fig 5-5. QS-ML can be described as the range of operation with a slow periodic modulation (> μs) enveloping the mode-locked pulse intensity.

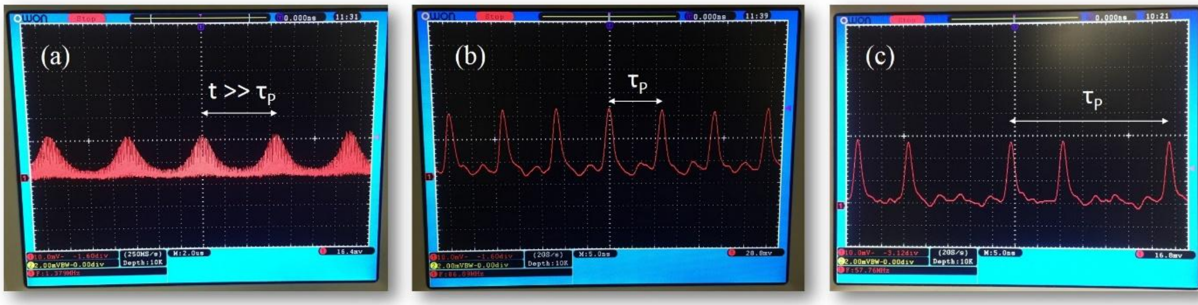

Fig. 5-5 ML pulse trains with (a) Q-switching instability, (b) no instability, and (c) multi-pulsing.

In order to avoid QS-ML, the effect of gain saturation from the gain medium comes into play in order to suppress the buildup of the intracavity pulse energy. The saturation energy of the gain medium ($E_{sat,Laser}$) is described by

$$E_{sat,Laser} = F_{sat,L} A_L = \frac{h\nu}{m\sigma} A_L, \tag{5-6}$$

where $F_{sat,L}$ is the fluence on the gain medium, A_L is the beam area on the gain medium, m is the number of passes through the gain medium per round trip and σ is the emission cross-section. At the pump power multiple times above the threshold, the saturation energy of the gain medium is the only factor from gain medium contributing to the QS-ML condition. The criteria for avoiding QS-ML was derived by Hönninger et al. [28] as

$$E_p^2 > E_{sat,Laser} E_{sat,SESAM} \Delta R, \tag{5-7}$$

where E_p is the pulse energy traveling inside the cavity, $E_{sat,SESAM}$ is the saturation energy of the SESAM and equals to $F_{sat,SESAM}$ multiplied by the laser mode area on it, and ΔR is the modulation depth of the SESAM. From this relationship we can say that gain media with larger stimulated emission cross-section provide a more relaxed condition for avoiding the QS-ML since it decreases the gain saturation fluence. However, for any given laser system, using multiple passes can help manipulate the gain saturation even further.

Contrary to the QS-ML, multi-pulsing instability occurs at high levels of fluence on SESAM. This is due to the inability for the laser system to differentiate between the two conditions, a single pulse traveling inside the laser cavity and multiple pulses, if both conditions provide approximately the same level of saturation of the absorber. From Fig. 5-4 we can see that the $dR/dF_{sat,SESAM}$ is much smaller at higher levels of $F_{sat,SESAM}$ which is the cause of this types of instability. Therefore, the multi-pulsing instability acts as the upper limit to the output power under mode-locked operation for a particular laser system.

Both types of unstable mode locking can be detected by careful inspection of the pulse trains at different time windows or by radio frequency (RF) measurements which will be covered in the results section of this chapter.

5.1.3 Optimum design

Taking all the factors mentioned above into accounts, we can draw a diagram as shown in Fig. 5-6 connecting various parameters in order to explain the trade-offs for a particular case of mode-locked lasers.

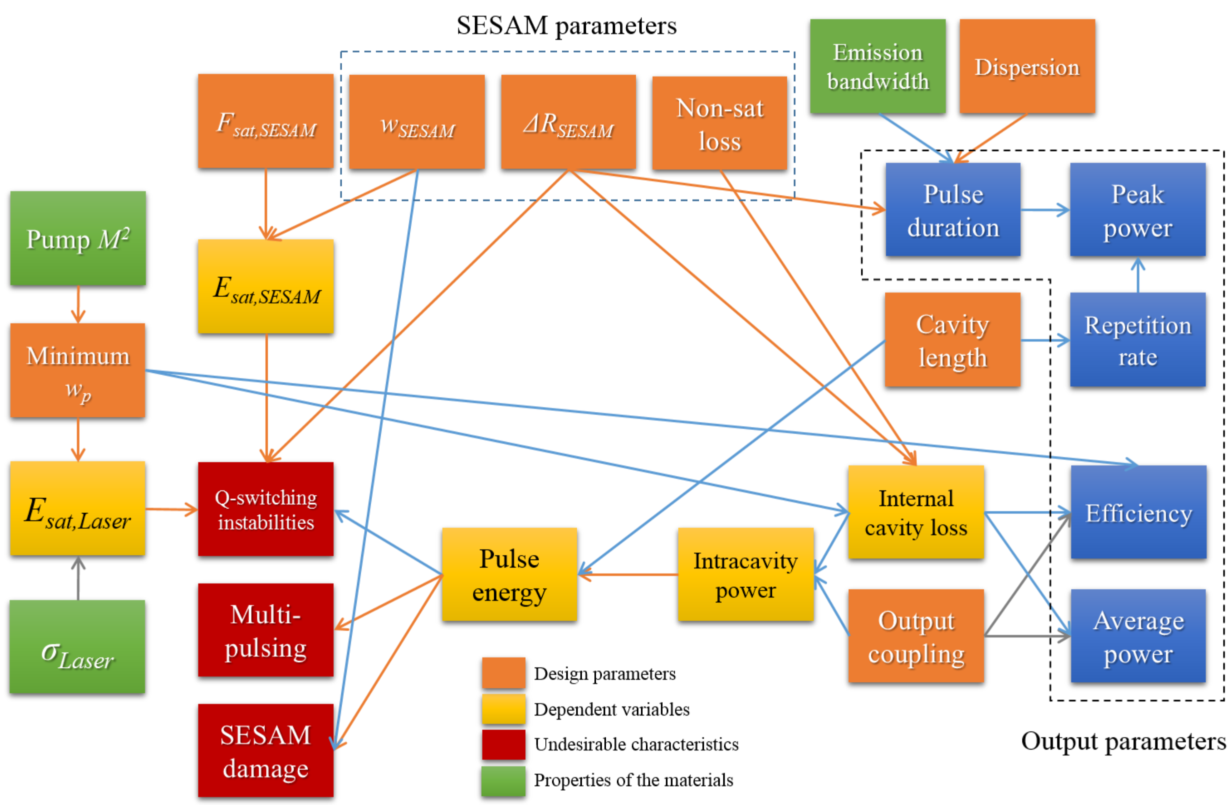

Fig. 5-6. Diagram showing the connections between various parameters of a mode-locked laser. Orange arrows denote direct relationship between two variables and blue arrows denote inverse

relationship. The grey arrows from OC to efficiency and average power denote non-monotonic relationships.

Due to the intricate nature of the connections between these variables, the information from thermal lensing measurement in Chapter 2 is very useful here. Among these parameters w_{SESAM} and w_p are the parameters that reflect the changes from thermal lensing.

5.2 Experimental setup

Multiple resonator configurations were used with different SESAMs available in the experiment. The following setup described here gives the highest output power and efficiency.

A 20-mm-long a-cut $Nd:YVO_4$ crystal (Castech) with doping level of 1.5 at.% was antireflection (AR) coated for both pump and laser wavelengths in order to reduce internal cavity loss. The crystal was pumped by a fiber-coupled laser diode (iPG Photonics) with 110 μm core diameter and numerical aperture of 0.12 at 914 nm. The laser diode was water cooled at 16 °C to control the wavelength shift due to temperature change and was capable of delivering 16.8 W of pump power at 914 nm. At this wavelength its spectrum was ~3.8 nm wide at FWHM (full width at half maximum). The pump was focused into a 275 μm spot radius at the center of the crystal through a set of coupling lenses with 1:5 magnification. The $Nd:YVO_4$ crystal was wrapped in indium foil and constantly water cooled on the top and bottom surfaces in a metal holder at 16 °C in order to control the thermal effects.

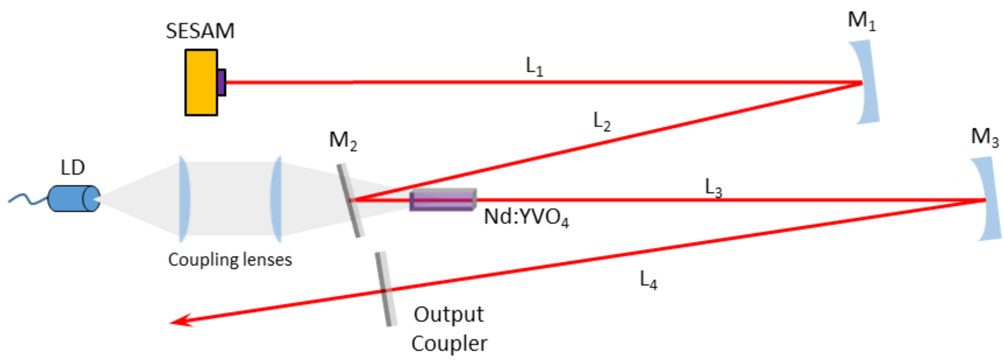

Fig. 5-7. Experimental setup for mode-locked operation of a $Nd:YVO_4$ laser diode-pumped at 914 nm. LD, laser diode.

A 5-mirror cavity was used with a reflective SESAM as one of the end mirrors as shown in Fig. 5-7. The dichroic pump mirror M_2 served as a folding mirror and was AR-coated for 914 nm and highly reflected (>99.9%) laser radiation at 1064 nm. The radii of curvature of M_1 and M_3 were 400 mm and 500 mm, respectively. The distances L_1, L_2, L_3, and L_4 were 33, 47.5, 48.1, and 45.0 cm, respectively. At the highest absorbed pump power (and with thermal lensing taken into account) the spot size of the laser mode at the center of the crystal was 270 μm and ensured constant and efficient mode-matching with the pump beam while the spot size radius on SESAM was 175 μm. The laser cavity was designed to have a proper spot size on SESAM in order to control its fluence and to achieve mode locking with the highest output power [28]. This enabled us to avoid multi-pulse mode locking and damage of the SESAM.

The SESAM (BATOP GmbH) with 1.2% modulation depth, 0.8% non-saturable loss, 90 $\mu J/cm^2$ saturation fluence, and relaxation time constant of ~10 ps was used. The SESAM was soldered onto a gold plated Cu-cylinder.

A stable, self-starting, continuous wave mode-locked output with the highest output power was achieved with a 15% output coupler (OC). The mode-locked pulse train was recorded by a 6 GHz digital oscilloscope (Tektronix, TDS6604) with a fast InGaAs photodetector (Thorlabs, DET08CFC/M) giving an overall temporal resolution of ~100 ps. An autocorrelator with a delay range of 200 ps (Femtochrome Research, FR-103XL) was used to measure the pulse duration and monitor multi-pulse instabilities.

5.3 Experimental results

Since the specification of the laser diode has changed from the one given in Chapter 2 and the crystal doping concentration is higher in this experiment, the laser diode wavelength and the absorbed power versus laser diode optical power are given again here. The pump absorption at 914 nm displayed nonlinearity as shown in Fig. 5-8 due to the wavelength shift of the laser diode. This was taken into account for further analysis of the performance of the developed laser oscillator. Pump absorption by the crystal was 66% at the highest level of pump power.

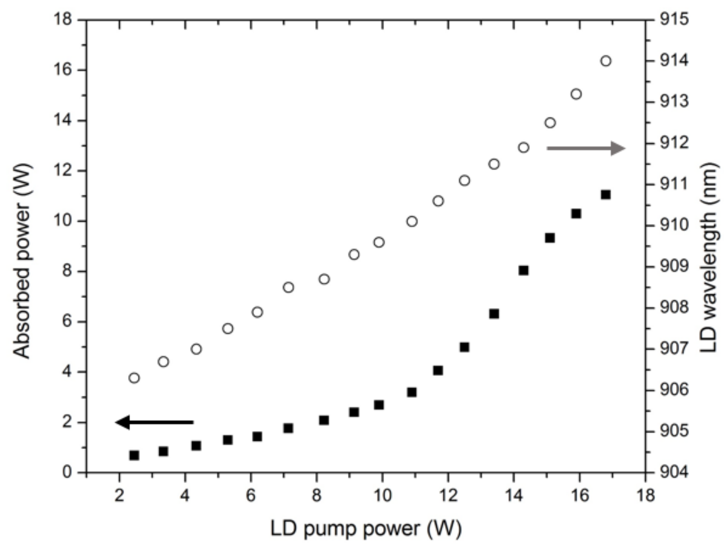

Fig. 5-8. Pump absorption (left axis) and center wavelength of the laser diode (right axis) versus the laser diode optical power

5.3.1 CW operation with 5-mirror cavity

When SESAM was replaced with an HR (High Reflectivity) mirror, the performance in the continuous wave regime could be obtained. The output power and slope efficiency in CW is shown in Fig. 5-9 along with output power from ML regime for comparison. The measured slope efficiency of 76.7% was very close to the limitation imposed by quantum defect. The optical-to-optical efficiency was 65.7% at 7.26 W of maximum output power.

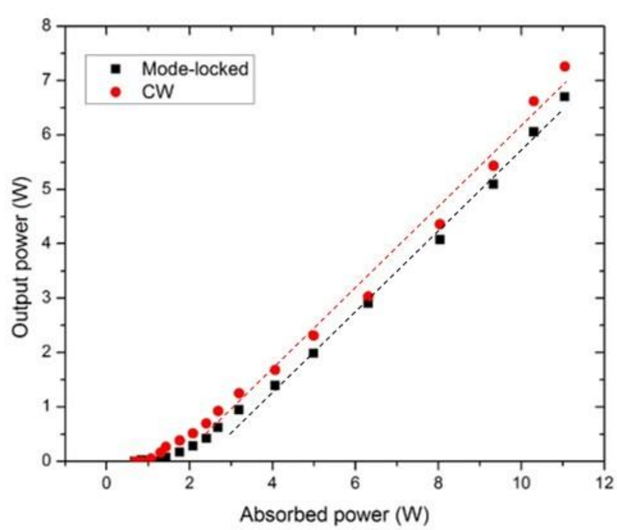

Fig. 5-9. Output power versus absorbed power in continuous wave and ML regimes.

5.3.2 Mode locking results

The laser output power versus the absorbed pump power in ML regime is presented again in Fig. 5-10 with detail of different ranges of operation. After 0.94 W of output power, Q-switched mode-locked (QS-ML) operation was observed as shown in the pulse train in the middle inset. Above 4.1 W of output power, the laser started operating in continuous wave mode-locked regime. At 11.0 W of absorbed pump power, the maximum output power of 6.7 W was obtained with 60.7% of optical-to-optical efficiency and 77.1% of slope efficiency in the ML regime. This slope efficiency is much higher than the reported values of 55.2% for the commonly used pumping scheme at 808 nm [29-34] and higher than 71% previously reported at 880 nm [19]. Assuming a reasonable internal cavity loss of ~0.9% that was introduced by different cavity elements (i.e. crystal and mirrors which were all specified to have <0.1% loss per surface/reflection) and 0.8% from the non-saturable loss introduced by the SESAM, the maximum possible slope efficiency can be calculated as ~77.2%. This is in good agreement with the experimentally achieved slope efficiency and shows that it is mainly limited by the intracavity loss. Therefore by carefully managing of the intracavity loss either by using a SESAM with lower non-saturable loss or by lowering the number of optical elements inside the cavity, it is possible to increase the slope efficiency even further.

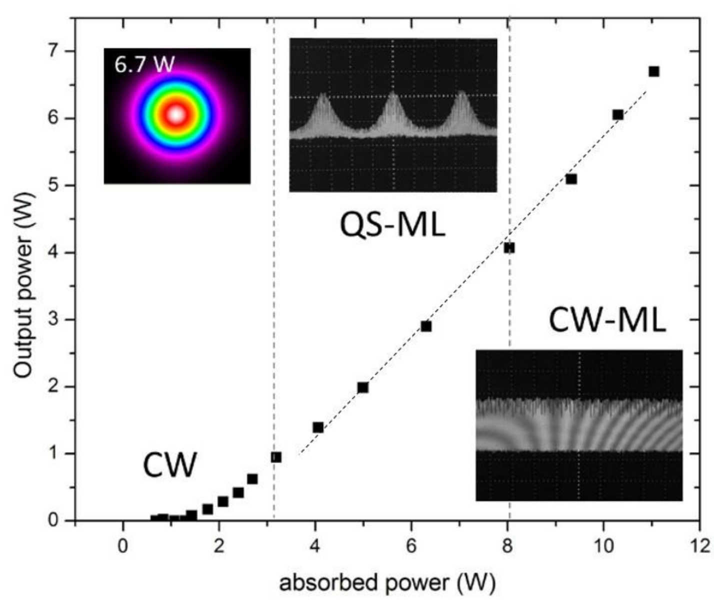

Fig. 5-10. Average output power of the $Nd:YVO_4$ laser versus the absorbed pump power. Insets: beam intensity profile at maximum output power, QS-ML pulse train and ML pulse train over 30 μs and 15 μs time periods, respectively.

The obtained optical-to-optical efficiency with respect to incident pump power (40%) can be also increased by using a longer gain medium with higher doping concentration to maximize pump absorption. Since the beam quality of the laser diodes available at 914 nm is much better than for the 808 nm diodes, maintaining good mode-matching even in a long crystal is not an issue.

The slope efficiency shows no sign of decreasing at the highest output power which suggests that the output power was not limited by the thermal lensing effects but by the available pump power. Due to the lower absorption coefficient of $Nd:YVO_4$ at 914 nm as compared to the other absorption lines, a longer crystal or multiple pass pumping scheme can be used to further increase the output power.

The beam quality factor M^2 was measured by a beam profiler to be less than 1.4. Throughout the experiment, the output beam exhibited TEM_{00} mode beam profile as shown in the inset of Fig 5-10. This is due to the fact that the cavity was designed with preliminary measurement of thermal lensing effect [16,35] which at the highest pump power level was found to be ~160 mm. The other insets in Fig. 5-10 also show the pulse trains in the QS-ML and ML regimes within the time spans of 30 μs and 15 μs, respectively.

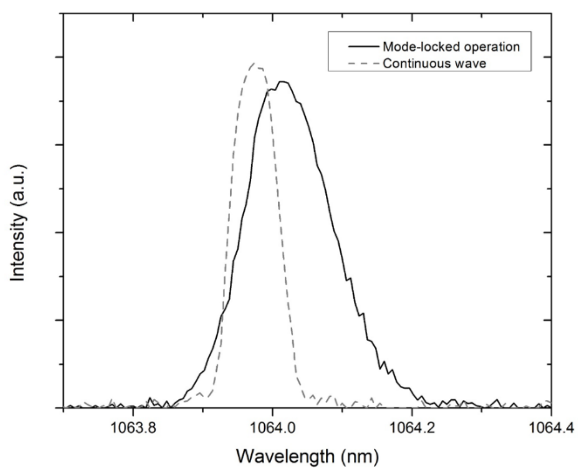

Fig. 5-11. Optical spectrum of the laser output in continuous wave and ML operation.

Figure 5-11 shows the broadening of the optical spectrum when the laser operation changes from the continuous wave to the continuous wave mode-locked regime. The FWHM of the spectra are 0.14 and 0.07 nm, respectively, and was limited by the resolution (0.07 nm) of the available optical spectrum analyzer (Anritsu, MS9710B).

At maximum output power, a pulse width of 16 ps was measured and deconvoluted by an intensity autocorrelator corresponding to the time bandwidth product of 0.593 which indicates a chirped pulse. According to the recorded spectrum, the generation of pulses shorter than 10 ps should be possible. The autocorrelation trace with its corresponding fitting assuming *sech*^{2}-shaped pulses is presented in Fig. 5-12(a). The radio frequency (RF) spectrum in Fig. 5-12(b) displays stable mode locking at ~87 MHz repetition rate with noise suppressed to better than 51 dB. In addition, Fig. 5-12(c) shows an RF spectrum spanning 0-500 MHz also indicating clean, stable mode locking without multi-pulse instabilities.

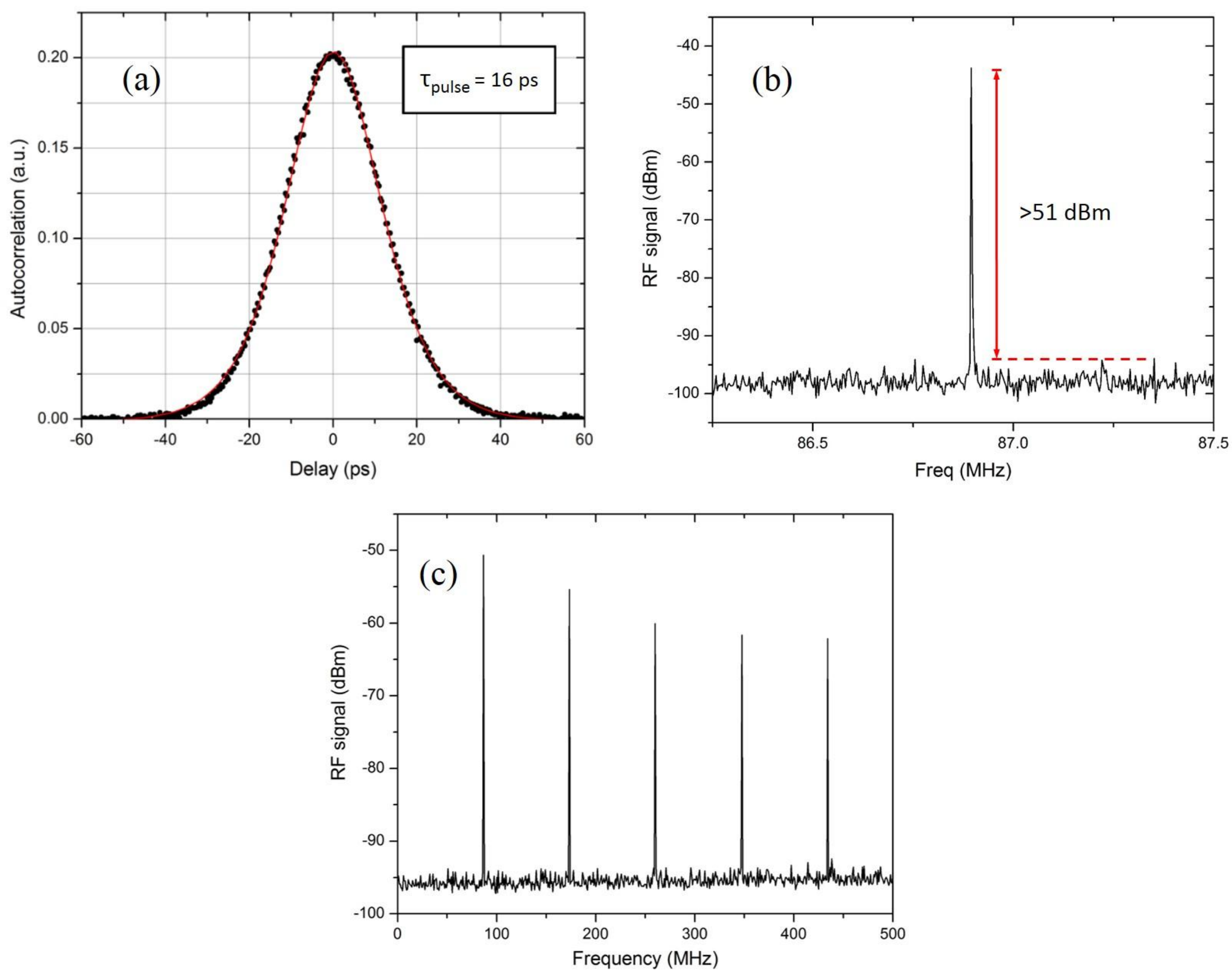

Fig. 5-12. (a) Autocorrelation trace (dots) and *sech*^{2}-fit (line) of the output pulse in CW-ML operation. (b) Radio frequency (RF) spectrum of the mode-locked laser. (c) RF signal in the 0-500 MHz range.

From the measured average output power, pulse duration, and repetition rate, we can calculate the peak power of the pulse and the maximum pulse energy, assuming that the laser operates in stable CW-ML which is clearly the case in our measurement. The pulse duration and repetition rate at the highest average output power corresponded to the peak power and maximum pulse energy of 4.8 kW and 77.2 nJ, respectively.

5.4 Conclusion

In summary, a diode-pumped passively mode-locked Nd:YVO_4 laser with optical-to-optical efficiency up to 60.7% and slope efficiency of 77.1% under the new pumping wavelength of 914 nm was demonstrated. This is the highest slope efficiency for the ML Nd:YVO_4 lasers reported to date and for the ML Nd-doped lasers in general. This result for the first time confirms the advantages of in-band pumping at 914 nm over the standard pumping at 808 nm in the ML regime. The measured slope efficiency was limited by the intracavity losses and therefore can be further improved by careful intracavity loss management. The maximum average output power of 6.7 W was achieved with a pulse duration of 16 ps and was limited only by the available pump power. Further power scaling can be done both by the increase of pump power or increase of the absorbed pump power using a longer gain medium and higher doping concentration. We believe that the same concept can be extended and to other Nd-ion based gain media to produce highly efficient mode-locked laser systems.

References

[1] H. Yokoyama, H. Guo, T. Yoda, K. Takashima, K. Sato, H. Taniguchi, H. Ito, “Two-photon bioimaging with picosecond optical pulses from a semiconductor laser,” Opt. Express. 14, 3467 (2006).

[2] C. Evans and X. Xie, “Coherent anti-Stokes Raman scattering microscopy: chemical imaging for biology and medicine,” Annu. Rev. Anal. Chem. 1, 883 -909 (2008).

[3] Y. Sato and T. Taira, “Spectroscopic properties of neodymium-doped yttrium orthovanadate single crystals with high-resolution measurement,” Jpn. J. Appl. Phys. 41, 5999-6002 (2002).

[4] A. J. Lee, D. J. Spence, J. A. Piper, and H. M. Pask, “A wavelength-versatile, continuous-wave, self-Raman solid-state laser operating in the visible,” Opt. Express 18, 20013-20018 (2010).

[5] A. Major, D. Sandkuijl, V. Barzda, "Efficient frequency doubling of a femtosecond Yb:KGW laser in a BiB3O6 crystal," Optics Express, 17(14), 12039-12042 (2009).

[6] A. Sennaroglu, "Experimental determination of fractional thermal loading in an operating diode-pumped Nd:YVO_4 minilaser at 1064 nm," Appl. Opt. 38, 3253-3257 (1999).

[7] F. Song, C. Zhang, X. Ding, J. Xu, and G. Zhang, "Determination of thermal focal length and pumping radius in gain medium in laser-diode-pumped Nd:YVO_4 lasers," Appl. Phys. Lett. 81, 2145 (2002).

[8] Z. Xiong, Z. G. Li, N. Moore, W. L. Huang, and G. C. Lim, "Detailed Investigation of Thermal Effects in Longitudinally Diode-Pumped Nd:YVO_4 Lasers," IEEE J. Quantum Electron. 39, 979-986, (2003).

[9] X. Huai and Z. Li, "Thermal stress analysis of a Nd:YVO_4 laser medium end pumped by a Gaussian beam," Appl. Phys. Lett. 92, 041121 (2008).

[10] R. Soulard, A. Zinoviev, J. L. Doualan, E. Ivakin, O. Antipov, and R. Moncorge, "Detailed characterization of pump-induced refractive index changes observed in Nd:YVO_4, Nd:$GdVO_4$ and Nd:KGW," Opt. Express 18, 1553-1568 (2010).

[11] Y. R. Peng, Y. Xin, C. D. Ying, C. Fei, L. X. Dong, M. Y. Fei, and Y. J. Hua, "The thermal effect in diode-end-pumped continuous-wave 914-nm Nd:YVO_4 laser," Chin. Phys. B 21, 024208 (2012).

[12] L. McDonagh, R. Wallenstein, R. Knappe, and A. Nebel, "High-efficiency 60W TEM_{00} Nd:YVO_4 oscillator pumped at 888 nm," Opt. Lett. 31, 3297-3299 (2006).

[13] N. Pavel, C. Krankel, R. Peters, K. Petermann, and G. Huber, "In-band pumping of Nd-vanadate thin-disk lasers," Appl. Phys. B 91, 415 (2008).

[14] Y. J. Wang, W. H. Yang, H. J. Zhou, M. R. Huo, Y. H. Zheng, "Temperature dependence of the fractional thermal load of Nd:YVO_4 at 1064 nm lasing and its influence on laser performance," Opt. Express 21, 18068-18078 (2013).

[15] D. Sangla, M. Castaing, F. Balembois, and P. Georges, "Highly efficient Nd:YVO_4 laser by direct in-band diode pumping at 914 nm," Opt. Lett. 34, 2159-2161 (2009).

[16] T. Waritanant and A. Major, “Thermal Lensing in Nd:YVO_4 Laser with In-Band Pumping at 914 nm,” Appl. Phys. B 122, 135 (2016).

[17] W. P. Risk, “Modeling of longitudinally pumped solid-state lasers exhibiting reabsorption losses,” J. Opt. Soc. Am. B 5, 1412-1423 (1988).

[18] Z. Cai, W. Wen, Y. Wang, Z. Zhang, X. Ma, X. Ding, and J. Yao, “5.3-W Nd:YVO_4 passively mode-locked laser by a novel semiconductor saturable absorber mirror,” Chin. Opt. Lett. 3, 342-344 (2005).

[19] L. Sun , H. J. Yu, L. Zhang, L. Guo, J. Zhang, Z. Y. Dong, B. Xiong, W. Hou, X. C. Lin, and J. M. Li, “High efficiency passive mode-locked Nd:YVO_4 laser based on SESAM under direct pumping at 880 nm,” Laser Phys. 21, 1765-1768 (2011).

[20] L. McDonagh, R. Wallenstein, and A. Nebel, “111W, 110 MHz repetition-rate, passively mode-locked TEM00 Nd:YVO_4 master oscillator power amplifier pumped at 888 nm,” Opt. Lett. 32, 1259-1261 (2007).

[21] H. C. Liang, Y. J. Huang, P. Y. Chiang, and Y. F. Chen, “Highly efficient Nd:$Gd_{0.6}Y_{0.4}VO_4$ laser by direct in-band pumping at 914 nm and observation of self-mode-locked operation,” Appl. Phys. B 103, 637–641 (2011).

[23] H. A. Haus, “Mode-locking of lasers,” IEEE J. Sel. Top. Quantum Electron. 6, 1173–1185 (2000).

[24] U. Keller, “Recent developments in compact ultrafast lasers,” Nature 424, 831–838 (2003).

[25] U. Keller, “Ultrafast solid-state laser oscillators: a success story for the last 20 years with no end in sight,” Appl. Phys. B 100, 15–28 (2010).

[27] A. Schmidt, S. Rivier, W. B. Cho, J. H. Yim, S. Y. Choi, S. Lee, F. Rotermund, D. Rytz, G. Steinmeyer, V. Petrov and U. Griebner, “Sub-100 fs single-walled carbon nanotube saturable absorber mode-locked Yblaser operation near 1 μm,” Opt. Express 17, 20109–20116 (2009).

[28] C. Hönninger, R. Paschotta, F. Morier-Genoud, M. Moser, and U. Keller, “Q-switching stability limits of continuous-wave passive mode locking,” J. Opt. Soc. Am. B 16, 46-56 (1999).

[29] D. J. Farrell and M. J. Damzen, "High power scaling of a passively modelocked laser oscillator in a bounce geometry," Opt. Express 15, 4781-4786 (2007).

[30] J. Cui, Z. Fan, Y. Xue, J. Zhang, G. Niu, Z. Shi, B. Pei, Y. Bi, and Y. Qi, "LD end-pumped 1.5-W passively CW mode-locked Nd:YVO_4 laser," Chin. Opt. Lett. 5, S42-S43 (2007).

[31] Z. Sun, X. Lin, H. Yu, T. Hasan, F. Torrisi, L. Zhang, L. Sun, L. Guo, W. Hou, J. Li, and A. Ferrari, "High-power ultrafast solid-state laser using graphene based saturable absorber," in CLEO:2011 - Laser Applications to Photonic Applications, OSA Technical Digest (CD) (Optical Society of America, 2011), paper JWA79.

[32] X. Fu, J. Li, and X. Liang, "Compact high-power mode-locked Nd:YVO_4 picosecond laser using multiple-pass cavity," Chin. Opt. Lett. 11, 081401 (2013).

[33] C. Y. Tang, Y. Chai, H. Long, L. Tao, L. H. Zeng, Y. H. Tsang, L. Zhang, and X. Lin, "High-power passively mode-locked Nd:YVO_4 laser using SWCNT saturable absorber fabricated by dip coating method," Opt. Express 23, 4880-4886 (2015).

[34] V. S. Aleksandrov, H. Iliev, and I. Buchvarov, "$\chi(2)$-lens mode-locking of a Nd:YVO_4 laser with high average power and repetition rate up to 600 MHz," in CLEO: 2015, OSA Technical Digest (online) (Optical Society of America, 2015), paper JW2A.76.

[35] H. Mirzaeian, S. Manjooran, and A. Major, "A simple technique for accurate characterization of thermal lens in solid state lasers," Proc. SPIE 9288, 928802 (2014).

Chapter 6

Selectable Multi-Wavelength Operation of a SESAM Mode-locked Nd:YVO_4 Laser

To expand upon the mode locking results of Chapter 5, we can also recall the tunability of the Nd:YVO_4 laser demonstrated in Chapter 3. Aside from one report of passive mode locking at 1086 nm from Nd:$LuVO_4$ crystal with a custom made SESAM and mode-locked pulse width of 144 ps [1], so far both 1073 nm and 1085 nm emission lines from the Nd:YVO_4 have not been demonstrated in the mode locking regime.

Wavelength selectivity in the mode locking regime also has not been reported. In a typical mode-locked laser selection between the three wavelengths mentioned in Chapter 3 requires, however, a change of cavity lengths, OC, and spot size on SESAM in order to accommodate for the change in intracavity power owing to a large disparity in the stimulated emission-cross sections at different wavelengths.

This chapter reports the discrete wavelength tuning results from a single setup of a stable, self-starting, passively mode-locked Nd:YVO_4 laser operating at 1064 nm, 1073 nm, and 1085 nm with the use of an intracavity birefringent plate as the tuning element. The laser did not require any changes in setup except for the rotation of the BRF.

6.1 Experimental setup

The laser crystal used was still a 3x3x20-mm-long a-cut 1.5% doped Nd:YVO_4 crystal. The laser was pumped by the same fiber-coupled diode laser at 914 nm to reduce thermal effects. The crystal was water cooled on both top and bottom surfaces at 16 °C. The schematic diagram of the laser cavity is shown in Fig 6-1.

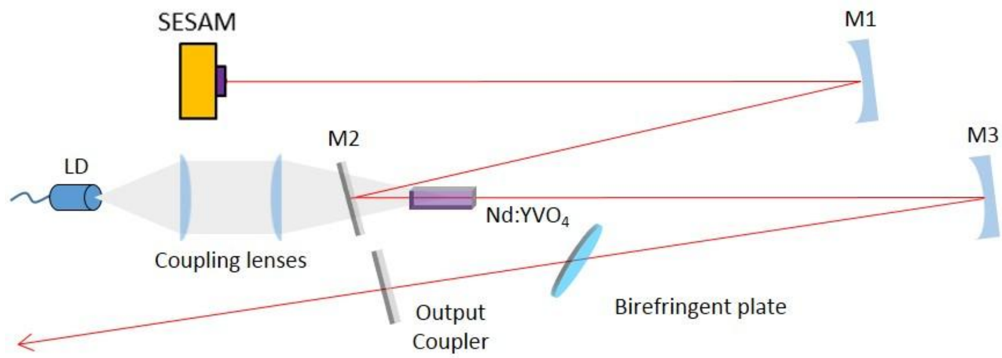

Fig. 6-1. Experimental setup for tunable mode-locked $Nd:YVO_4$ laser operation.

The total cavity length in this case was 1.77 m. The spot size radius on SESAM was changed to 150 μm while keeping the laser mode size at 275 μm by changing the separation between each mirror. The reason for a smaller spot size on SESAM was due to the much smaller emission cross-sections at 1073 and 1085 nm which significantly influence the criteria for stable mode locking as seen in equations (5-5) and (5-6).

At the highest incident pump power, 11.0 W was absorbed in the crystal. The pump spot size was 270 μm at the center of the gain medium. A SESAM with 1.2% modulation depth and 90 $\mu J/cm^2$ saturation fluence was used as one of the end mirrors. A 4-mm-thick birefringent plate was inserted into the cavity at the Brewster's angle to achieve the discrete tuning of the laser output wavelength. Stable, self-starting, continuous wave mode-locked operations for all three wavelengths at 1064, 1073, and 1085 nm were achieved with a ~2.1% OC. Since the small change in the reflectivity of the OC can influence the criteria for QS-ML, the specification for the reflectivity of the OC is also given in Fig. 6-2 to confirm that the change in reflectivity is relatively small within the range of operation. The reflectivities at 1064, 1073, 1085 nm are 2.07, 2.06, and 2.11%, respectively.

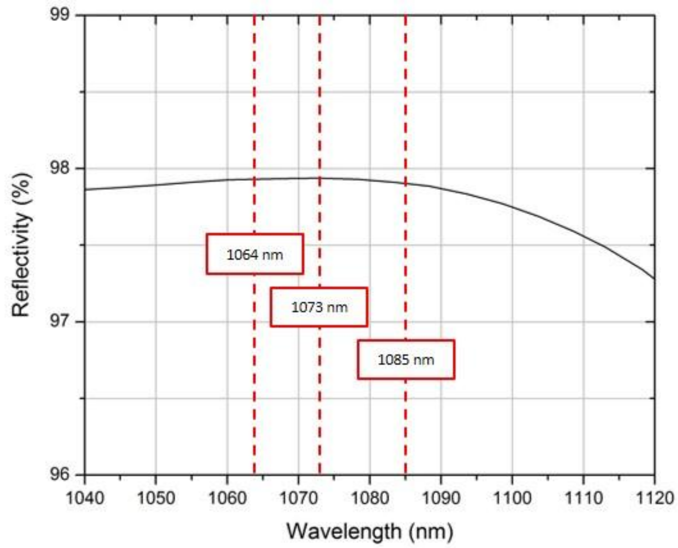

Fig. 6-2. Reflectivity of the OC used to obtain discretely wavelength tunable ML operation.

6.2 Results and discussion

The continuous wave mode-locked operations were achieved at all three wavelengths, 1064.0 nm, 1073.0 nm, and 1085.1 nm with the highest output powers of 2.79 W, 2.17 W, and 2.18 W, respectively with the same BRF plate and OC. The laser output power versus the absorbed pump power is plotted in Fig. 6-3 (a). The discrete tuning of the mode-locked laser wavelength was done by rotating the intracavity birefringent plate. The optical-to-optical efficiency and slope efficiency are 25.3% and 29.1% for the 1064 nm output, 19.6% and 31.3% for the 1073 nm output, and 19.7% and 31.2% for the 1085 nm output. The beam quality (M^2) was again less than 1.4 for all laser wavelengths. The higher threshold power levels for both the 1073 nm and 1085 nm outputs were due to the lower emission cross-sections for these lines. To the best of our knowledge, this is the first report of the mode-locked operations at 1073 nm and 1085 nm and also discrete wavelength tuning of the mode-locked Nd:YVO_4 laser.

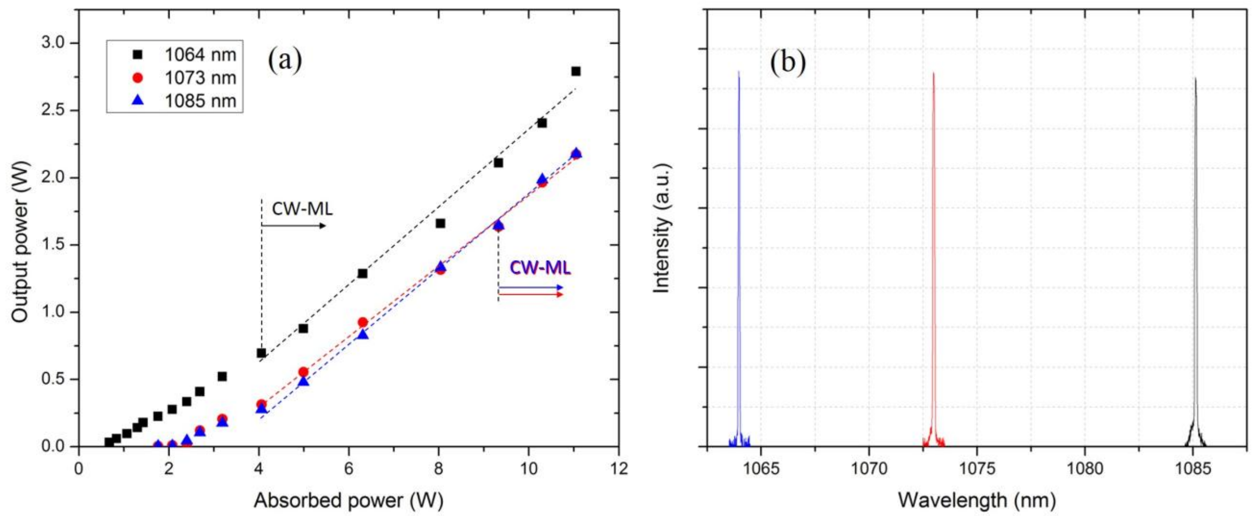

Fig. 6-3 (a). Output power for three different mode-locked output at 1064, 1073, and 1085 nm. (b) The three laser output spectra under ML operation.

Fig. 6-3 (b) shows the optical spectra for the three obtained wavelengths. The FWHM of the spectra in the mode-locked regime are 0.14 nm, 0.11 nm, and 0.11 nm, for output at 1064 nm, 1073 nm, and 1085 nm, respectively. The autocorrelation traces with their $sech^2$ fit curves are shown in Fig. 6-4 and were used to calculate the following pulse durations.

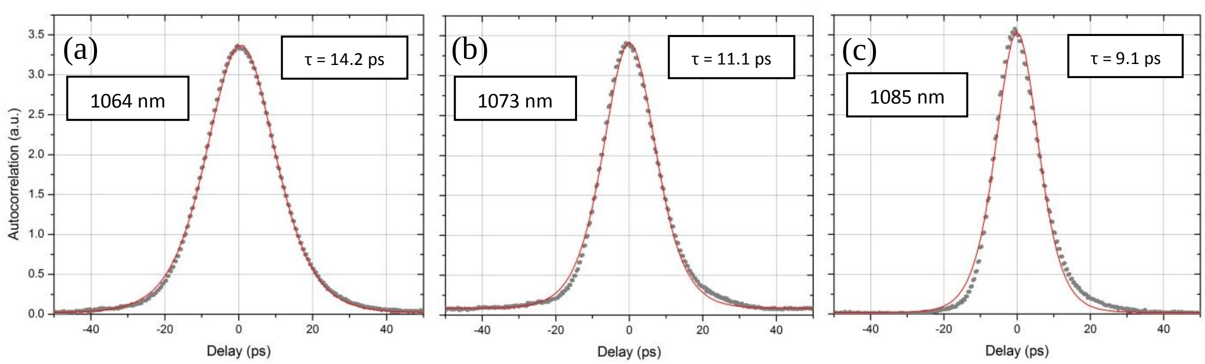

Fig. 6-4. Autocorrelation traces and $sech^2$ fits of the output pulses in the CW-ML operation at (a) 1064 nm, (b) 1073 nm, and (c) 1085 nm.

The pulse durations at the highest output power levels were 14.2 ps, 11.1 ps, and 9.1 ps. The radio frequency (RF) spectra were also recorded with signal-to-noise separation of more than 45 dBm and show no sign of Q-switched mode locking or multi-pulsing at the highest output power for all of the three wavelengths (see Figs. 6-5 and 6-6).

The repetition rate for the cavity was ~84.9 MHz which was confirmed with the RF measurements as shown in Fig. 6-5.

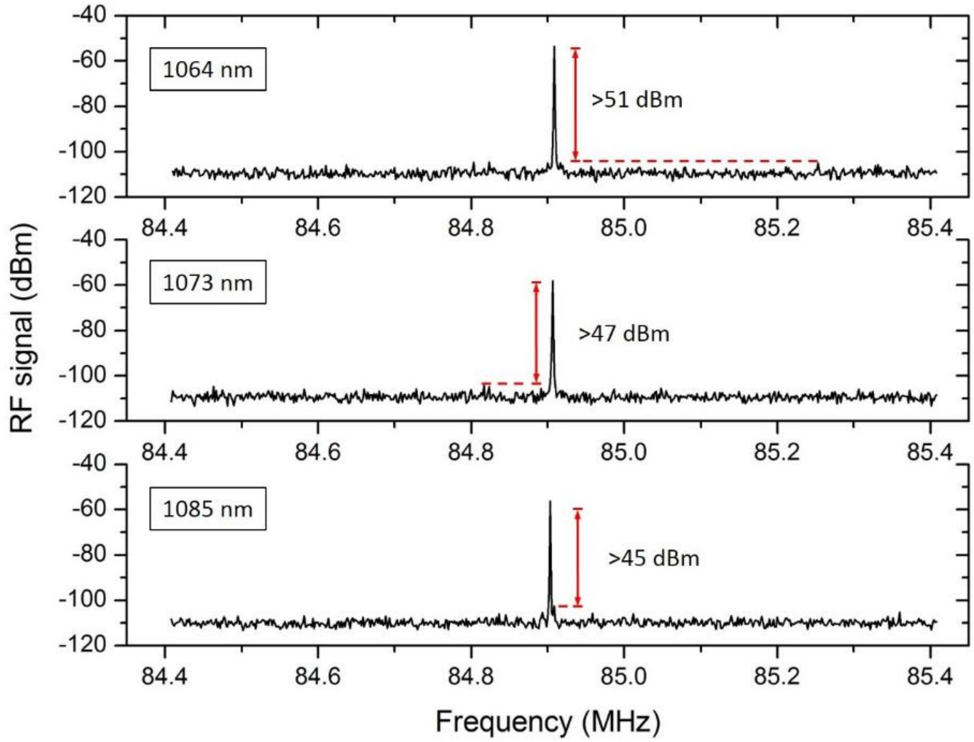

Fig. 6-5. RF spectra of the mode-locked lasers close to the fundamental frequency (~84.9 MHz).

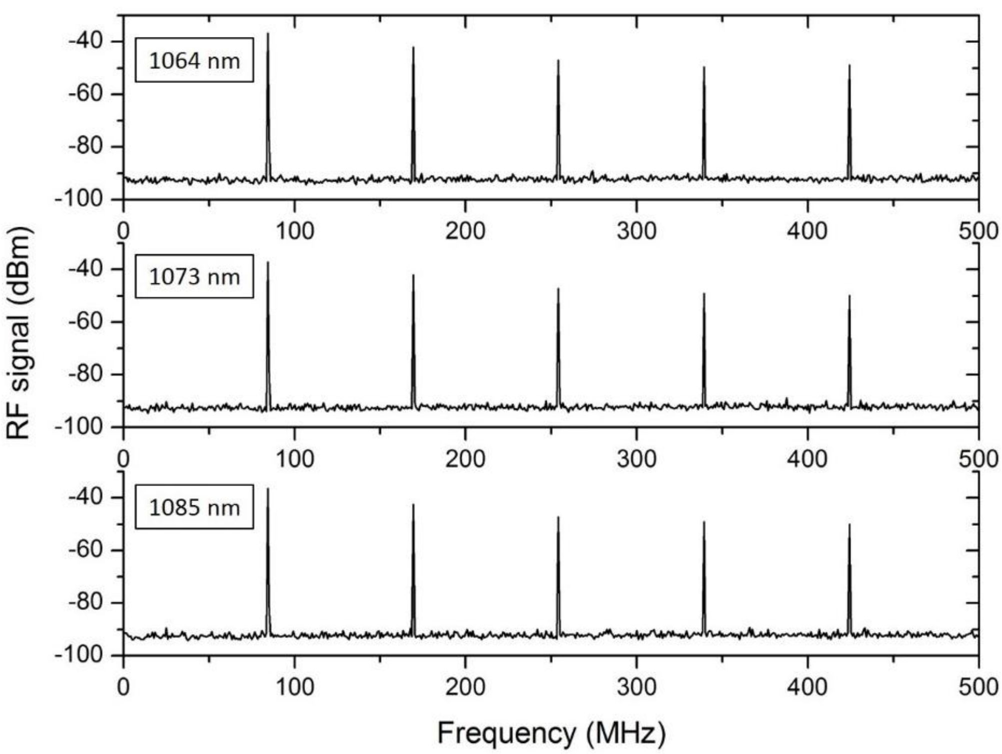

Fig. 6-6. RF spectra in the 0-500 MHz range.

Following the similar calculation for the peak power and pulse energy for a stable mode-locked laser at the end of the last chapter, the resulting discretely wavelength tunable laser had the peak powers of 2.04 kW, 2.03 kW, 2.48 kW and pulse energies of 32.9 nJ, 25.6 nJ, 25.7 nJ for laser outputs at 1064 nm, 1073 nm, and 1085 nm, respectively.

6.3 Conclusions

A discrete wavelength tuning of a mode-locked Nd:YVO_4 laser operating at 1064.0 nm, 1073.0 nm, and 1085.1 nm was demonstrated for the first time. Wavelength tuning was realized with a birefringent plate as the tuning element. The output power of more than 2.2 W at 11.0 W of absorbed pump power was achieved for all three wavelengths with slope efficiencies of more than 29% in ML regime, and optical to optical efficiencies of more than 19%. The generated pulse durations were 14.2 ps, 11.1 ps, and 9.1 ps respectively.

References

[1] J. H. Lin, P. K. Yang, and W. C. Lin, "Passively mode-locked pulse generation in a c-cut Nd:$LuVO_4$ laser at 1086 nm with a semiconductor saturable-absorber mirror," J. Phys. B: At. Mol. Opt. Phys. 45, 085403 (2012).

Chapter 7

Alternative ultrashort pulse gain media under 914 nm pumping

Since the previous chapters of this thesis have demonstrated that the direct in-band pumping at 914 nm can provide clear advantages over other pump wavelengths in terms of reduction in thermal lensing and increase of efficiency, the same concept can be applied to other Nd-doped materials as well. The ability to pump Nd:KGW laser at 910 nm was also investigated with a similar experimental setup [1,2]. For the next logical step, a further study should be made with Nd:YVO_4's sister material, Neodymium gadolinium vanadate (Nd:$GdVO_4$), which has the most similarity in terms of crystal parameters and performance.

Such low quantum defect pumping schemes are also particularly advantageous for laser gain media with disordered structures such as Nd:glass since they are generally constrained by poor thermal conductivity (κ). This chapter provides the experimental findings from low quantum defect pumping at 914 nm of two gain media with disordered structure, Nd:$ScYSiO_5$ (Nd:SYSO) and Nd:$CaYAlO_4$ (Nd:CALYO). To the best of my knowledge, this is the first report of such experiments with these gain media.

7.1 Nd:$CaYAlO_4$ (Nd:CALYO)

Nd:CALYO crystal was first proposed as a new candidate for disordered structure laser crystal in 1977 by E. F. Kustov et al. [3] where the absorption and emission spectra of single crystals of Nd:CALYO were initially reported. H. R. Verdún and L. M. Thomas later reported the first laser operation with Nd:CALYO pumped by a GaAlAs diode laser array [4] in 1990.

Nd:CALYO was the first laser crystal discovered that was isostructural with tetragonal K2NiF4 structure where the Ca^{2+}, Y^{3+}, and Nd^{3+} can randomly occupy the same crystallographic site. This random distribution of different species creates the same effect as disordered crystals. The main reason for interest in Nd:CALYO was because of the disordered crystal structure which translates to spectral properties as seen in Nd:Glass, Nd:CNGG, and Nd:CLNGG media, i.e. smooth inhomogeneous broadening of absorption and emission spectral lines. At the same time the crystal of Nd:CALYO still retained the thermal properties closer to the other crystals with ordered structure such as Nd:YVO_4. The inhomogeneous broadening of the emission spectrum ultimately can allow generation of shorter pulses.

The absorption spectra of the uniaxial Nd:CALYO can be seen in Fig. 7-1(a) and were measured by D. Z. Li et al. [5]. The typical pump band of interest was at 805 nm because of the availability of the AlGaAs pump diodes. The spectra also show small absorption past 900 nm for both polarizations indicated by the light red bands.

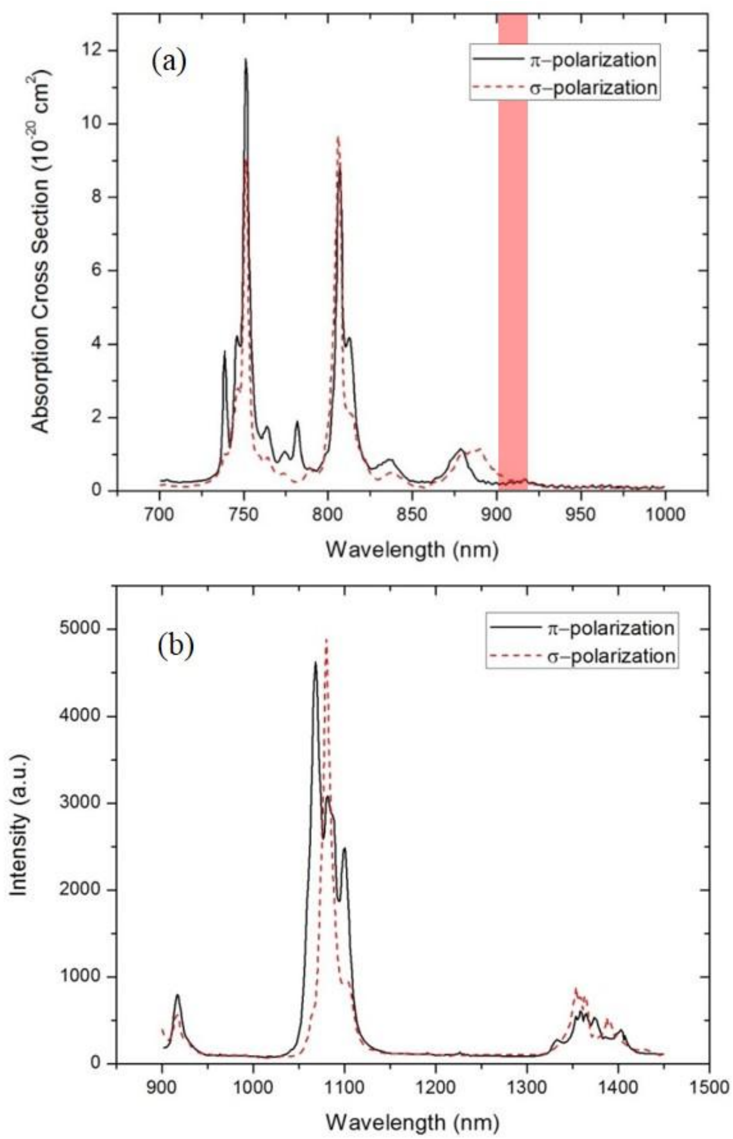

Fig. 7-1. Polarized (a) absorption and (b) emission spectra of Nd:CALYO [5]. Colored areas (red) represent the wavelengths available from the pump laser diode in the experiments.

While there are multiple absorption bands available, the typical pump band of interest is at 805 nm because of the availability of the pump diode generally employed in the diode-pumped solid state laser (GaAlAs). The FWHMs of the main emission band at 1080 nm ($^4F_{3/2} \rightarrow {}^4I_{11/2}$ transition) are 12 nm for σ-polarization and 15 nm for π-polarization and the spectra are given in Fig. 7-1(b). The FWHM for σ-polarization is approximately 20 times larger than that of Nd:YVO_4 emission band at 1064 nm. These large FWHMs of the absorption and emission bands are clear evidence of the disordered structure of Nd:CALYO. Birefringent property of the Nd:CALYO crystal is the result of the tetragonal crystallographic structure and is beneficial in applications such as mode locking and others that require linearly polarized laser output.

While the absorption and emission linewidths are many times larger than those of the ordered structure crystals, the main disadvantages of Nd:CALYO when compared to Nd:YVO_4 are the smaller peak absorption and emission cross-sections. These disadvantages result in higher laser threshold and lower optical efficiency.

7.2 Nd:$ScYSiO_5$ (Nd:SYSO)

Nd:SYSO is a newer crystal first demonstrated in CW and Q-switched regimes by S. D. Liu et al. [6] and in passive mode-locked regime by V. Aleksandrov et al. [7]. The absorption cross-sections for different cuts of Nd:SYSO are shown in Fig. 7-2(a) [8]. Similar to Nd:CALYO, there is small absorption for the wavelengths longer than 900 nm. Table 7-1 provides a comparison between the optical and thermal properties of Nd:YVO_4, Nd:CALYO, and Nd:SYSO.

Table 7-1. Comparison of several optical and mechanical properties of Nd:YVO_4, Nd:CALYO, and Nd:SYSO

Laser Crystal	λ_{em} (nm)	σ_{em} (10^{-20} cm^2)	Δλ (nm)	K_c ($Wm^{-1}K^{-1}$)	α_T ($10^{-6}K^{-1}$)	dn/dT ($10^{-6}K^{-1}$)	τ (μs)	Ref.
Nd:YVO_4	1064	141 (π)	0.96	∥C 5.23 ⊥C 5.10	α_a 4.43 α_c 11.37	n_o 8.5 n_e 15.5	90	[9,10]
Nd:CALYO	1080	10.44 (σ)	15	∥C 3.2 ⊥C 3.6	α_a 8 α_c 11	n_o 8.5 n_e 12	114	[3,5]

Nd:SYSO	1075.6	9.92	15.4	-	-	-	-	[8]

As can be seen from Table 7-1, both Nd:CALYO and Nd:SYSO have clear advantages over Nd:YVO_4 in terms of emission bandwidth as shown in Fig. 7-2(b) which offers a possibility of sub-picosecond pulse generation while trading away some of the thermal properties in the case of Nd:CALYO.

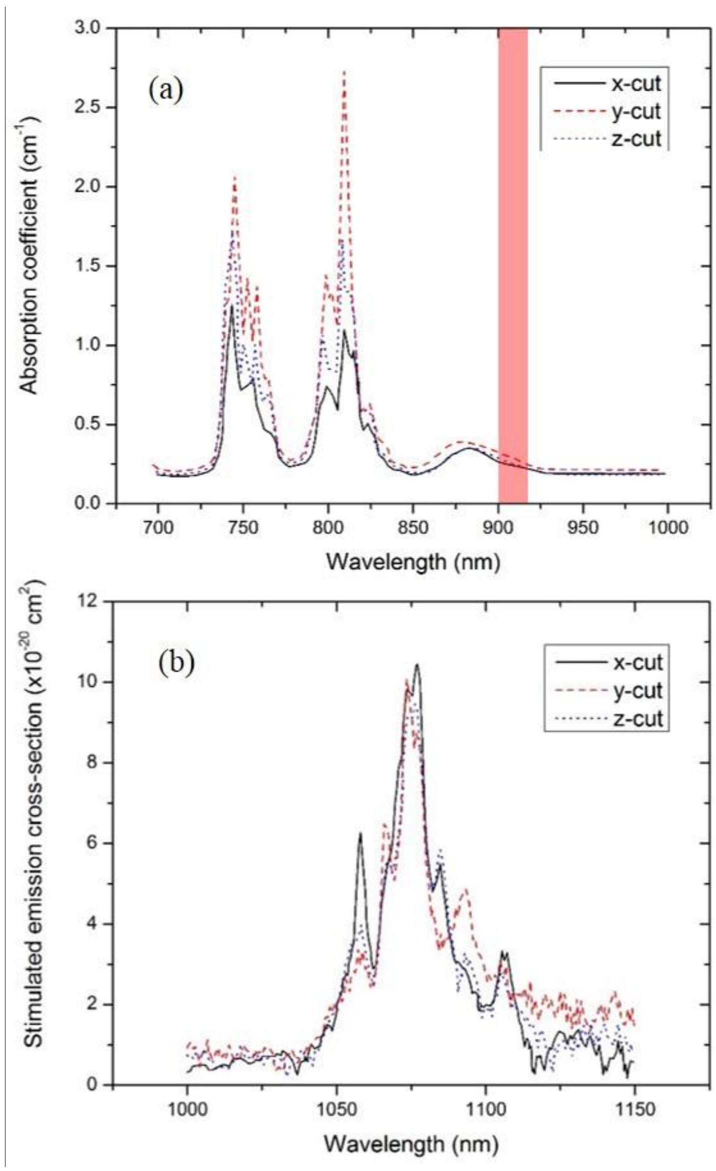

Fig. 7-2. (a) Emission and (b) absorption spectra of Nd:SYSO for 3 different cuts [8]. Colored areas (red) represent the wavelengths available from the pump laser diode in the experiments.

This section demonstrates for the first time low quantum defect pumping at 914 nm of these two gain media with disordered structure, Nd:CALYO and Nd:SYSO.

7.3 Experimental setup

A 20-mm-long Nd:CALYO crystal was used in a 3-mirror cavity as shown in Fig. 7-3. The crystal was pumped by a fiber-coupled diode laser with a fiber core diameter of 105 μm and a numerical aperture of 0.15. The maximum pump power was limited to 24.3 W. The pump was then coupled into the crystal with a set of achromatic doublet with 40 mm focal length and 150 mm focal length. The spot size of the pump beam at the center of the gain medium was 197 μm.

The crystal was wrapped in indium foil and water cooled in a copper holder at 16 °C at the flow rate of 1 liter/minute on the top and bottom surfaces. The gain medium was in-band pumped at 914 nm at the highest pump power level. Both surfaces of the crystal were anti-reflection coated (R < 0.5%) at the laser wavelength. M3 was a dichroic mirror with high reflection at 1080 nm (T > 99.9%). An output coupler (OC) with 1.6% transmission in the 1040-1090 nm range was used in the experiment in order to determine the highest output power and optical efficiency.

In another experiment, two 5-mm-long 0.8 at. % doped Nd:SYSO crystals were used in a similar 3-mirror cavity setup (see Fig. 7-3). The optimum output coupler in this case was found to be 5%.

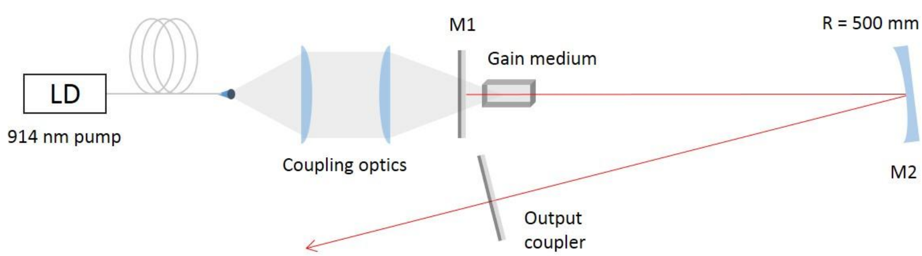

Fig. 7-3. 3-mirror laser cavity used in the experiment for both Nd:CALYO and Nd:SYSO

7.4 Results and discussions

The absorbed pump power was 9.0 W and 3.3 W for the Nd:CALYO and Nd:SYSO crystals, respectively. Fig. 7-4 shows the absorbed pump power versus the laser diode power. The experimental results were limited by the low pump absorption in the crystals which could be increased further by higher doping concentration, longer crystal in the case of Nd:SYSO, or utilizing multiple pass geometry. Regarding the available pump power, high-power fiber-coupled laser diodes around 914 nm (>100 W) are widely used for pumping of Yb-doped fiber lasers and are readily available for further power scaling experiments.

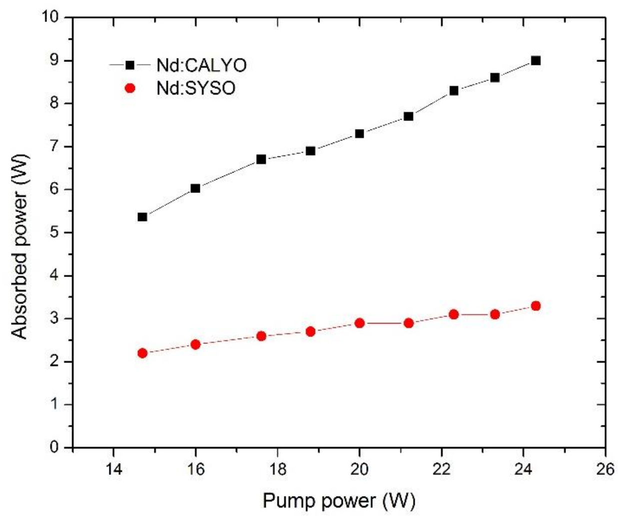

Fig. 7-4. The absorbed power versus the incident pump power for Nd:CALYO and Nd:SYSO.

The output power achieved was 201 mW for the Nd:SYSO and 154 mW output for the Nd:CALYO. Fig. 7-5 shows the measured output power for both crystals. The highest slope efficiency obtained from Nd:SYSO laser was 18.6% while the slope efficiency from Nd:CALYO laser was only 7.8%.

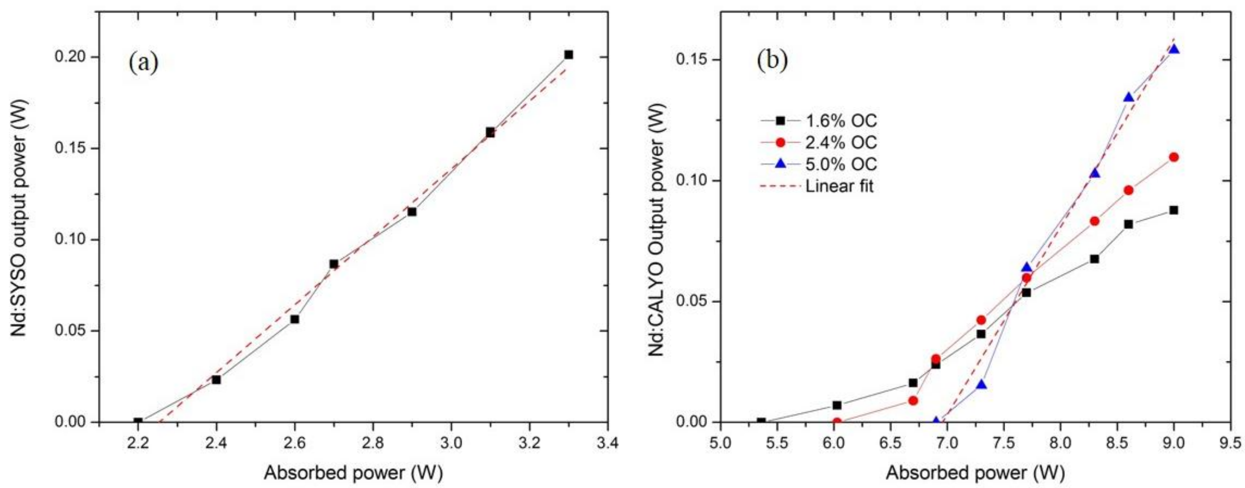

Fig 7-5. (a) The output power versus absorbed power for Nd:SYSO. (b) The output power versus the absorbed pump power for Nd:CALYO with various values of output coupler transmission.

The laser spectra are shown in Fig. 7-6. The central wavelengths are 1079.8 nm for the Nd:CALYO and 1074.9 nm for the Nd:SYSO. The FWHM are 0.14 nm and 0.17 nm, respectively.

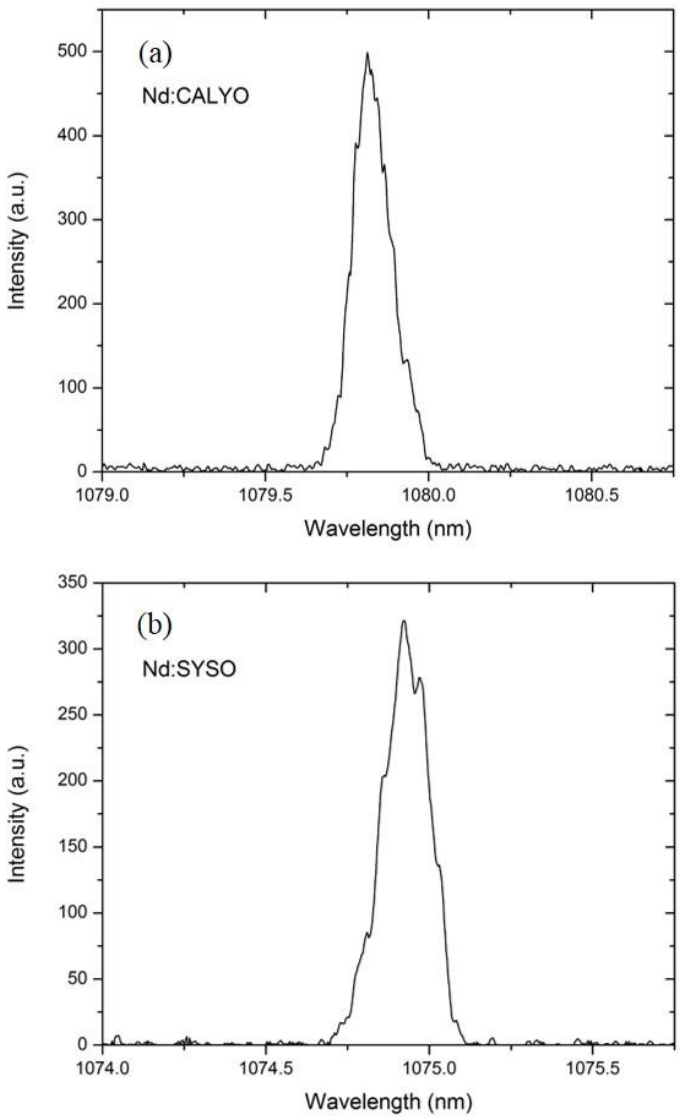

Fig. 7-6. Laser spectra of (a) Nd:CALYO and (b) Nd:SYSO.

7.5 Conclusions

Two proof-of-principle neodymium lasers with disordered structure gain media, Nd:SYSO and Nd:CALYO, were demonstrated with in-band pumping at 914 nm for the first time. The maximum output power achieved was 201 mW centered at 1074.9 nm with slope efficiency of 18.6% for Nd:SYSO and 154 mW output centered at 1079.8 nm with 7.8% slope efficiency for Nd:CALYO. This pumping approach offers further power scaling possibility due to the availability of powerful InGaAs laser diodes around 910 nm, the strongly reduced quantum defect and, consequently, thermal lensing.

References

[1] R. C. Talukder, Md. Z. E. Halim, T. Waritanant, and A. Major, "Multiwatt continuous wave Nd:KGW laser with hot-band diode pumping," Opt. Lett. 41, 3810-3812 (2016).

[2] M. Z. Eibna Halim, R. C. Talukder, T.Waritanant, A. Major, "Passive mode locking of a Nd:KGW laser with hot-band diode pumping," Laser Phys. Lett. 13, 105003 (2016).

[3] Kustov, E. F., Petrov, V. P., Petrova, D. S., and Udalov, J. P., "Absorption and luminescence spectra of $Nd^{3\pm}$ and $Er^{3\pm}$ ions in monocrystals of $CaYAlO_4$," Phys. Stat. Sol. (a) 41(2), 379-383 (1977).

[4] Verdún, H. R. and Thomas, L. M., "Nd:$CaYAlO_4$–a new crystal for solid-state lasers emitting at 1.08 μm," Appl. Phys. Lett. 56(7), 608-610 (1990).

[5] Li, D. Z., Xu, X. D., Cheng, S. S., Zhou, D. H., Wu, F., Zhao, Z. W., Xia, C. T., Xu, J., Zhang, J., Zhu, H. M., and Chen, X. Y., "Polarized spectral properties of Nd^{3+} ions in $CaYAlO_4$ crystal," Appl. Phys. B 101, 199-205 (2010).

[6] Liu, S. D., Zheng, L. H., He, J. L., Xu, J., Xu, X. D., Su, L. B., Yang, K. J., Zhang, B. T., Wang, R. H., and Liu, X. M., "Passively Q-switched Nd:Sc0.2Y0.8SiO5 dual-wavelength laser with the orthogonally polarized output," Opt. Express 20(20), 22448-22453 (2012).

[7] Aleksandrov, V., Iliev, H., Zheng, L., Su, L., Xu, J., Aka, G., and Bucharov, I., "Passive Mode-locking of a Diode Pumped Nd:$ScYSiO_5$ Laser," CLEO:2014, OSA Technical Digest (online) (Optical Society of America, 2014), paper JTu4A.127.

[8] Liu, S. D., Zheng, L. H., Xu, J., Zhang, Y. P., Zhang, H. Y., Li, D. H., Ren, T. Q., Zhang, B. T., and He, J. L., "Anisotropy of laser emission in monoclinic Nd:$ScYSiO_5$ crystals cut along the optical indicatrix axes," Chin. Opt. Lett. 14(2), 021406 (2016).

[9] Huai, X. and Li Z., "Thermal stress analysis of a Nd:YVO_4 laser medium end pumped by a Gaussian beam," Appl. Phys. Lett. 92(4), 041121 (2008).

[10] Sato, Y. and Taira, T., "Highly accurate interferometric evaluation of thermal expansion and dn/dT of optical materials," Opt. Express 4(5), 10528 (2006).

Chapter 8

Conclusion

In conclusion, this thesis proposed to study Neodymium-doped laser crystals as an alternative for ultrashort pulse generation with medium output power level and high efficiency. The first half of this thesis focused on the thermal effect which is the main limitation in power scaling. Thermal lensing effect in Nd:YVO_4 laser with in-band pumping at 914 nm was studied as an alternative to the classical 808 nm pumping scheme in order to relieve the output power limitation. FEA simulation was also done to compare the thermal lensing effect with 914, 888, 880, and 808 nm pumping. The results showed that the thermal lens power is significantly reduced because of two reasons, one, the difference in quantum defect and two, the thermal lens geometry.

Aside from thermal lens effect investigation, with the available Nd:YVO_4 laser setup, discrete wavelength tuning by a birefringent plate was reported at 1064.0, 1073.1, and 1085.2 nm. Two dual-wavelength operations were also demonstrated at 1064.1 & 1073.1 nm and 1064.1 & 1085.3 nm with two intracavity birefringent plates where the output power ratio of the dual-wavelength output could be freely adjusted.

The in-band pumped continuous wave Nd:YVO_4 laser formed an ideal platform for the development of a pulsed oscillator based on the principle of mode locking. As a result, mode-locked operation with SESAM as saturable absorber was demonstrated for the first time with the highest efficiency to date. The output in CW-ML regime was stable and self-starting with pulse width of 16 ps. The mode-locked operation was then extended to adjacent emission lines at 1073 nm and 1085 nm while still maintaining the CW-ML range of operation that could be switched between each wavelength simply by the rotation angle of the intracavity BRF plate.

To continue the in-band pumping study of Nd:YVO_4, the next step would be to use now commercially available laser diodes at 914 nm with up to 100 W of output power to push power scaling even further, to test pump absorption saturation, and to perform frequency conversion experiments.

Finally, other important candidates for low quantum defect pumping such as Nd:CALYO and Nd:SYSO were identified and tested with in-band pumping around 914 nm for the first time. The efficiency improvement and optimization are still required for these two crystals with disordered structure and are the prime candidates for the future works on ultrashort pulse generation.

Appendix A – ABCD matrix formulation

In the field of optics, originally proposed as a tool for light rays propagation, the term ABCD matrix refers to the matrix that provides enough information of an optical element in order to transform the information contained in the light propagating through that particular optical element. An ABCD matrix can be written as

$$M_{ABCD} = \begin{pmatrix} A & B \\ C & D \end{pmatrix}. \tag{a-1}$$

Recall from Chapter 2, a Gaussian beam with wavelength λ can be fully represented by a pair of parameters. The parameter $q(z)$ is then defined to represent two beam parameters $w(z)$ and $r(z)$ as

$$\frac{1}{q(z)} = -i\frac{\lambda}{\pi w(z)^2} + \frac{1}{r(z)} \tag{a-2}$$

which represents the Gaussian beam at distance z. Following the analogy between Gaussian beams and spherical waves in geometrical optics, the same ABCD matrices from geometrical optics can be used to transform the parameter $q(z)$ through equation

$$q' = \frac{q \cdot A + B}{q \cdot C + D} \tag{a-3}$$

where q' represents the Gaussian beam after the optical element described by the matrix M_{ABCD}.

Optical element	Flat mirror	Free space	Crystal	Thin lens	Curved mirror
M_{ABCD}	$\begin{bmatrix} 1 & 0 \\ 0 & 1 \end{bmatrix}$	$\begin{bmatrix} 1 & d \\ 0 & 1 \end{bmatrix}$	$\begin{bmatrix} 1 & d/n \\ 0 & 1 \end{bmatrix}$	$\begin{bmatrix} 1 & 0 \\ -\frac{1}{2f} & 1 \end{bmatrix}$	$\begin{bmatrix} 1 & 0 \\ -\frac{1}{2r} & 1 \end{bmatrix}$

d is the propagation distance, n is the refractive index, f is the focal length of the thin lens, and r is the radius of curvature of the curved mirror.

Appendix B – Jones matrix calculation

The Jones matrices are operators for Jones vectors, written as

$$\begin{pmatrix} E_{0x}e^{i\phi_x} \\ E_{0y}e^{i\phi_y} \end{pmatrix} \tag{b-1}$$

which are the vectors that describes the propagation of two transverse polarizations of the light in homogeneous isotropic medium. Different optical interfaces and elements have their corresponding Jones matrices. In this section the Jones matrix (*M*) for the birefringent filter used in this thesis is given.

Consider the birefringent plate with angles described in Fig. 3-1 in Chapter 3 inserted into the laser cavity at the Brewster's angle. The Jones matrix for this birefringent plate [1] is described by

$$M = \begin{pmatrix} 1 & 0 \\ 0 & q \end{pmatrix} \begin{pmatrix} \sin\alpha_{eq} & \cos\alpha_{eq} \\ -\cos\alpha_{eq} & \sin\alpha_{eq} \end{pmatrix} \begin{pmatrix} 1 & 0 \\ 0 & e^{i\varphi} \end{pmatrix} \begin{pmatrix} \sin\alpha_{eq} & -\cos\alpha_{eq} \\ \cos\alpha_{eq} & \sin\alpha_{eq} \end{pmatrix} \begin{pmatrix} 1 & 0 \\ 0 & q \end{pmatrix}, \tag{b-2}$$

where

$$q = \frac{2n}{(n^2+1)}, \tag{b-3}$$

$$\sin(\alpha_{eq}) = \sqrt{(1-\cos^2(\alpha_{eq}))}, \tag{b-4}$$

$$\cos(\alpha_{eq}) = (\cos\phi\cos\theta\cos\alpha - \sin\phi\sin\theta)/\sin\gamma, \tag{b-5}$$

and

$$\varphi = \left[(\sin^2\alpha\cdot\cos^2\theta) + (\cos(\alpha)\cdot\cos(\phi(n))\cdot\cos(\theta) - \sin(\theta)\cdot\sin(\phi(n)))^2\right]\cdot\frac{k(n)\cdot\Delta(n)\cdot d}{\cos(\phi(n))} \tag{b-6}$$

which describe the phase difference between the fast and slow axes of the crystal due to birefringence. The five matrices in equation (b-2), from right to left, describe the propagation of the two transverse waves through the first air-glass interface, redistribution of the wave amplitudes to the crystal's fast and slow axes, phase retardation, back-conversion of the axes to the original vertical and horizontal axes, and propagation through the second air-glass interface. The parameter q represents the maximum loss due to the Fresnel reflection which occurs only in S-polarization while P-polarized light experiences no loss. Since the calculation above involved a large wavelength range, the refractive indices of the birefringent plate (n) used in the calculation are also functions of wavelength, $n(\lambda)$ [2]. The round-trip Jones matrix for the linear laser cavity is written as

$$M_{roundtrip} = Q'Q'MM \tag{b-7}$$

which includes the matrices describing the other sources of the polarization dependent loss inside a laser cavity, Q'. Since it is the nature of the oscillator that the propagating wave repeats itself after one round trip, the eigen value of $M_{roundtrip}$ is then the electric field amplitude transmission (m) and $|m|^2$ is the round trip power transmission.

References

[1] K. Naganuma, G. Lenz, and E. P. Ippen, "Variable bandwidth birefringent filter for stable femtosecond lasers," IEEE J. Quantum Electron. 28(10), 2142-2150, (1992).

[2] E. D. Palik, *Handbook of Optical Constants of Solids*, 1st ed. (Elsevier, 1997).

Appendix C – List of publications

Published

1. T. Waritanant and A. Major, "Thermal lensing in Nd:YVO_4 laser with in-band pumping at 914 nm," Appl. Phys. B, 122 135 (2016).

2. T. Waritanant and A. Major, "High efficiency passively mode-locked Nd:YVO_4 laser with direct in-band pumping at 914 nm," Opt. Express 24, 12851-12855 (2016).

3. T. Waritanant and A. Major, "Selectable multi-wavelength operation of a diode-pumped Nd:YVO_4 laser," Opt. Lett. 42(6), 1149-1152 (2017).

4. T. Waritanant and A. Major, "Discretely selectable multi-wavelength operation of a SESAM mode-locked Nd:YVO4 laser," Opt. Lett. 42(17), 3331-3334 (2017).

5. R. C. Talukder, Md. Z. E. Halim, T. Waritanant, and A. Major, "Multiwatt continuous wave Nd:KGW laser with hot-band diode pumping," Opt. Lett. 41, 3810-3812 (2016).

6. Md. Z. E. Halim, R. C. Talukder, T. Waritanant, and A. Major, "Passive mode locking of a Nd:KGW laser with hot-band diode pumping," Laser Phys. Lett. 13, 105003 (2016).

Submitted

1. T. Waritanant and A. Major, "Dual-wavelength CW operation at the 1064.1 & 1073.1 nm and 1064.1 & 1085.3 nm wavelength pairs of Nd:YVO_4 Laser"

Conferences presentations

1. T. Waritanant and A. Major, "Dual-Wavelength CW Operations of a Nd:YVO_4 Laser at 1064.1 & 1073.1 nm and 1064.1 & 1085.3 nm wavelengths," Photonics North 2014, Oral presentation, Abstract Reference Number: 255-hxGf-203 (2014).

2. T. Waritanant and A. Major, "Selectable Multi-Wavelength Operation of a Diode-Pumped Nd:YVO_4 Laser," Photonics North 2014, Poster presentation, Abstract Reference Number: 255-Ra51-203 (2014).

3. T. Waritanant and A. Major, "Thermal Lensing in Nd:YVO_4 Laser with In-Band Pumping at 914 nm," Photonics North 2014, Poster presentation, Abstract Reference Number: 255-oAPq-203(2014).

4. T. Waritanant and A. Major, "High Efficiency Passively Mode-Locked Nd:YVO_4 Laser with Direct In-Band Pumping at 914 nm," Photonics North 2016, Oral presentation, Abstract Reference Number: 255-RCXX-182 (2016).

5. T. Waritanant and A. Major, "Selectable Multi-Wavelength Operation of a SESAM Mode-locked Nd:YVO_4 Laser," Photonics North 2016, Poster presentation, Abstract Reference Number: 255-mLpe-182 (2016).

6. T. Waritanant and A. Major, "Thermal Lensing in Nd:YVO_4 Laser with In-Band Pumping at 914 nm," in CLEO: 2014, OSA Technical Digest (online) (Optical Society of America, 2014), paper JTh2A.80.

7. T. Waritanant and A. Major, "Dual-Wavelength CW Operations at 1064.1 & 1073.1 nm and 1064.1 & 1085.3 nm of Nd:YVO_4 Laser," in *CLEO: 2014*, OSA Technical Digest (online) (Optical Society of America, 2014), paper JW2A.82.

8. T. Waritanant and A. Major, "High Efficiency Passively Mode-Locked Nd:YVO_4 Laser with Direct In-Band Pumping at 914 nm," in *CLEO: 2016*, OSA Technical Digest (online) (Optical Society of America, 2016), paper SM4M.2.

9. R.C. Talukder, Md.Z.E. Halim, T. Waritanant, and A. Major, "Multi-Watt continuous wave Nd:KGW laser with hot band diode pumping," in *CLEO 2016*, June 5-10, San Jose, USA, paper JTu5A.42

10. Md.Z.E. Halim, R.C. Talukder, T. Waritanant, and A. Major, "Passive mode-locking of a Nd:KGW laser with hot band diode pumping," poster presentation in *Photonics North 2016*, May 24-26, Quebec City, Canada.

11. T. Waritanant and A. Major, “Continuous wave operation of $Nd:CaYAlO_4$ and $Nd:ScYSiO_5$ lasers with hot band diode-pumping,” SPIE Photonics West 2017, paper number 11082-63, San Francisco, CA, USA.